PAUL SCHERRER INSTITUT

SwissFEL ARAMIS Beamline Conceptual Design Report

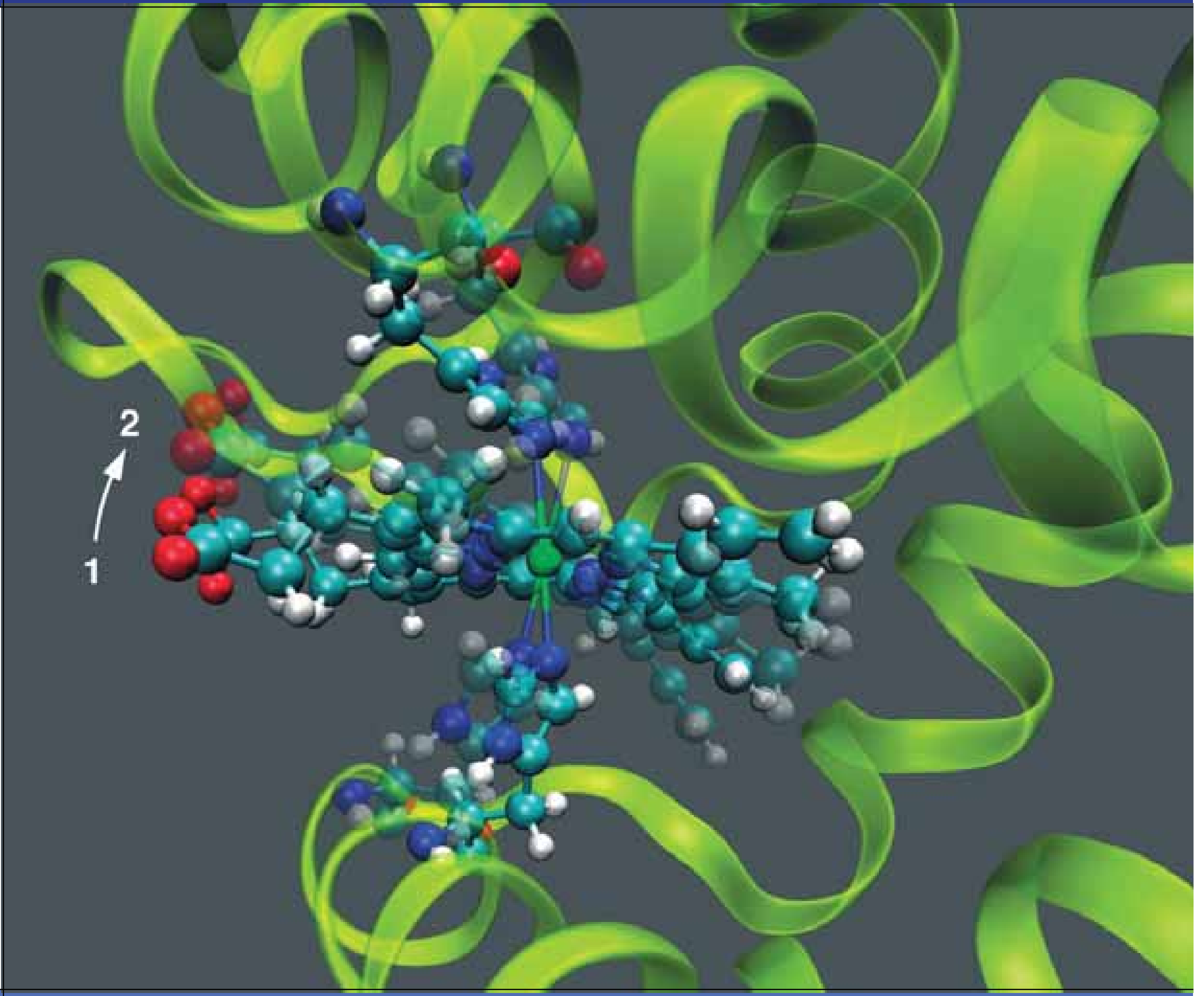

June 2013

ARAMIS beamline

Luc Patthey, Uwe Flechsig, Rolf Follath, Pavle Juranic, Bill Pedrini, Bruce Patterson, Chris Milne, Gerhard Ingold, Milan Radovic, Rafael Abela

Contents

1. **Introduction**

ARAMIS beamline will deliver photons from 2-12.4 KeV to three experimental hutches using three different optical beamlines called AR1, AR2 and AR3. Figure 1 illustrates a hand sketch of the ARAMIS optical layout. A combination of off-set mirrors is used to bring the beam alternatively to one of the three beamlines. The most upstream off-set mirrors bring the beam on the left side to the AR1 trough a double horizontal reflection. A crystal monochromatic beam can also be delivered to the end-station by a 4-bonce scheme made of a double crystal monochromators and two vertical deflecting mirrors. The beam is then focused at the end-station by Kirkpatrick-Baez focusing optics. For the AR3 beamline, the off-set mirrors of AR1 are retracted out of the beam and a second set of off-set mirrors deflects the photons horizontally to the right side and to the beamline. This beamline can also be equipped with a X-ray delay stage and a Kirkpatrick-Baez focusing optics. When both AR1 and AR3 off-set mirrors are retracted, the beam goes straight to the central beamline AR2, which uses a similar optical scheme installed at SACLA [1]. It consists in two vertical deflecting mirrors and a double crystal monochromator which are intercalated. The mirrors and the monochromator are used alternatively but never simultaneously.

The optical layouts proposed for AR1, AR2 and AR3 allow the propagation of the monochromatic or pink FEL radiation with or without monochromators, respectively. For the three beamlines, the beam height remains unchanged between both configuration which significanttly simplifies the mechanical design of the photon diagnostics and end-stations where no special translation are requested to “follow” the monochromatic or pink beam. The nominal photon energy range of the ARAMIS is 2-12.4 KeV, while AR2 and AR3 are designed to cover the photon energy up to 15.5 KeV in case of possible future machine energy upgrade. It is also foreseen to extend the ARAMIS beamline with large off-set monochromators (not shown in Figure 1) to allow parallel user operation as done at LCLS [2]. The Large off-set monochromator splits the beam with a thin single crystal producing pink beam on the main beamline and monochromatic beam on the side branch. A detailed specification of the optical layout is given in the CDR: ARAMIS Optical Layout.

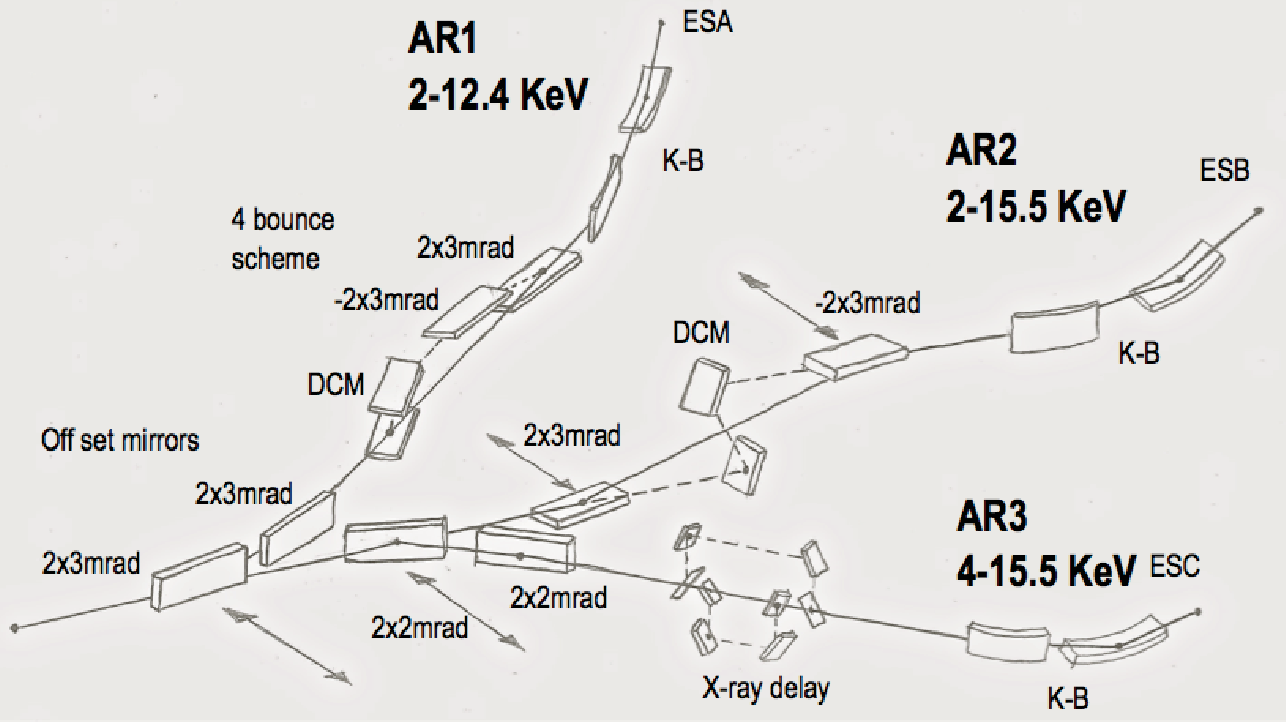

Figure 1: Hand sketch of the tree ARAMIS optics beamlines.

A detailed layout of ARAMIS is given in Figure 2, the beamline is located in following main area:

- the front end „inside the tunnel“
- the optical hutch
- the experimental halls 1, 2 and 3

The color code of Figure 2 describes the different phases of the ARAMIS beamline. The components labeled in blue will be ready “to take” the photon beam in 2016 and available for user operation in 2017. AR1 will deliver the beam in the experimental hutch 1 and AR2 in experimental hutch 2. AR3, shown in pink, will be installed later in 2017. Further extensions of the beamlines are shown in yellow–green: the large off-set monochromator for parallel user operation or prolongation of the beamline to the next experimental hutch for additional user end-stations.

The order in which the FEL radiation is distributed between the different experimental hutches and end-station is not predefined and will depend on the experimental program. But the operation mode should allow a maximum of flexibility to optimize the use of FEL radiation. While the FEL radiation is delivered to one experimental hutch, access to other experiment hutches will be possible for preparation of the next experiment/beamtime. In the second phase (> 2017) the large offset monochromator could be used to distribute the FEL radiation to two different hutches simultaneously. Under these conditions, the access to the third hutch should still be guaranteed for preparation work. Such operation modes require a proper shielding scheme. A detailed description of the operation mode combined with the shielding set-up is given in CDR: Operation Mode and Safety Concideration.

Due to the stochastic nature of the FEL radiation, photon diagnostic plays a particularly important role for both end-stations and the machine. Pulse energy, position, profile, spectral distribution, time arrival and pulse length monitors will deliver shot-by-shot information for all three ARAMIS beamlines. An extensive description of the photon diagnostic items with specifications is given in the CDR “Photon Beam Diagnostics”.

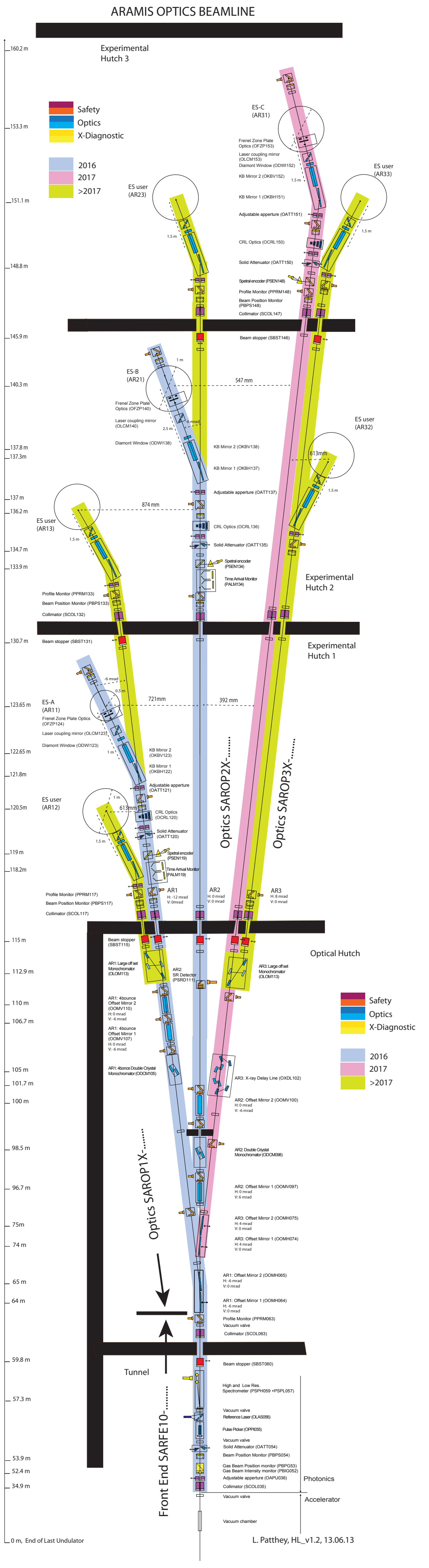

Figure 2: A detailed layout of ARAMIS. The color code indicates the different installation phases. A new Z origin for the photon beamline is set for convenience at the end of the last undulator and corresponding to a Z “machine” of 567.7385 m.

2. Front end

The front end layout for ARAMIS is given in Figure 3 and its schematic view is depicted in Figure 4. The first upstream component is the collimator followed by an adjustable x-ray double slit system, with dimensions from 30 mm x 30 mm to completely closed. The role of those components is to restrict the angular acceptance on the beamline to the angular distribution of the FEL radiation and limit the effect of spontaneous radiation. In normal operation, the opening of the x-ray double slits will be set to 4-6 sigma of the FEL central cone. A detail description of those items is given in chapter “Concept of Beamline Operation and Basic Specifications for the Photon Beam Stoppers and Collimators at the ARAMIS Photon Beamlines”. The first photon diagnostics element in the front end is the gas beam intensity and position monitor developed and produced by DESY [3] followed by a solid position monitor developed by SACLA [4]. A solid attenuator with a set of thin diamond and silicon films of various thicknesses is used to adjust the beam pulse fluence, while a pulse picker is used to select the desirable pulse to be “sent” through the beamline. A single shot spectrometer using diffractive diamond grating and bent silicon crystal can record the spectral distribution of the FEL radiation from pulse to pulse. This scheme has been developed at PSI [5]. The last item inside the tunnel is the beam stopper, which controls the radiation exiting the tunnel, while a collimator located outside the tunnel limits the angular distribution of the radiation from the tunnel. Finally, the front-end section ends with a beam profile monitor located just behind the collimator.

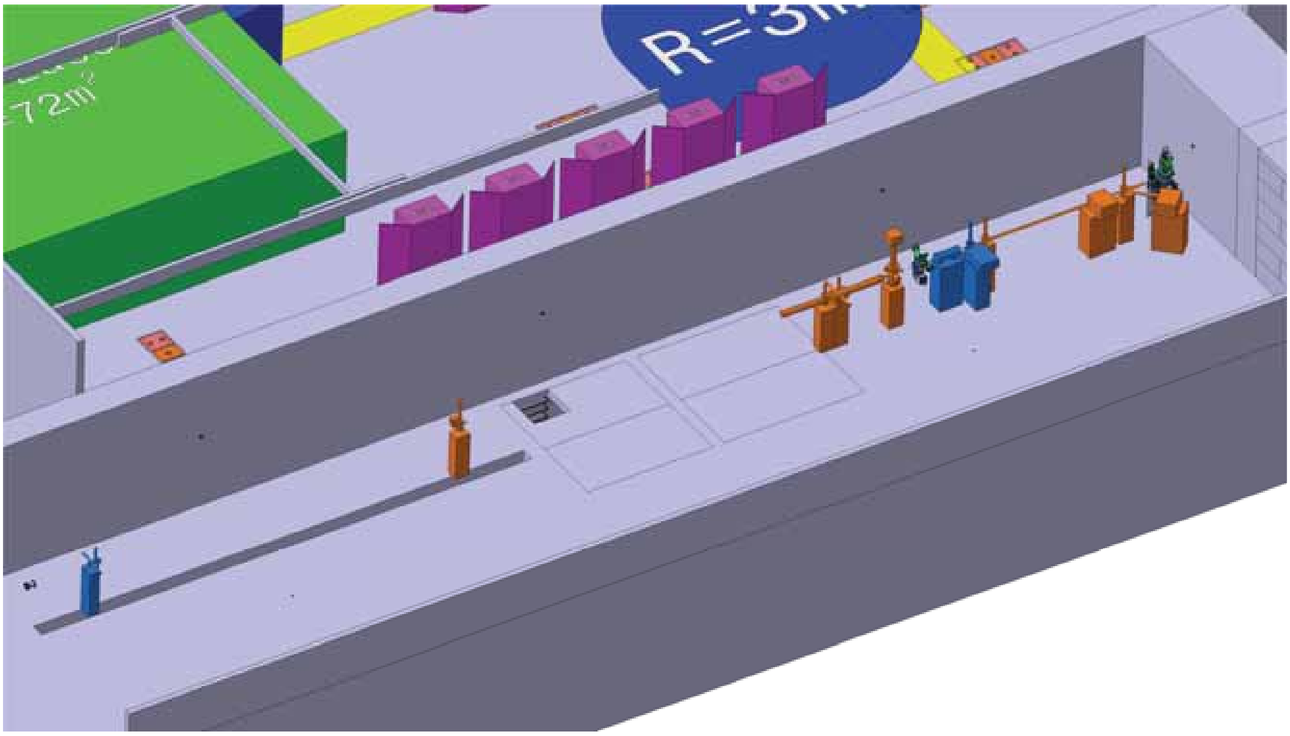

Figure 3: 3D view of the ARMIS Front End

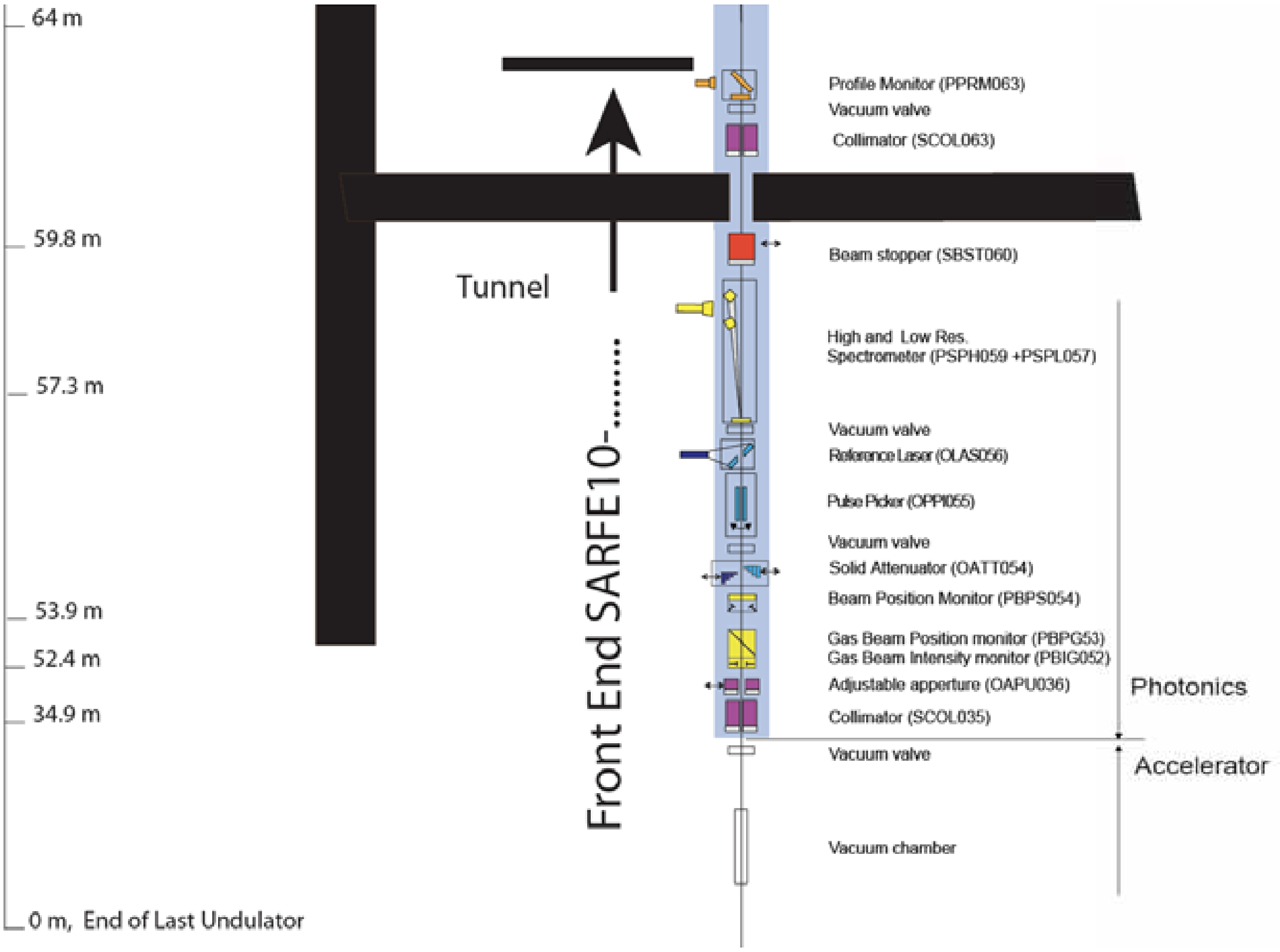

Figure 4: Schematic view of the front-end, which corresponds to an enlarged view of Figure 2 over the range of 0 to 64 m in Z beamline coordinate.

2. Optical hutch

The optical hutch is given in Figure 5 and the schematic view of the beamline inside the optical huch is depicted in Figure 6. As mentioned earlier, a set of off-set mirrors will deflect the beam to the three ARAMIS beamlines (AR1, AR2 and AR3). Those mirrors are installed in the optical hutch. They are located upstream of the monochromators or X-ray delay line. Two large off set monochromator in AR1 and AR3 can be installed downstream from the optical hutch for parallel user operation, similar to the scheme proposed at LCLS [2]. Beam profile monitors are mounted after each optical component for diagnostics and beamline alignment. A 2 dimensional detector is located on AR2 (central beamline) to record the spontaneous radiation from the undulators. This detector will be used for the commissioning of the undulators. The last items of the optical hutch are the beam stoppers, which control the radiation exiting the optical hutch when a collimator located behind the wall and inside the first experiment hutch limits the angular distribution inside the experimental hutch to prevent any spontaneous radiation or bremsstrahlung from exiting to the vacuum tubing of the beamline.

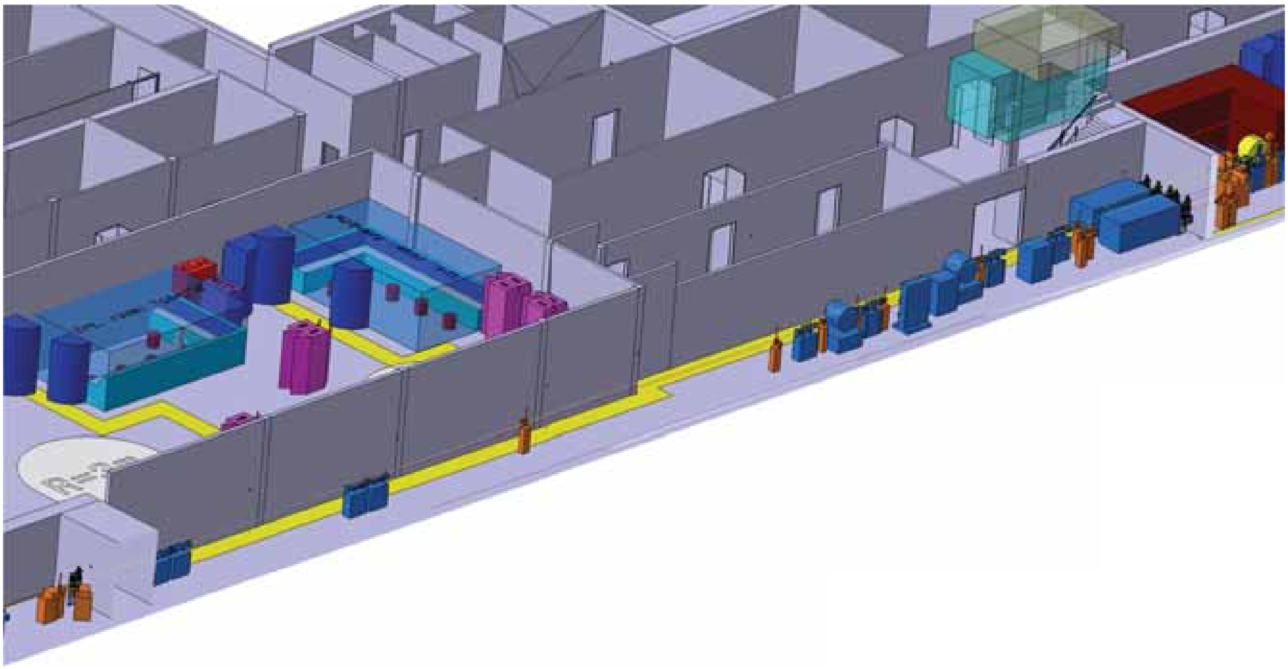

Figure 5: 3D view of the ARMIS optical hutch

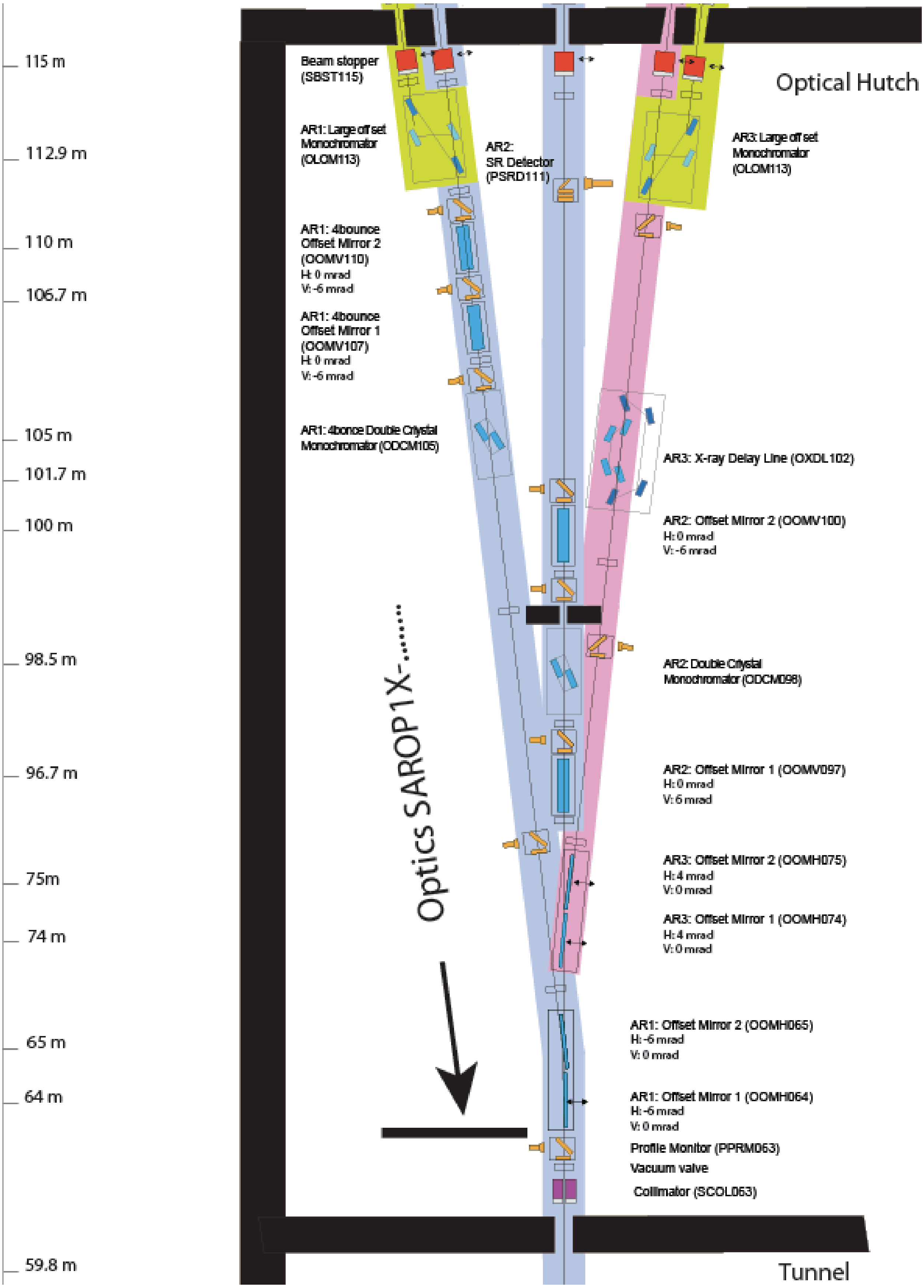

Figure 6: Schematic view of the Optical hutch, which corresponds to an enlarged view of Figure 2 over the range of 59.8 m to 115 m in Z beamline coordinate.

2. Experimental hutches

The experimental hutch model is given in Figure 7 and the schematic view of the beamline inside experimental hutch 2 is shown in Figure 8. Several photon diagnostics tools are located in the beamlines downstream from the collimator. Solid intensity and profile monitors are installed on each beamline and each of the side branches. Other photon diagnostics are mounted on the beamlines according the specific beamline and end-station needs. In particular for AR1 and AR2, a pulse arrival and pulse length monitor followed by a spectral encoder monitor are installed to measure the time jitter between the pump laser and probe FEL radiation. More details on those monitors are given in the CDR: Photon Beam Diagnostics. Since the pulse arrival and pulse length monitors need the full FEL beam for a good signal/noise ratio of the time jitter measurement, a solid attenuator (similar as installed in the front end) is mounted after those monitors to adjust the beam pulse fluence at the end-station. Finally, a Kirkpatrick-Baez optics will focus the beam at the end-station. Alternative focusing schemes such as compound refractive lens or Frenel Zone plate optics are also being considered.

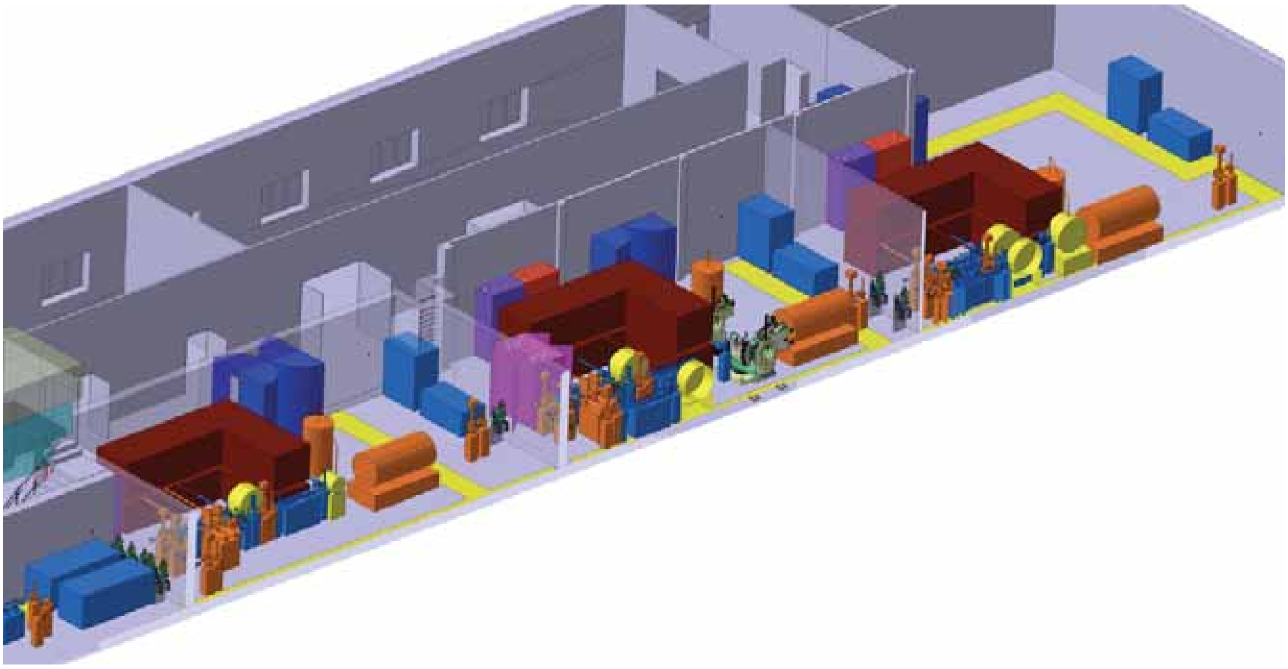

Figure 7: 3D view of the ARMIS Experimental hutch 2

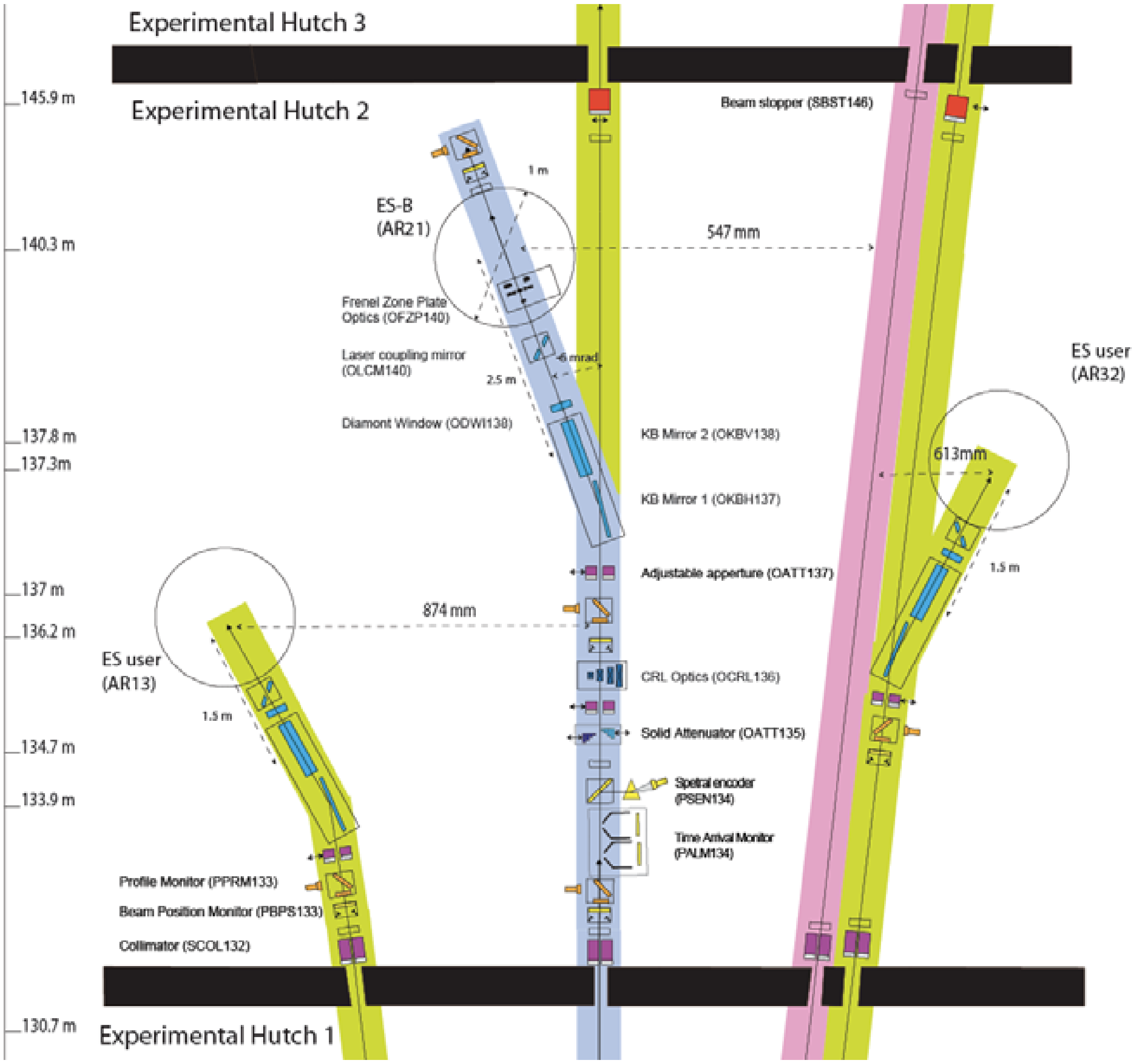

Figure 7: Schematic view of the Experiemental hutch 2, which corresponds to an enlarged view of Figure 2 over the range of 130.7 m to 145.9 m in Z beamline coordinate.

[1] M. Yabashi, private communication
[2] Y. Feng et al. Proc. *SPIE* **8504** X-Ray Free-Electron Lasers: Beam Diagnostics, Beamline Instrumentation, and Applications (2012) doi: 10.1117/12.930944
[3] K. Tiedtke et al., Gas Detectors for X-Ray Lasers, Journal of Applied Physics 103, 094511 (2008).
[4] T. Kensuke *et al.* Rev. Sci. Instrum. 82, 023108 (2011)
[5] C. David, private communication

ARAMIS Optical Layout

Uwe Flechsig, Rolf Follath, Luc Patthey, Rafael Abela

Contents

1 Abstract

This document presents the basic concepts for the X-ray beam transport systems at the Aramis beamlines. The Aramis undulator is one out of several planned undulators at the SwissFEL that are attached to the same linear electron accelerator structure and will deliver photons for the hard X-ray regime from 1770 eV up to 12400 eV. The beam transport system distributes the FEL-beam from the Aramis undulator to three end stations alternatively. While switching between the end stations of one undulator is expected to happen not more than a few times per day, the electron beam can be switched on a bunch to bunch rate between the different undulators in the future.

The Aramis end stations are dedicated to different scientific research fields and have very specific requirements concerning the beam properties. To address these particular needs, three specifically optimized beamlines are foreseen.

2 Introduction

The Paul Scherrer-Institut (PSI) has a long and internationally recognized experience in the operation of the third generation light source SLS. While this light source offers excellent conditions for experiments requiring high average brilliance, the new free electron X-ray laser facility SwissFEL opens the field for physics on an ultra short timescale with extremely high peak brillances [1, 2]. Both facilities cover the hard- and soft X-ray range from 0.1 nm to 7 nm, which is extended by the SLS into the infrared regime.
To cover the full wavelength range, the SwissFEL facility divides up into an undulator line Aramis for the hard X-ray regime and the undulator line Athos for the soft X-ray regime. Future upgrades with additional undulator lines are already foreseen in the layout of the buildings and will be realized at a later date. This report describes the beam transport system for the Aramis undulator lines for photon energies from 1.77 - 12.4 keV, but many aspects are valid for the Athos lines too.

The beam transport system has several functions and purposes. While some of them are mandatory for all lines, others may be realized in particular branches only. From the optical point of view, the most important are

1. the distribution of the beam to the various end stations.
2. the monochromatisation of the FEL-beam or the alternative use of the undispersed, pink beam in the same end station.
3. the formation of beam spots with variable size in the end stations.
4. the splitting of photon pulses into two pulses by a delay line with variable time delay.

The overall layout of the beam transport system is shown in Figure 1. Two pairs of horizontal offset mirrors deflect the beam to the Aramis 1 and Aramis 3 beamlines with 12 mrad and 8 mrad total deflection angle, respectively.
With the smaller deflection angles, the Aramis 3 beamline emphasizes the higher spectral range and envisages the Mössbauer transition at 14.4 keV, which will optionally be available after phase two upgrade. It uses the pink undulator beamline without further monochromatisation. Instead, a delay line is foreseen to split the FEL pulse into two pulses with variable time delay. This delay line is part of the phase two installation and not covered by this document.
The Aramis 1 beamline offers a pink mode and a monochromatised mode, where the bandwidth of the FEL-beam is reduced by a factor ten with the help of a crystal monochromator. For pink beam operation the monochromator and a additional pair of vertically deflecting mirrors is retracted, leaving the beam direction unchanged. The

adaptive offset mirrors already allow for a moderate horizontal focusing. Additional two dimensional focusing is available with compound refractive lenses. For ultimate focusing, a pair of mirrors in a Kirkpatrick Baez [3] configuration allow for an achromatic operation over the full energy range.
In the middle, the Aramis 2 beamlines employs a pair of vertically deflecting offset mirrors with 6 mrad deflection angle. Alternatively, a monochromator can be introduced to further monochromatise the FEL-radiation. In that mode, the offset mirrors are retracted and the monochromator is the only optical element in the beam. Again, the beam direction for pink and monochromatised mode is the same. The adaptive offset mirrors provide a vertically focusing. For additional focusing, compound refractive lenses and a KB-system is foreseen.
Large offset monochromators are planned for phase 2 operation but not shown in Figure 1. They will be installed in all branches between the monochromators and the refocusing optics and enable the simultaneous usage of the FEL-beam in two experimental stations.

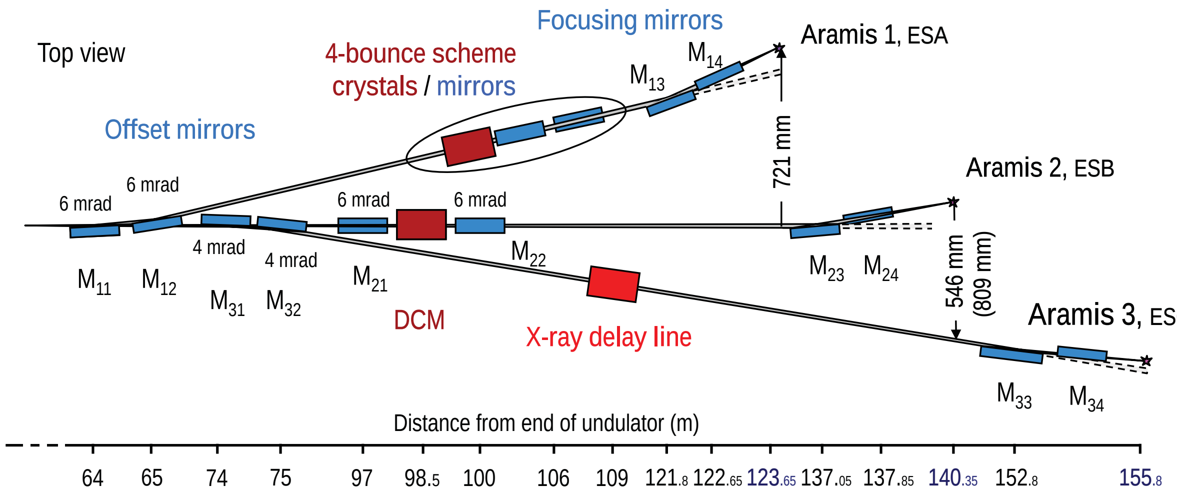

Figure 1: Schematic layout of the Aramis beamlines

Whenever possible, the beam transport system should accept the whole FEL beam, i.e. five times the rms-value of the beam cross section. This may not be possible at all photon energies and at all optical elements. But at least an acceptance four sigma should be guaranteed. A smaller acceptance not only wastes pulse energy but also leads to interference effects at the apertures, resulting in an inhomogeneous intensity distribution on the sample. This becomes a major drawback, especially when nonlinear processes are studied. Besides the mirror surface quality, the mirror lengths and deflection angles are therefore of crucial importance for the optical design. Particular attention is payed to the choice of mirror coating materials to increase the acceptance of the mirror systems.

3 Undulator

Within the SwissFEL facility, the Aramis undulator will serve as Free Electron Laser for the hard X-ray regime. The Aramis line will use a planar in vacuum undulator with a period length of 15 mm. Fifteen modules, each having a length of 4 m will be operated at a k-value of 1.2. For small changes in the photon energy, the gap can be varied between 3.2 mm and 5.5 mm, but the main parameter to change the photon energy is the variation of the electron energy in the accelerator between 3.1 GeV and 5.8 GeV. The use of dysprosium–enriched NdFeB magnets allows the undulators to be operated at room temperature, avoiding an expensive liquid nitrogen cooling system, as is would be required for undulators with conventional magnets. The beamlines will assist the alignment process of the undulators by characterizing the spectral emission pattern and help to match the k-values of the individual undulator modules.

GENESIS calculations performed by S. Reiche serve as basis for the layout of the beam transport system. The accelerator foresees two operation modes, one with 10 pC bunch charge and ultrashort pulses of 2 fs (rms) pulse lengths[1], and one with 200 pC bunch charge, 20 fs (rms) pulse lengths and higher pulse energies[2]. The data for the two modes are summarized in Table 1 and values for source size and divergence are plotted in Figure 2.

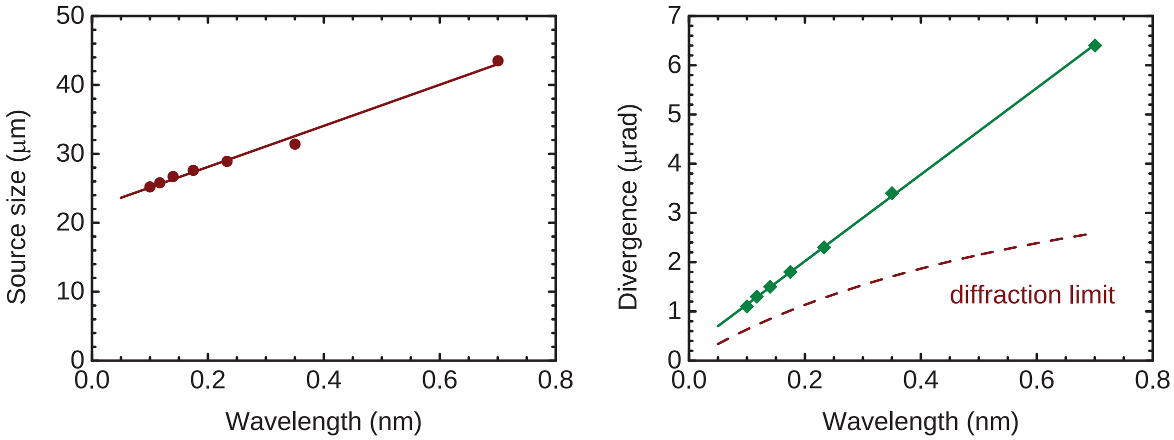

Figure 2: Source size (left) and beam divergence (right) of the Aramis-FEL-beam according to Table 1. A linear regression to the data is plotted in both diagrams. The dashed line in the right diagram shows the divergence of a gaussian beam with the same beam waist as the FEL-beam.

The source size and divergence are proportional to the wavelength and a linear regression is plotted in both diagrams. From the source size σ, a diffraction limited divergence $\sigma' = \lambda/(2\pi\sigma)$ is calculated and shown as dotted line in the right diagram. This assumes

---

[1] see https://intranet.psi.ch/Swiss_FEL/DesignParameters10pC, Run date Dec-2012.

[2] see https://intranet.psi.ch/Swiss_FEL/SwissFELSimAramis-Design , Run date Nov-2012.

Photon energy (eV)	1770	3540	5320	7090	8860	10600	12400
Source size* (µm)	**44**	**31**	**29**	**28**	**27**	**26**	**25**
	48	33	24	22	19	20	23
Source divergence* (µrad)	**6.4**	**3.4**	**2.3**	**1.8**	**1.5**	**1.3**	**1.1**
	8.3	4.5	2.7	2.1	1.7	1.7	1.6
Pulse energy (µJ)	**200**	**150**	**160**	**180**	**180**	**180**	**160**
	5	6	14	15	15	10	10
Spectr. Bandw.* (%)	**0.17**	**0.09**	**0.09**	**0.07**	**0.06**	**0.06**	**0.06**
	0.16	0.14	0.17	0.10	0.08	0.08	0.07
Beam size* in 70 m (µm)	**450**	**240**	**160**	**130**	**110**	**95**	**80**
	580	320	190	150	121	121	114

*rms-values

Table 1: Beam parameters for the Aramis undulator operating with **200 pC** and 10 pC bunch charge.

a gaussian intensity distribution in the waist of the FEL-beam and sets the lower limit of beam divergence.

The values for beam size and fluence are plotted in Figure 3 for typical distances of the offset and the refocussing mirror systems. Without pre focusing, the beam at the end of the Aramis 2 beamline extents to almost 5 mm width (5σ, 1.7 keV).

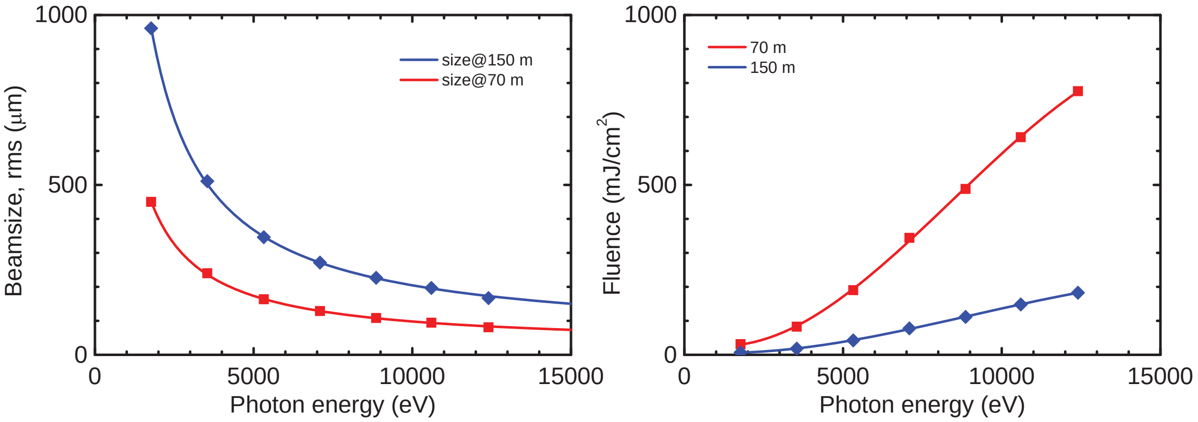

Figure 3: Beam size and fluence at the offset mirrors (70 m) and the location of the refocusing mirrors of Aramis 2 (150 m).

4 Optical properties and damage risk

Reflective mirrors with small glancing angles deflect and focus the x-rays in the Aramis beamlines. They are made of single crystal silicon for high mechanical and thermal stability, while their optical properties are independently tailored by an appropriated choice of coating materials and layer parameters. The mirrors for Aramis should cover the full spectral range with a high and smooth reflectance and without pronounced spectral features. Multilayer mirrors with stacks of several hundreds of bilayers are generally optimized for a specific combination of incidence angle and photon energy and are therefore not suitable as general purpose mirrors in the Aramis beamlines.

4.1 Optical properties

The optical properties of the coatings are determined by the Fresnel formulas and the layer parameters as e.g. thickness and roughness. For hard X-rays the index of refraction n is very close to, but slightly smaller than one

$$n = 1 - \delta + i\beta \ , \tag{1}$$

with $\delta, \beta \ll 1$. In this regime, the optical constant δ is reasonably well described by the electron density n_e and the wavelength

$$\delta = \frac{r_e n_e}{2\pi}\lambda^2, \tag{2}$$

where $r_e = 2.818 \cdot 10^{-15}\mathrm{m}$ is the classical electron radius. The critical angle θ_c for total external reflection can be approximated by

$$\theta_c \approx \sqrt{2\delta} \approx \sqrt{\frac{r_e n_e}{\pi}} \cdot \lambda \ , \tag{3}$$

Materials with mid or high electron densities as ruthenium, molybdenum or gold show large critical angles and are often used as coatings for hard X-ray mirrors. Their high damage risk to the peak power of XFEL pulses hindered their usage in FEL beamlines in the past. Recent experiments at existing FELs indicate that at least mid-Z material as ruthenium withstand the high intense beam better than expected [4]. Cooling by photo electrons has been proposed as effective mechanism to explain their capability to withstand higher peak power and to increase their damage threshold. The usage of these high-Z materials could now be reconsidered, especially for mirrors that experience lower fluences at the end of the beamlines

The small divergence of the XFEL-beams allow for very small grazing incidence angles θ, where the reflectance R is high and the increased footprint dilutes the beam intensity over a larger area. For angles lower than the critical angles, this is a way to reduce the power load for the surface atoms on the mirrors, while for angles larger than the critical angle the dilution effect is counteracted by the reduced penetration depth.

In a simple model, the dose, η, absorbed by an atom or molecule in the top layer is assumed to be proportional to the incident fluence Φ

$$\eta = \sigma \cdot \Phi \tag{4}$$

with the cross section

$$\sigma = \frac{\sin\theta\,(1-R)\,\mu_g}{n_A}\ , \tag{5}$$

where n_A denotes the particle density[3]. The absorption coefficient μ_g is related to the photon wavelength and the index of refraction by

$$\mu_g = \frac{4\pi}{\lambda}\Im\left\{\sqrt{n^2-\cos^2\theta}\right\} = \frac{2\sqrt{2}\pi}{\lambda}\cdot\sqrt{2\delta-\sin^2\theta+\sqrt{(2\delta-\sin^2\theta)^2+4\beta^2}}\ . \tag{6}$$

With this, the penetration depth $d_e = 1/\mu_g$ can be calculated. It measures the distance perpendicular to the surface where the intensity reduces to a fraction 1/e of the surface value. Together with the beam footprint, the penetration depth defines the volume in which the absorbed energy is deposited. Figure 4 shows values for reflectance, penetration depth and cross section for relevant materials at a grazing incidence angle of 3 mrad. These values are specific for the material and independent of the beam properties. To obtain the absorbed dose for an atom on a mirror surface, the cross section is multiplied with the fluence at the mirror position according to eqn (4).

---

[3] $n_A = \rho N_A/A$ with the Avogadro number N_A, the density ρ and molar weight A of the material.

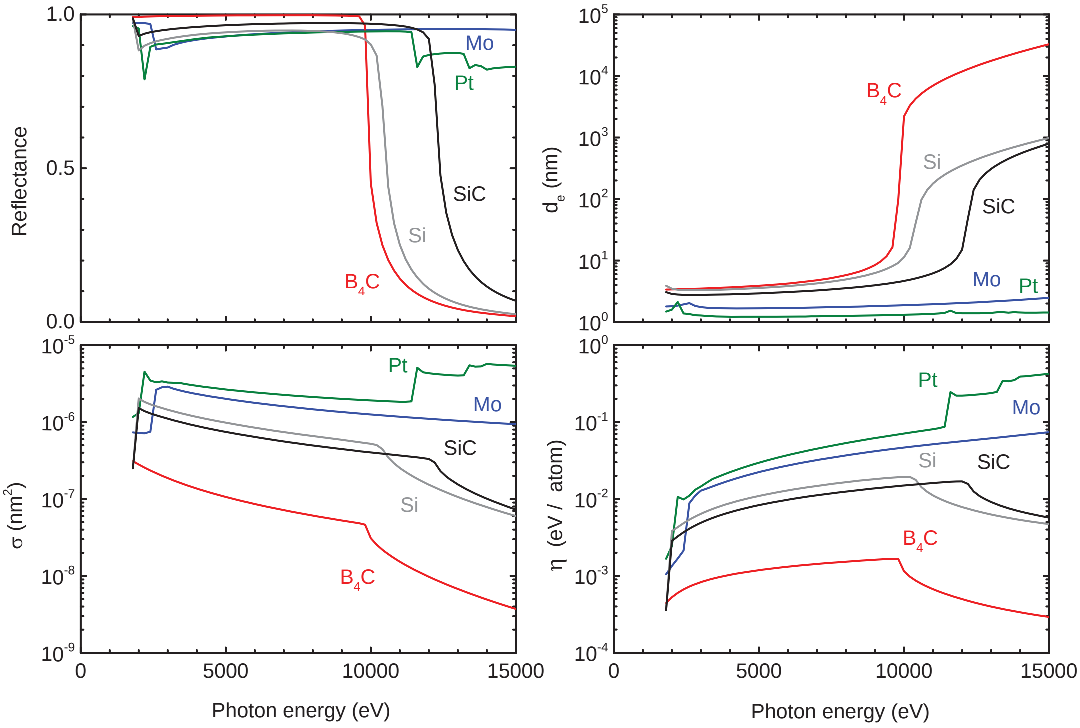

Figure 4: Reflectance, penetration depth and cross section for atoms on a mirror surface with a grazing incidence angle of 3 mrad according to eqn (4). The absorbed dose η, shown in the lower right diagram, is calculated for the 200 pC mode and an offset mirror in 70 m distance from the undulator.

The absorbed dose is calculated for an offset mirror at 70 m distance from the undulator and shown in lower right diagram of Figure 4. For low-Z material as B$_4$C or SiC the maximum dose is absorbed at the critical angle. Mid- and high-Z materials show a broad maximum with steps at the absorption edges. B$_4$C would be the ideal coating material for photon energies up to 10 keV and a grazing incidence angle of 3 mrad. It has the lowest cross section, the highest reflectance and no absorption edges in the given photon energy range. Elements with higher Z show lower reflectance and more spectral features, but offer a higher critical energies. SiC could cover the full energy range but shows a distinct Si-K absorption edge at 1840 eV. Composite layers with two or more layers combine the high and smooth reflectance of low-Z materials with te high critical energy of mid and high-Z materials. Coatings with two and three layers are investigated in more detail in section 5.

An alternative way to achieve a high reflectance and a high critical energy would be a smaller grazing incidence angle. According to eqn (3) the critical energy of B$_4$C increases by 50% to 15 keV, when the grazing incidence angle is reduced from 3 mrad to 2 mrad. But this would require longer mirrors, that are currently not available.

4.2 Damage

The high peak power of the FEL has the potential to damage material placed in the beam. It was found that the dose for threshold damage for surface damage is comparable to the dose required for thermal melting [5, 6].

To estimate the potential hazard, the melting dose of relevant materials is calculated and compared to the absorbed dose. The melting dose is calculated as the sum of the dose to heat the material from room temperature to the melting temperature and the heat of fusion to actually melt it [5]. The values for relevant materials are listed in Table 2.

Material	Be	B_4C	Al	Si	SiC	Mo	Pt	W	InSb
Dose to melt (eV/atom)	0.42	0.74	0.3	0.89	1.03	1.32	0.7	1.8	0.4

Table 2: Melting dose of materials. The dose is given in units of electronvolt per atom. For compounds the dose is equally distributed to the constituents.

Normal incidence damage

In normal incidence, when all of the radiation is absorbed within the attenuation length ($\theta = 90°, R = 0$) in eqn (5), the dose absorbed by a top layer atom, eqn (4), becomes

$$\eta(E) = \frac{\mu_L(E)}{n_A} \cdot \Phi(E) \tag{7}$$

with the linear attenuation factor μ_L. Due to its energy dependence, the absorbed dose depends strongly on the photon energy (E), especially when absorption edges are in the photon energy working range. To estimate the damage risk of a material in a certain distance to the FEL-source, the maximum absorbed dose as function of the distance to the undulator is calculated and compared to the dose to melt it.
In the first step the photon energy E_m is determined, where the maximum dose is absorbed, and then the beam parameters for this energy are used to calculate the beam size and the dose $\eta(E_m)$ as a function of the distance. Figure 6 shows the normal incidence dose at 70 m distance from the undulator. At this distance all materials operate at least one order of magnitude below their melting dose. The most critical material is indium antimonide, which is foreseen as crystal for the very low photon energy range. For safety reasons, this crystals should not operate above their L-edges at 3600 eV.

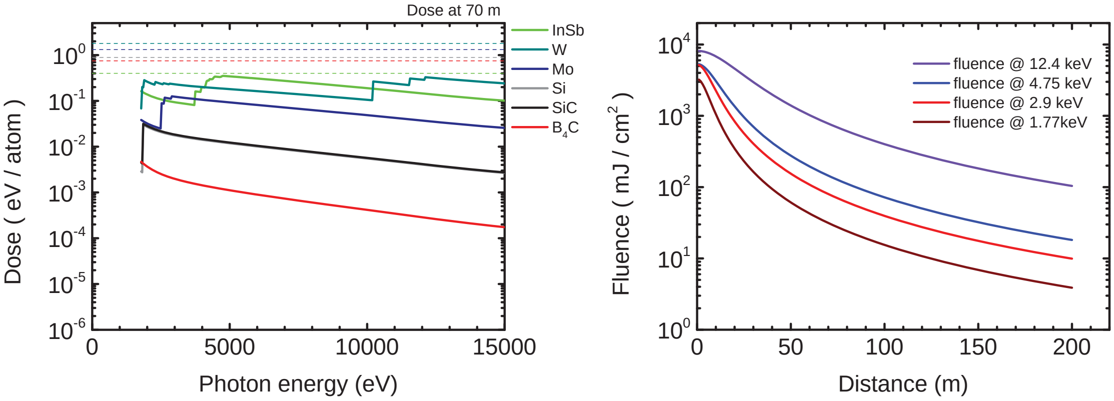

Figure 5: Normal incidence dose at the distance of the offset mirrors at 70 m.

Placing material nearer to the undulator increases the absorbed dose. To estimate a critical distance, Figure 6 shows the maximum absorbed dose (between 1.77 keV and 15 keV) of material as function of the position along the free propagating Aramis beam.

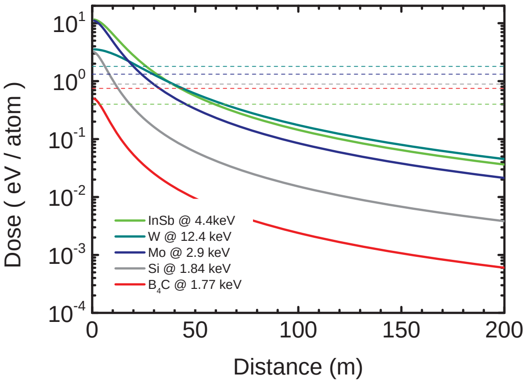

Figure 6: Maximum absorbed dose as function of position along the free propagating Aramis beam.

With the current beam parameters, the low-Z materials as B_4C and Beryllium can safely be used at all distances. Mid-Z materials as molybdenum are already safe at the location of the offset mirrors and High Z-materials as tungsten cannot be used without protective layers in the Aramis beamlines.

4.3 Surface quality

Residual figure errors of the mirror surface cause phase distortion of the reflected wave field of wavelength λ, see Figure 7. The phase errors ϕ induced by a figure errors of Δh are related by the grazing incidence angle θ through

$$\phi = \frac{2\Delta h \cdot \sin\theta}{\lambda} \,. \tag{8}$$

According to the Marechal criterium the rms-value σ of the surface figure error should obey

$$\sigma \leq \frac{\lambda}{14} \,. \tag{9}$$

With N surfaces and small grazing incidence angles the individual surfaces errors should be smaller than

$$\sigma \leq \frac{\lambda}{14\sqrt{N}2\theta} \,. \tag{10}$$

With four mirrors, a grazing incidence angle of 3 mrad and a design wavelength of 0.1 nm, the profile error of each mirror should be smaller than 0.6 nm. This is within the current state of the art and has been achieved for mirrors over a length of 400 mm[7].

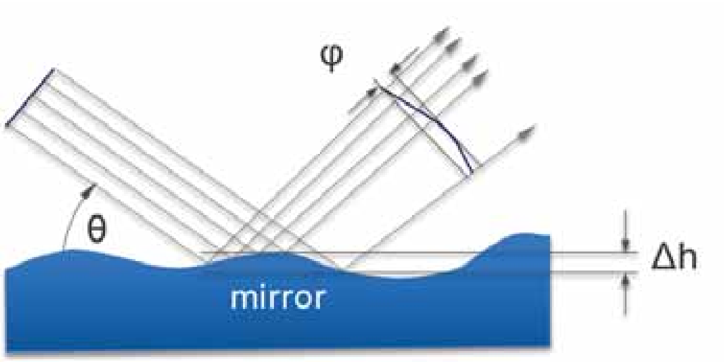

Figure 7: Phase distortions due to surface profile errors.

5 Coatings for offset and refocusing mirrors

The mirrors of the Aramis beamlines are covered with coatings to enhance reflectance and the critical angle. Beamlines at existing FELs use mainly coatings with low-Z materials as boron carbide or carbon. They are less sensitive for beam damage but have small critical angles. To increase the critical angle, materials with higher Z are more favorable but more sensitive to beam damage. They could be used at locations in the beamline where the fluence values are low enough to tolerate their usage. Mirrors with platinum coatings are foreseen e.g. for the soft X-ray self seeding beamline at the LCLS.

To investigate the potential of these materials, several layer systems with low, medium and high-Z are considered for SwissFEL beamlines. Three different samples from two suppliers were investigated to compare the theoretical calculations with the properties of real systems.

1. Coating L: 50 nm SiC with 10 nm B_4C on top,
2. Coating M: 20 nm Mo with 15 nm B_4C on top,
3. Coating H: 10 nm Au or Ir, 5 nm Mo with 15 nm B_4C on top.

Low-Z materials will be able to cover the designated photon energy range of the SwissFEL and are foreseen as safe fallback solution. Coatings with medium-Z would extend the photon energy range to allow for third harmonic operation, or to increase the deflection angle at the mirrors. This would allow for shorter mirrors. High-Z materials could be used at the refocussing mirrors, where the wide beam cross section reduces the fluence. With larger incidence angles, the refocussing mirrors could accept the full beam even at low photon energies without restricting the critical photon energy. Mirrors with high-Z materials could also be used in monochromatic mode downstream of the monochromator, when the fluence is reduced due to the smaller bandwidth,.

5.1 Coating with low Z materials

Coatings with low Z material will withstand the Aramis beam at the distance of the offset mirrors, see Figure 4. One of the layer systems foreseen for the offset mirrors will therefore consist of such light elements as fallback solution.

At the highest design energy, silicon carbide can be used with a maximum incidence angle of 3 mrad. An additional 10 nm thin B_4C-layer on top of the SiC is effective at lower photon energies and covers the drop in the reflectance due to the silicon K-edge. At higher photon energies the B_4C becomes transparent and the reflectance is determined by the SiC-layer, see Figure 8. With 3 mrad incidence angle, a single B_4C layer without SiC would only operate up to 10 keV.

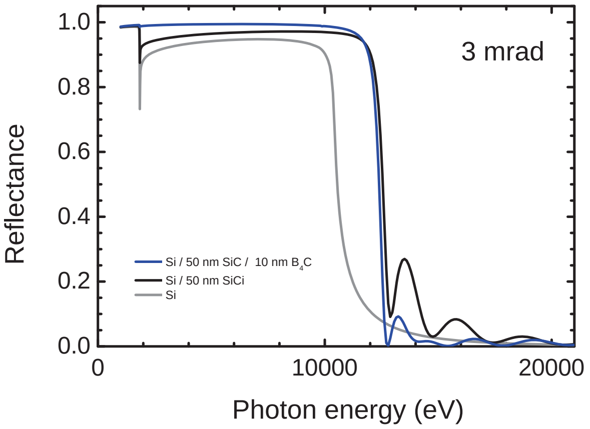

Figure 8: Low-Z coatings with 10 nm B_4C-layer on top of a 50 nm SiC-coating.

5.2 Coating with medium Z materials

Coatings with medium Z elements as molybdenum, ruthenium or rhodium are promising candidates to increase the critical angle for a given photon energy. Here a layer system with molybdenum and B_4C is considered. This combination is often used in multilayer systems and the technology to fabricate it is well established [8, 9, 10].

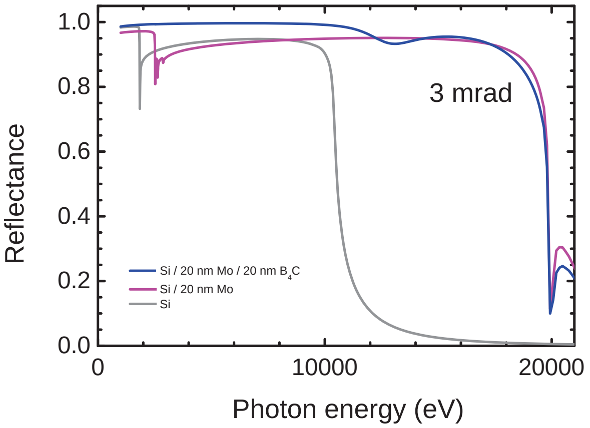

Figure 9: Layer system with mid Z coating of 20 nm molybdenum, covered by a 15 nm B_4C-layer.

The coating consist of 20 nm thick molybdenum layer directly on the silicon substrate. It is covered by a 15 nm thick layer of B_4C, see Figure 9. At 3 mrad incidence angle, the B_4C-layer reflects up to its critical energy of about 10 keV. Above 10 keV the B_4C

becomes transparent and reflectance is carried by the underlying molybdenum layer, which has the potential to extend the photon energy range up to 20 keV. The thickness of the molybdenum layer is determined by the film quality, which becomes worse with increasing thickness and by the necessity to reflect up to the Mo K-edge. The B_4C layer has to be thick enough to cover the molybdenum L-edges around 2600 eV, but thin enough to prevent the occurrence of standing waves up to the maximum design energy of 12.4 keV. The occurrence of standing waves in the B_4C-layer enhances the field amplitude in the layer and may limit the use of this system at higher photon energies. The field amplitudes are calculated with IMD[11] and shown in Figure 10. With the layer thickness $d = 15$ nm and the incidence angle $\theta = 3$ mrad, the simple resonance condition

$$\lambda = 2d \sin\theta \tag{11}$$

would be fulfilled for a wavelength of 0.09 nm (13.8 keV). Actually, the maximum field amplitude occurs at a photon energy of 14.6 keV.

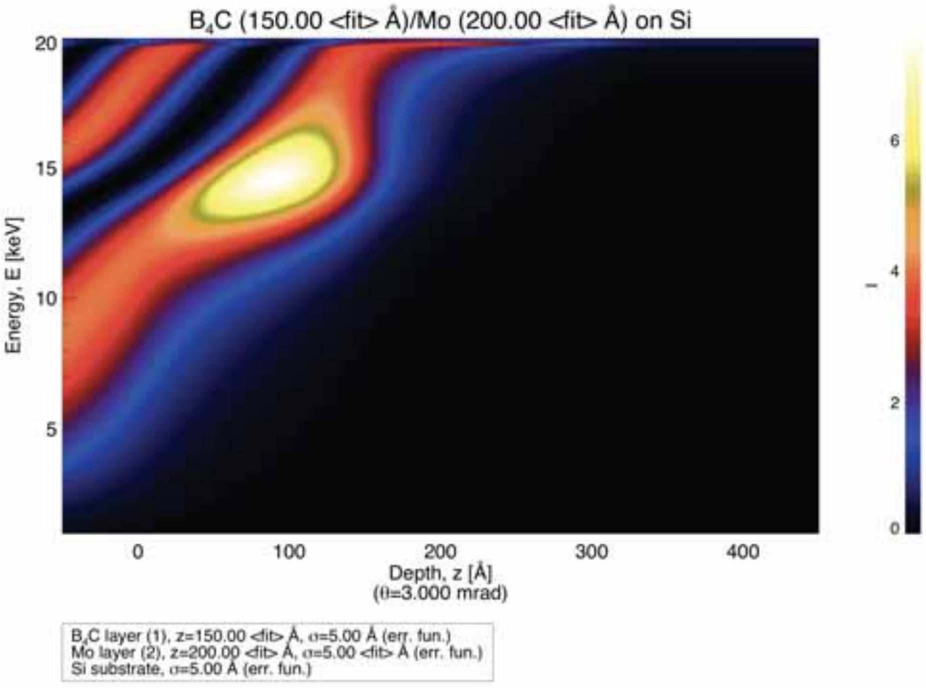

Figure 10: Electrical field intensity as function of the depth (horizontal axis) in the B_4C/Mo - bilayer for 3 mrad grazing incidence angle. The photon energy is given as additional parameter on the vertical axis . The top B_4C layer extends from the surface at z=0 Å to 150 Å and the Mo-layer from z=150 Å to z=250 Å.

The usage of this layer system in the vicinity of the standing wave region may be limited to an attenuated beam operation only. The photon energy range at which the standing wave occurs, can be shifted to higher photon energies by reducing the layer thickness of the B_4C-layer. This has to be balanced with the requirement to cover the drop in the reflectance at the Mo-L edge.

5.3 Coating with high Z materials

Coatings with high Z materials could be used behind a monochromator or without monochromatisation at the end of the Aramis beamlines. A double crystal monochromator reduces the bandwidth and the fluence approximately by a factor ten and at the end of the beamline, the fluence is already diluted due to the large beam size. The large beam size in turn calls for steeper incidence angles to accept the full beam.

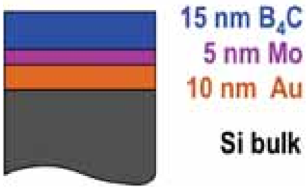

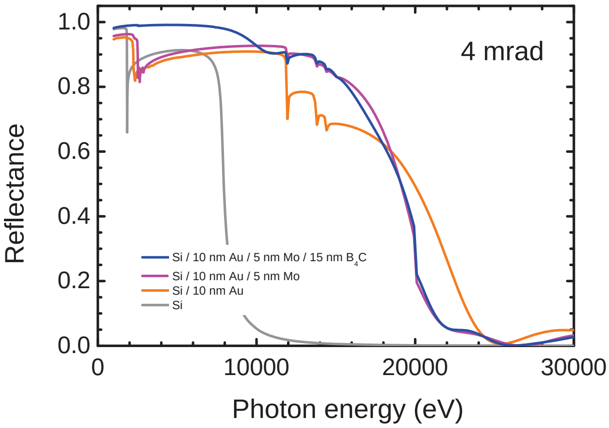

Figure 9: Three layer coating for an incidence angle of 4 mrad.

A three layer system with 10 nm gold directly on the substrate gives a good reflectance up to 20 keV with an incidence angle of 4 mrad. A 5 nm thin molybdenum layer covers the gold L-edges above 12 keV and the gold M-edges above 2000 eV reasonably good without sacrifying to much reflectance at higher energies. The remaining L-edges of molybdenum are again covered by a 10 nm thick top layer of B_4C. Small reductions in the reflectance between 10 keV and 12 keV are due to Kiessig interference fringes in the B_4C-layer and still tolerable.

This layer system could be used with 4 mrad incidence angle on the KB-systems at the end of the beamline.

5.4 Investigations of test-samples

Test samples were prepared by two suppliers, AXO-Dresden and Helmholtz Center Geesthacht on superpolished silicon substrates of one inch diameter. They were investigated at the optics beamline of the SLS[12] for the quality of the individual layers and the critical angles at different energies. Figure 12 shows $(\theta, 2\theta)$-curves taken at 18 keV photon energies for the L- and M-coatings. The data were fitted with the IMD-software [11] to obtain values for layer thickness and roughness.

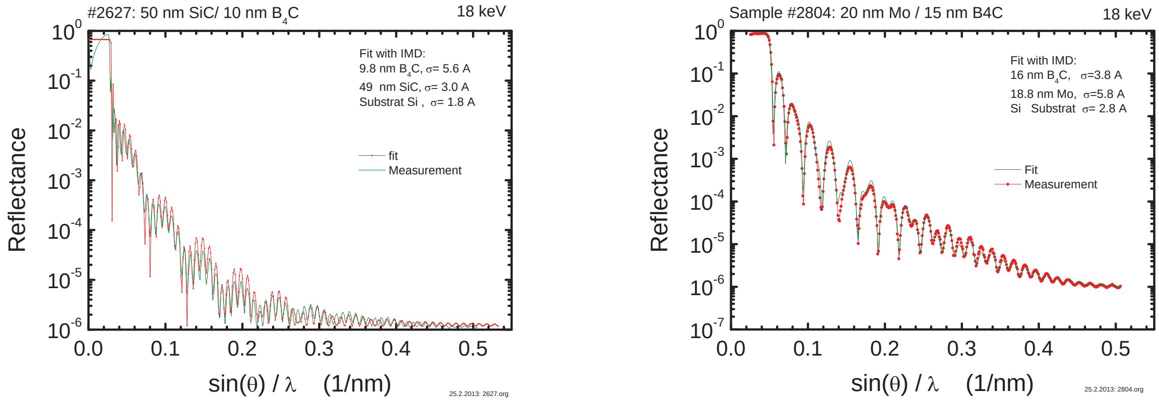

Figure 12: Reflectance of two samples with low-Z (left) and high-Z (right) coatings.

Both samples show well pronounced Kiessig fringes due to interference in the two layers. In the case of the SiC/B$_4$C- system the layers have very different thickness (50 nm vs. 10 nm), and the Kiessig fringes nicely reproduce the ratio of five to one. The obtained layer thickness agree with the design values quite well.

Critical angles are obtained from measurements at different energies and plotted in Figure 13. The data for the critical angle show the angle, at which the reflectance drops to 80% of the maximum value. They are plotted against the photon wavelength and photon energy, respectively. A linear regression is obtained from the wavelength data and plotted in both graphs. It verifies the linear relation according to eqn (3). The slope of the fit is 2.7 mrad/Å for the SiC/B$_4$C-system and 4.6 mrad/Å for the Mo/B$_4$C-system.

This corresponds to a product of critical angle and critical energy of 33 mrad·keV for SiC/B$_4$C-system and 57 mrad·keV for Mo/B$_4$C-system. Preliminary results for coating-H at 18 keV gives 72 mrad·keV.

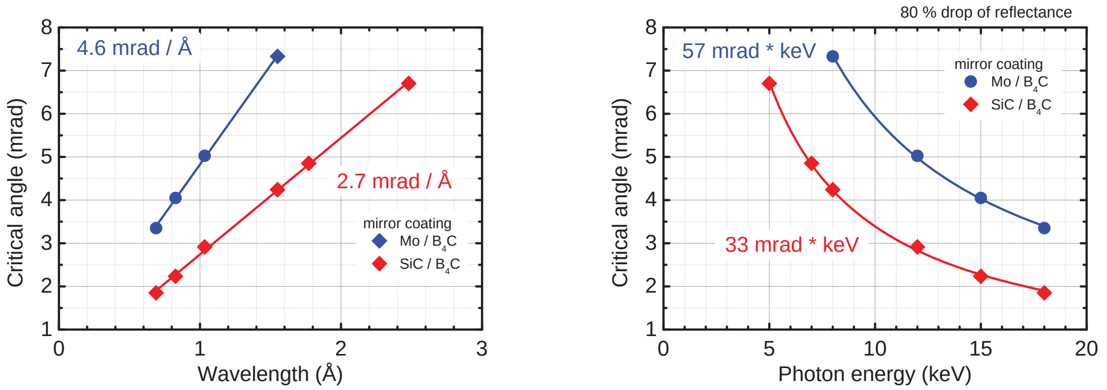

Figure 13: Critical angles for different coatings, measured at the optics beamline of the SLS. The left figure shows the data as function of the wavelength, the right figure as function of the photon energy, respectively.

6 Offset mirrors

The main purpose of the offset mirrors is the distribution of the photon beam to the different end stations. They also serve as radiation safety systems by separating the X-ray beam from the direct bremsstrahlung, generated in the linear accelerator and undulator sections.
Each of the three Aramis beamlines will have a set of two offset mirrors. In the outer two beamlines, the beam is horizontally deflected, whereas in the central beamline the offset mirrors are used in a vertical zig-zag geometry.
Besides these geometric and safety functions, the offset mirrors offer the possibility to manipulate the beam properties in their respective deflection plane. For this, at least the second offset mirror will be realized as bendable plane elliptical mirror to tailor the beam divergence and optimize the illumination of the subsequent optical elements or even the sample. Along with a bendable refocusing mirror a zoom optic can be realized, allowing for a real variation in the focal spot size on the sample at least in one direction. When used without additional optics, the bendable offset mirror can be used to vary the illumination on the sample directly. Due to the small incidence angle, a manipulation of the beam properties perpendicular to the deflection plane is not possible.

The offset mirrors will be motorized to remotely steer the beam through the beamline. The horizontally deflecting mirrors offer the additional possibility to compensate for parasitic horizontal beam motions induced by the crystal monochromators while scanning the photon energy.

The offset mirrors have multiple coatings parallel to their long side, which are selected by a translation of the mirror Figure 15.

6.1 Alignment accuracy

To estimate reasonable values for the alignment accuracy, the impact of mirror motions on the beam position at the end of the beamline is considered and compared to the corresponding beam cross section. For this estimation, it is assumed that the offset mirror is located at a distance of 70 m from the end of the undulator and the beam position is monitored another 100 m downstream, as it is the worst case in the Aramis 3 beamline. The most stringent requirements are imposed by an operation with 200 pC at 12.4 keV, where the rms-divergence is only 1.1 µrad. Due to the long distances and the small beam sizes involved, the reproducibility of the mirror settings must be very high. The design of the mirror chamber should allow for a reproducible setting of the beam position at the end of the beamline to a twentieth of the beam size and the layout of the motorization should foresee a setability of at least a tenth of the reproducibility.

Any vibrational amplitudes should not exceed the level of the setability, while long term drifts, caused by temperature variation should stay on the level of the reproducibility.

Horizontally deflecting mirrors

Two Aramis beamlines employ horizontally deflecting offset mirrors. Both mirrors within one set deflect the beam in the same direction. The geometry and the coordinate system are depicted in Figure 14. Values for adjustment ranges, reproducibility and setability are summarized in Table 3.

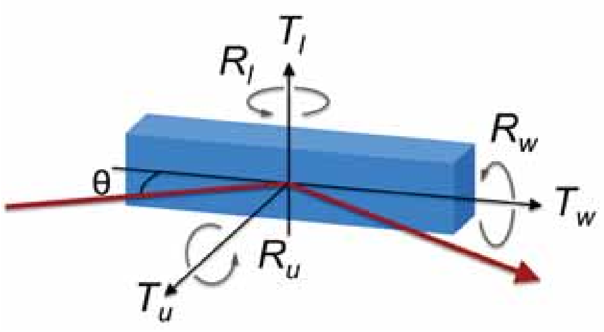

Figure 14: Coordinate system at horizontal deflecting mirrors and denotation of the mirror motions. The incidence angle θ is in the order of 3 mrad.

With the considerations given above, the reproducibility of the pitch should be 0.05 µrad. The total range of the pitch must be large enough to allow for a beam based alignment, starting from the pre aligned mirror. For the bendable mirror, the pitch is also used to compensate for parasitic motions induced by the bending mechanism.

The impact of the roll angle (R_W) onto the beam position is reduced by the incidence angle on the mirror. With a grazing incidence angle of 3 mrad, the reproducibility of the roll should be 15 µrad.

The yaw angle (R_U) specifies the rotation around the surface normal. Plan mirrors are insensitive to this movement. To estimate the accuracy, an elliptical mirror is used to image the source onto the sample. The alignment should not increase the spot size by more than 10%. From this an accuracy of 0.1 mrad is sufficient.

The offset mirrors will be coated with multiple coatings parallel to their long side. The selection is accomplished by a vertical translation of the mirror with an accuracy of a tenth of the beam cross section. This results in a value of approximately 10 µm for the vertical translation(T_Z). The offset mirrors have to be retractable to let the beam pass for the other beamlines. This can be accomplished by the vertical motion, which has already a large range or by a horizontal translation (T_U).

A horizontal translation perpendicular to the incident beam shifts the beam pattern along the mirror surface. This movement should have the same accuracy as the vertical translation.

Alignment, motion	Reproducibility	Setability	Range
R_l, Pitch (μrad)	0.05	0.005	± 50
R_w, Roll (μrad)	15	1.5	-1 000 - 45 000
R_u, Yaw (μrad)	100	10	± 500
T_l, Vert. translation (μm)	10	1	-50 000 - + 10 000
T_u, Hor. translation (μm)	10	1	-2 000 - + 4000

Table 3: Accuracy and setability of the horizontally deflecting offset mirrors.

The horizontal translation in the beam direction has no significant impact on the beam properties. With the very grazing incidence angle, the beam pattern extends over several tenth or hundreds of millimeters. The alignment of the mirror along this axis will be made manually during the installation on air.

6.2 Geometrical size of the offset mirrors

The necessary length of the mirrors depends on the divergence of the FEL-beam, the distance from the undulator to the mirror and the incidence angle. Floorspace considerations in the building request the offset mirrors at a distance of approximately 65 m - 75 m from the end of the undulator.

The layout of the offset mirrors has to account for the wavelength dependences of the beam divergence and the critical angle, respectively. Both decrease with decreasing wavelength and an optimum solution in terms of mirror length would be a variable incidence angle. Although this may be feasible for the Aramis 2 beamline with vertical offset mirrors in the zig-zag geometry, this is not feasible for the Aramis 1 and Aramis 2 beamlines, where both mirrors deflect into the same direction and the total deflection angle must stay fixed.

In a setup with fixed incidence angle, the maximum tolerable incidence angle is determined at the high energy limit. With the mirror coatings discussed in section 5.4 an incidence angle of 3 mrad gives a reasonable compromise between photon energy range and spatial separation of the beamlines. The necessary mirror length is then determined by the lowest photon energy and the corresponding beam divergence.
In the 200 pC mode, the largest beam size at the offset mirror is about 0.45 mm (rms), see Table 1. To accept 5σ of the beam with a grazing incidence angle of 3 mrad the mirror should have an optical surface of at least 750 mm. With this length the offset mirrors cover the full photon energy range down to 1800 eV.

Figure 15 shows a possible mirror geometry with two different coatings and an uncoated area of bulk silicon in the center. The end parts of the mirror are thinned to allow for clamping the mirror in the bender mechanism.

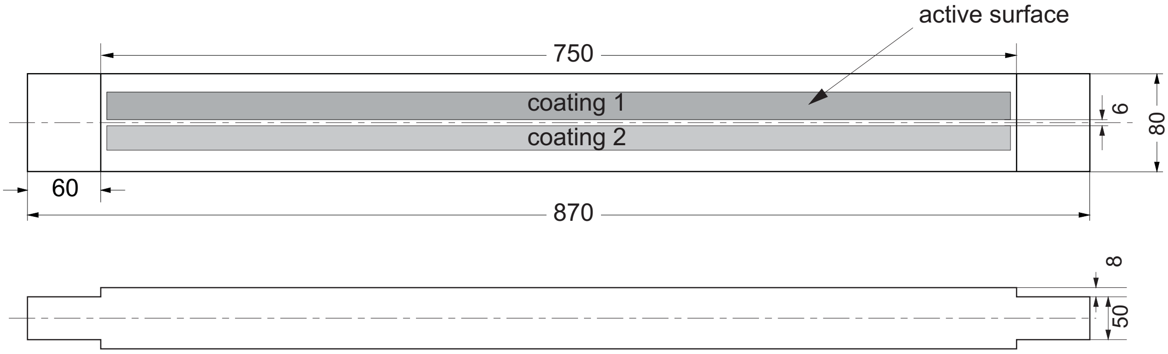

Figure 15: Geometry of the offset mirror. The mirror has two coatings separated by a small uncoated area of bulk silicon. The dimensions are in millimeter.

Mirrors with 1000 mm length would be necessary to cover the lowest photon energy range even in the 10 pC operation mode, but ultra precise surfaces fabrication is currently feasible only up to a mirror length of 800 mm. This may compromise the performance of the beamline in the 10 pC mode below 2500 eV.

6.3 Mirror chamber

The mirror support and chamber must guarantee a stiff and stable mounting of the mirrors and ensure an efficient suppression of ambient perturbances.

The mirror system of the P11 beamline at PETRA III as shown in Figure 16 fits nearly perfectly to the requirements of the SwissFEL offset mirrors and is envisaged as blueprint for the Aramis offset mirror chambers.

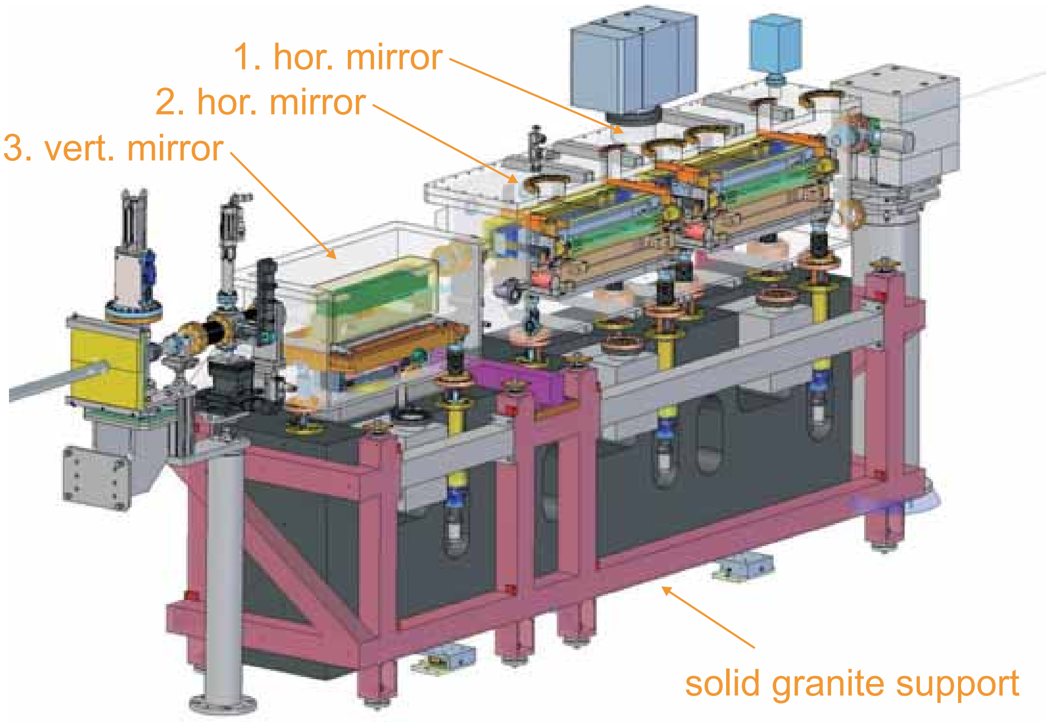

Figure 16: Mirror chamber of the P11 beamline at PETRA for two horizontally and one vertically deflecting mirrors. Figure courtesy of A. Meents [13].

The mirror length of the P11-mirrors with an optical surface length of 650 mm is slightly shorter than the maximum requirements derived for Aramis beamline with 750 mm length. Detailed considerations have to show, if the design can be adapted to longer mirrors without sacrificing accuracy, or if the operation at lowest photon energies constrains to an acceptance of less than 5σ of the beam.

6.4 Arrangement of offset mirrors

The Aramis 1 and Aramis 3 beamlines use both a pair of horizontally deflecting offset mirrors (HOMS), which must be moved in and out of the beam to give way for the direct Aramis 2 beamline. The vertically deflecting mirrors of the Aramis 2 beamline are positioned downstream of the horizontal offset mirrors and do not interfere with Aramis1 and Aramis3 beamline.

The four HOMS mirrors should be arranged in a way to minimize their travel range for moving in and out. This can be done either in vertical or horizontal direction.

Horizontal switching

If switching is performed in the horizontal direction, The mirrors could be arranged interleaved, where the mirrors deflect alternately left and right, or sequential, where the mirrors of either beamline are grouped together as shown in Figure 17.
In the sequential arrangement, the separation of the Aramis 1 beam from the Aramis 3 mirrors is already large enough to let the Aramis 3 mirrors at their working position when Aramis 1 is operating. The Aramis 3 mirrors must only be moved by approximately 10 mm, when Aramis 2 is operating. In this arrangement, the two mirrors of each beamline could be arranged in common chambers, as it is already realized in the PETRA P11 mirror chamber design. Both mirrors would then be mounted on a common granite and relative motions could be minimized.
In the interleaved arrangement, the second mirrors of the Aramis 1 and 3 beamline must be retracted by 66 mm to free the path for Aramis 2, while for operation of Aramis 1 and 3 the beam separation may already be large enough, to remain the second mirrors untouched. Placing the mirrors closer to each other reduces the necessary travel distance, but the second mirror still has to move by approximately 45 mm.

If the design of the mirror chamber and the bender mechanisms facilitates a configuration where the Aramis 2 beam can pass the mirrors of Aramis 3 system, as shown in the sequential arrangement, this solution offers the minimum travel distances and should be selected for the Aramis beamlines.

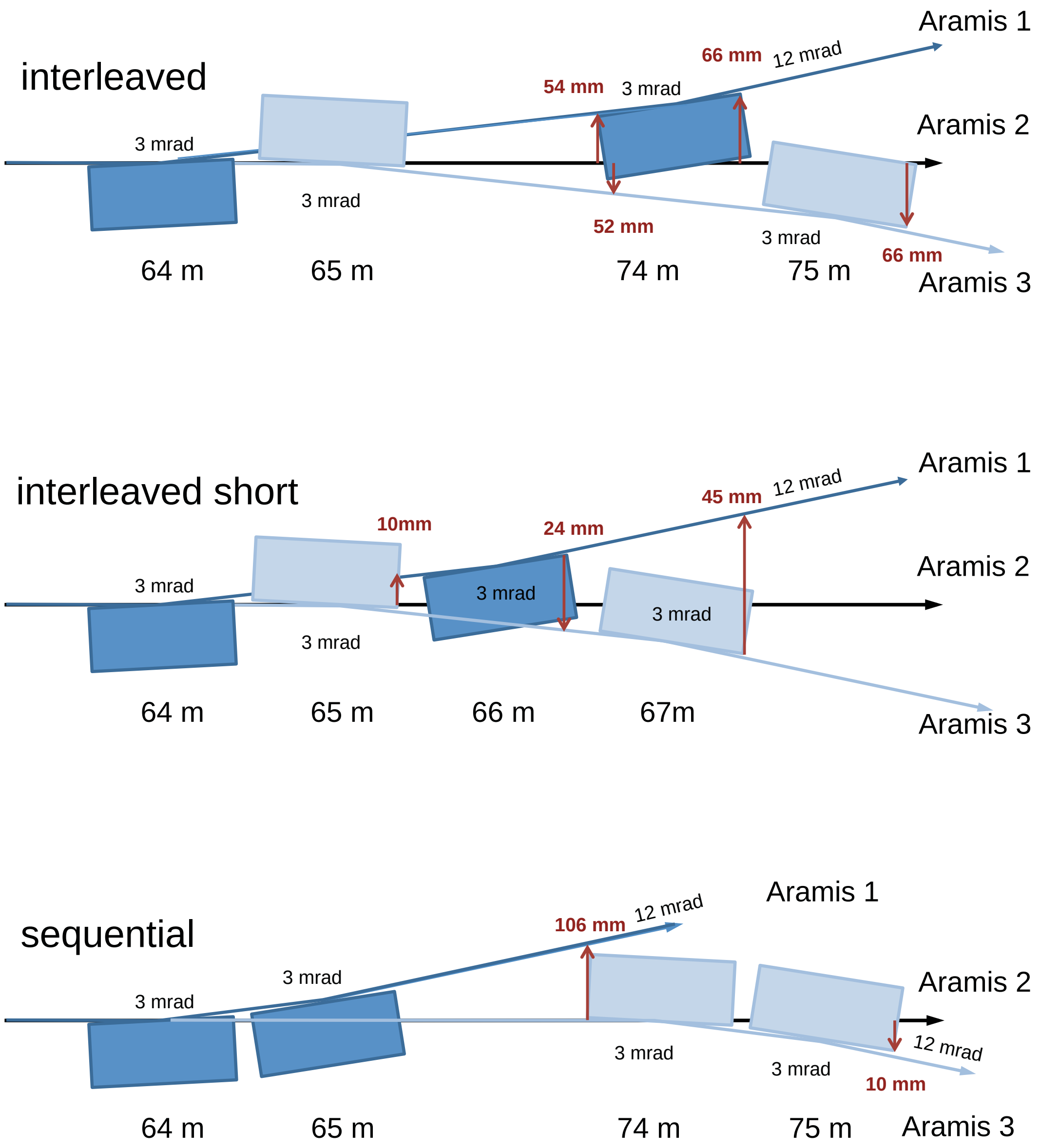

Figure 17: Arrangement of the four horizontally deflecting mirrors of the Aramis 1 and Aramis 3 beamline.
Top: interleaved arrangement, where the mirrors alternately deflect left and right.
Middle: Interleaved arrangement with mirrors close together.
Bottom: Sequential arrangement, where the mirrors of each beamline are grouped together.

Attenuation	10^{-1}	10^{-2}	10^{-3}
Thickness (mm) .... B_4C	4.10	8.19	12.3
Third order attenuation	0.94	0.89	0.84
Thickness (mm) .... silicon	0.16	0.32	0.48
Third order attenuation	0.92	0.84	0.78

Table 4: Absorber thickness for attenuations at 8 keV.

Vertical switching

If switching is performed in the vertical direction, the arrangement of the mirrors does not affect the travel distance. The vertical motion is already foreseen, to change between multiple coatings with a travel range of approximately ±5 mm. To move the mirrors in and out, the travel range must be increased in one direction to at least the half width of the mirror, i.e. 40 mm.

7 Absorbers

Solid attenuators will reduce the intensity of the photon beam in a controlled way without deteriorating the wavefront of the FEL-beam. An ideal materials would be B_4C. Silicon or carbon could be an alternative, if boron carbide cannot cannot be fabricated with the required quality concerning homogeneity or surface accuracy. The attenuation factor is controlled via the thickness of the absorber as shown in Table 4 and attenuators with various thickness can be inserted in the beam.
The attenuation of an absorber depends on the photon energy and is generally stronger for lower photon energies. The higher harmonics of the radiation suffer therefore less attenuation than the fundamental and any absorber will not only attenuate the fundamental photon energy but also increase the relative content of the higher order light. Table 4 shows the thickness of silicon and B_4C absorbers for a given attenuation factor as well as the attenuation factors for the third harmonic. At a fundamental photon energy of 8 keV, the third harmonic suffers virtually no absorption and passes the absorber more or less unhindered. The variation of the attenuation with photon energy and the enhancement of the third order content is shown in Figure 18 as a function of photon energy for absorbers of silicon and B_4C, respectively. The relative enhancement of the third order content limits the maximum achievable attenuation factor for the fundamental.

The situation is somewhat improved for energies, where absorbers show an absorbtion edge just below the third harmonic.

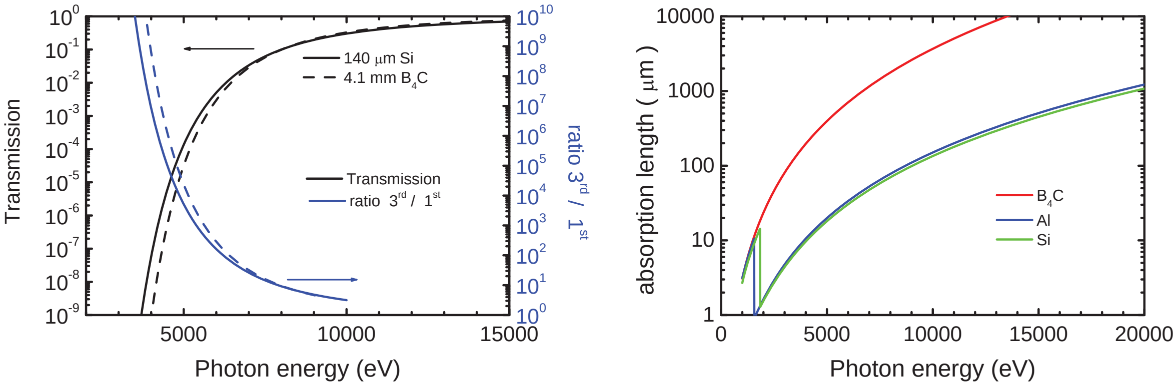

Figure 18: Left: Transmission through solid state absorbers of 140 µm silicon and 4.1 mm B_4C and corresponding enhancement of the third harmonic with respect to the fundamental. Right: attenuation length of some low-Z materials as function of the photon energy.

The homogeneity and thickness of the absorber must not deteriorate the wave front. For this, the effective thickness across the FEL-beam must be constant. The necessary accuracy can be deduced from a calculation of the phase change $\Delta\phi$ induced by a variation of the absorber thickness Δd and the index of refraction eqn (1):

$$\Delta\phi = 2\pi\frac{(1-n)}{\lambda}\Delta d \approx n_e r_e \lambda \Delta d \; . \qquad (12)$$

According to the Marechal criterion, eqn (9), this should stay below $2\pi/14$. At 8 keV, the effective thickness of the B_4C and silicon absorber must not vary by more than 1.5 µm (rms).

For a given thickness variation, the phase change according to eqn (12) is proportional to the wavelength of the radiation. The impact of thickness variations on the wavefront are therefore more critical towards lower photon energies.

8 Focusing scheme

Many experiments call for a variable beam spot on the sample either to optimize the overlap with a pump laser or to vary the fluence on the sample. The simplest way to achieve this is to move the sample out of the focal point. Although this is the most straightforward approach, it becomes difficult when the experimental station is complex and bulky or the sample has to be aligned with respect to other equipment as e.g. to a pump laser. A variation of the illuminated area on the sample by means of the beamline without moving the sample would simplify the design of the end stations. This can be achieved by various methods.

Arrays of compound refractive lenses are commonly used in hard X-ray instrumentation to form focal spots of medium sizes [14]. Their focal distance and thus the diameter of the beam spot at the end station can easily be varied by introducing more or less lenses into the beam [15]. This is also a way to compensate their chromaticity, i.e. the variation of the focal length with the photon energy. Compound refractive lenses with rotational symmetric parabolic profiles are 2-dimensional focusing devices and uncritical to align. Due to the high absorption of the lens-material, CRLs are mainly used above 5 keV. The Aramis beamlines foresees them to provide medium size focal spots.

Focusing with reflective mirrors is technically more complex but offers an achromatic focusing scheme over a wide photon energy range that could in principle focus down to a few nanometers [16]. Due to the very grazing incidence angle, focusing with one mirror is only one dimensional. To form a two dimensional focus, two mirrors are arranged perpendicular to each other. This can be done either sequential in the Kirkpatrick-Baez configuration [3] or in the Montel configuration, where both mirrors are rigidly mounted side by side in a very compact arrangement [17]. The Montel configuration offers shorter focal lengths and thus stronger demagnifications, at least for one direction. Montel mirrors are therefore candidates for applications with very strong demagnifications on short distances. Their compact mechanical design and the rigid connection makes it difficult to change their radius of curvature. Montel optics are therefore used with fixed focal lengths.
The additional space around the mirrors in the KB-mounting can be used for the installation of bender mechanisms to vary the focal lengths. Changing the geometry of the mirror surface by actuators allows for a continuous and online variation of the illuminated area at the sample position. This is appreciated by many experiments and widely-used in beamline instrumentations. For the same reason, the experimental stations at SwissFEL favor the flexibility of the bendable KB-systems against the compact architecture of the Montel-mirrors. The Aramis beamline layout foresees the KB-systems alternatively to the compound refractive lenses.

The size of the illuminated area on the sample can be varied by changing the radius of curvature of the offset mirror and/or the radius of the corresponding mirror in the KB-system. As an example, Figure 20 shows the achievable horizontal spot sizes for the Aramis 1 beamline, when the horizontal deflecting offset mirror is at 74 m, the horizontal deflecting KB-mirror at 122 m and the sample distance from the center of the horizontal focusing mirror is 1.8 m.

With flat mirrors, i.e. zero curvature, the horizontal beam spot size at the sample is about 100 µm (rms). Increasing the curvature of one or both mirrors reduces the spot size. Without aberrations, the smallest horizontal spot size of 260 nm (rms) occurs when the first mirror is flat and all of the focusing is done by the last mirror.

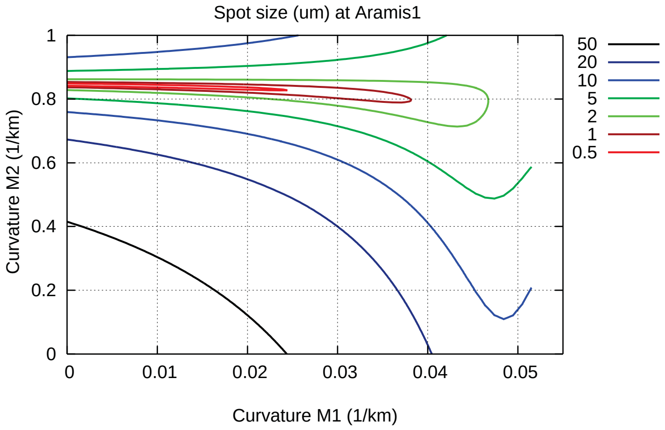

Figure 19: Size of the illuminated area at the sample as function of the curvature of mirror M_1 and M_2. The calculation was done with ideal geometrical optics. The source parameter are for 200 pC operation and a photon energy of 12.4 keV. With plan elements the horizontal spot size of 100 µm (rms) corresponds to the beam size of the free propagating beam.

Focusing with only the last mirror gives the strongest demagnification and therefore the smallest spot size. At small photon energies, where the FEL-beam has the widest divergence, the last mirror may not be large enough and therefore overfilled. Besides a loss of photon flux, the limited aperture may lead to artifacts in the image due to diffraction at the edges. A moderate pre focusing with the first mirror or CPLs could reduce the beam divergence avoiding this unwanted effects.

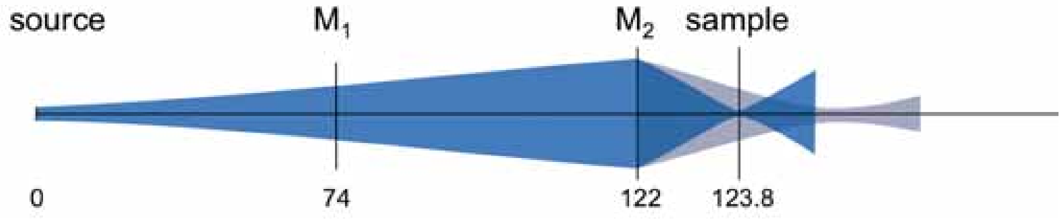

Figure 20: Varying the size of the illuminated area on the sample by defocusing with the last mirror.

Experiments with less stringent requirements on spot size may operate the beamline without the refocusing mirrors. In this mode, the spot size can be adapted by means of the first mirror. With the given distances from source to mirror and sample, the minimum spot size is about 100 µm.

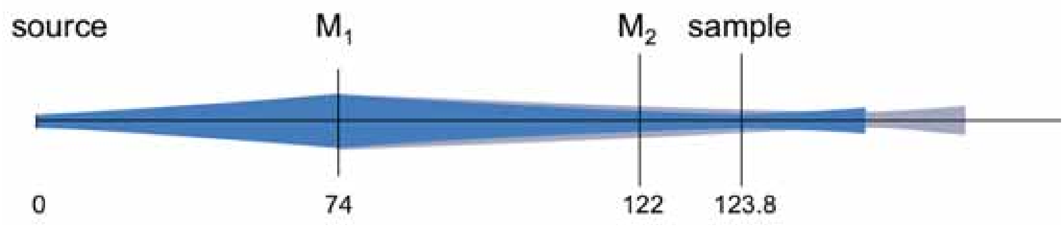

Figure 21: Varying the size of the illuminated area on the sample by defocusing with the first mirror.

Both methods use focusing elements with variable focal length to alter the size of the illuminated area on the sample by shifting the focal plane out of the sample location. This may lead to the appearance or the enhancement of already existing inhomogeneities in the spot pattern. This inhomogeneities are caused by residual imperfections of the mirror surfaces or the material of the compound refractive lenses which become more prominent when the focal plane shifts away from the sample position. This could limit the practical use of this single focusing scheme.

Distributing the focal power onto two optical elements separated adequately in space, would allow for a zoom objective that keeps the focus on the sample while its size could be changed independently.

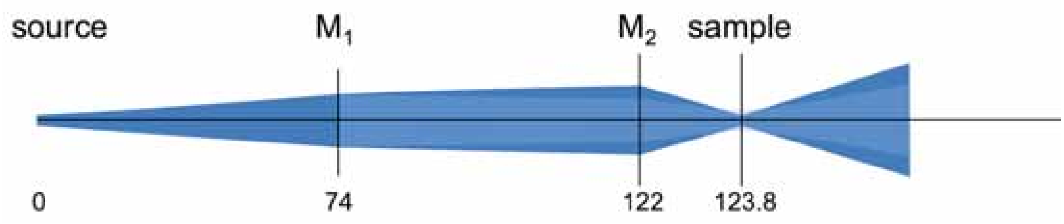

Figure 22: Focusing with both mirrors keeps focus with variable size on sample

With this option, care must be taken not to focus the FEL beam onto the surface of the second mirror.

Due to the small incidence angles, a manipulation of the beam parameters and therefore the focal spot size is only feasible in the deflection plane of the mirrors.

9 Physical optics simulations from start-to-end

The optics layout the Aramis beamlines is based on the classical geometrical optics approach. The chosen distances and angles result from various constraints like single shot damage, reflectivity, spatial separation of experiments etc..

The beam size and focus properties at various positions at the beamline has been simulated by physical optics calculations using the codes GENESIS [18] and PHASE [19].

As starting point for the physical optics calculations, the electical field distribution at the saturation point of the Aramis undulator was calculated with the code GENESIS, provided by S. Reiche. The electrical field was then propagated through the optical system by taking into account the longitudinal and transverse coherence properties of the FEL radiation. Results are shown on Figures 23 and 24.

The simulation were made for a photon energy of 12.4 keV and 200 pC bunch charge. In a first step, the field was propagated into the front end area 60 m downstream the undulator, just before the first offset mirrors. The initial FWHM beam width of $52\,\mu\mathrm{m}$ increased to $124\,\mu\mathrm{m}$. The numbers correspond to a rms source size of about $22\,\mu\mathrm{m}$ and a divergence of about $1\,\mu\mathrm{rad}$. In the next step, the fields were propagated across a flat offset mirror at 64 m[4] to the experimental station. Calculations were done with and without KB focusing (Figure 24). In the unfocused mode a FWHM beam size of $240\,\mu\mathrm{m}$ is expected at 124 m. This gives also the upper limit for the beam size at this photon energy. Figure 24 right shows the simulation for the focusing mode with a KB mirror system. For this, a horizontally deflecting plane-elliptical mirror at 122 m followed by a vertically deflecting plane-elliptical mirror at 123 m was assumed. This corresponds to a horizontal and vertical focusing distance of 2 m and 1 m respectively. The outcome of the calculation is a FWHM beam size of $470 \times 530\,\mathrm{nm}^2$ ($v \times h$). This beam size is in good agreement with the value obtained in geometrical optics calculation.

In a second simulation, the influence of manufacturing tolerances (slope errors) were investigated. Instead of a perfectly flat offset mirror, a real mirror with a measured height profile was considered. The mirror, with a very good slope error of $0.1\,\mu\mathrm{rad}$ (rms) is installed at an existing FEL beamline.

Some minor structures were observed in the beam shape, but only marginal changes occured in the width and the position of the centroid. Though the result is not a full proof, it gives confidence that the best quality of commercially available optics will not degrade the beamline performance.

---

[4] For the simulation we simplified the proposed design of two mirrors in sequence and considered only one offset mirror. With 3 mrad grazing angle the illuminated area is in the order of 100 mm and $\ll 650\,\mathrm{mm}$ the planned length of the mirrors i.e. diffraction effects from the mirror edges are not expected.

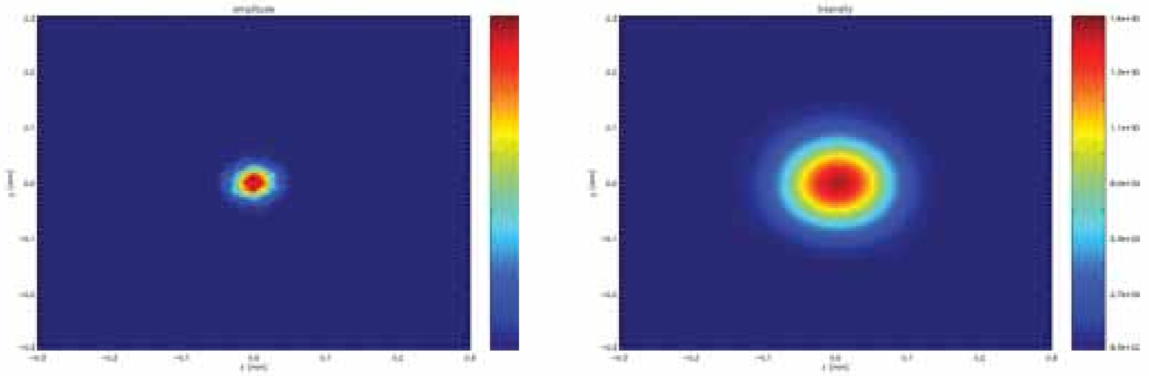

Figure 23: X-ray source for a photon energy of 12.4 keV. Left: X-ray intensity at the end of the Aramis undulator (saturation point). Extracted from an electrical field calculation by S. Reiche with GENESIS. Beam size: $52\,\mu\mathrm{m}$ FWHM. Right: Intensity at 60 m downstream the undulator in the front end. Electrical field propagated with PHASE. Beam size: $124\,\mu\mathrm{m}$ FWHM.

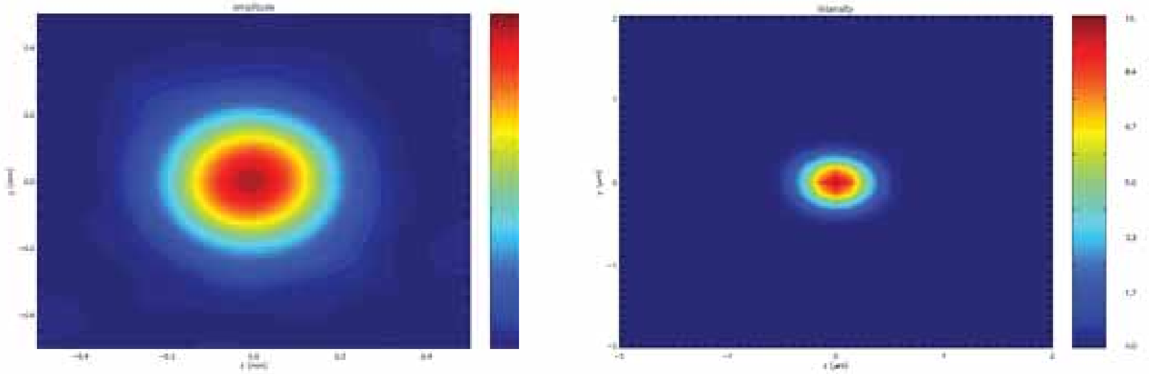

Figure 24: X-ray intensity at the experimental station 124 m downstream the undulator. Photon energy 12.4 keV, horizontally deflecting flat offset mirror at 64 m. Electrical field propagation with PHASE. Left: unfocused beam, KB's retracted, no CRL's. Beam size: $240\,\mu\mathrm{m}$ FWHM. Right: with KB system, the vertical and horizontal focusing distance was 1 and 2 m respectively. Beam size: $470 \times 530\,\mathrm{nm}^2$ FWHM ($v \times h$). Note the different scale at the right image.

10 Operation modes

Operation with monochromatised radiation or pink beam will be available in the Aramis 1 and Aramis 2 beamlines. Switching between both modes should be performed without the need for a readjustment of the experiment. Therefore the monochromatised and the pink beam should b enter the experimental station at the same position and with the same direction.

10.1 Aramis 2

In the Aramis 2 beamline, the offset mirrors deflect the beam vertically in a zigzag geometry with the same offset as the subsequent DCM. In monochromatised mode, the offset mirrors are removed and the DCM separates the monochromatised beam from the direct direction by the same vertical amount, see Figure 25.

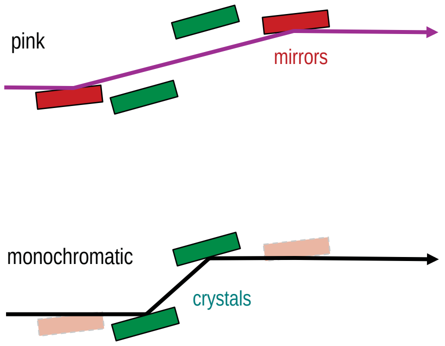

Figure 25: Monochromatic and pink beam operation in the Aramis 2 beamline

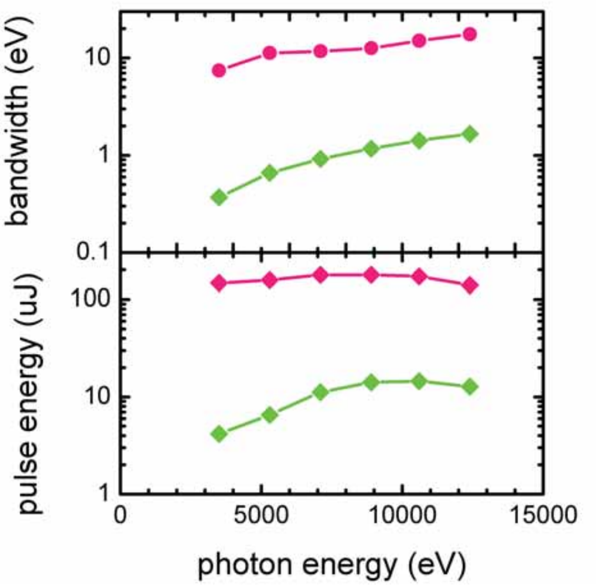

The Aramis 2 beamline can operate with the monochromator as the only optical element in the beam. In this operation mode, the DCM will introduce the same vertical offset to the beam as the vertical offset mirrors enabling the same beam direction for the operation with or without monochromator. For radiation safety reasons, the separation of the transmitted beam from the direct beam must be large enough to shield the high energy Bremsstrahlung and a offset of 20 mm is foreseen for the DCM and the VOMs. The beamline was ray traced with the code RAY[20] to get values for for beam width and pulse energy. The results are shown in Figure 26 for both modes.

10.2 Aramis 1

In the Aramis 1 beamline the offset mirrors deflect the beam horizontally with an angle of 12 mrad. They cannot be used to compensate the vertical offset in the subsequent DCM and a pair of additional mirrors are used for that.

A four bounce scheme with a DCM and an additional pair of vertically deflecting mirrors is considered, see Figure 26. The DCM could be a copy of the Aramis 1 monochromator for the full photon energy range. Although the DCM is designed with a fixed exit beam, the gap between the crystals and thus the beam offset could be varied within certain limits under computer control. On the other hand, the mirror chamber design foresees a vertical translation and a pitch change of the mirrors. By varying the beam height between the DCM and the mirror chamber, the pitch at the mirrors can be varied without changing the horizontal distance of the two mirrors. At low photon energies the beam will have the maximum offset and the mirrors deflect with the largest deflection angle. This improves high harmonic rejection at the low photon energies. With increasing photon energy, the beam offset will decrease and the deflection angle at the mirrors gets more grazing, improving the transmission at hight photon energies.

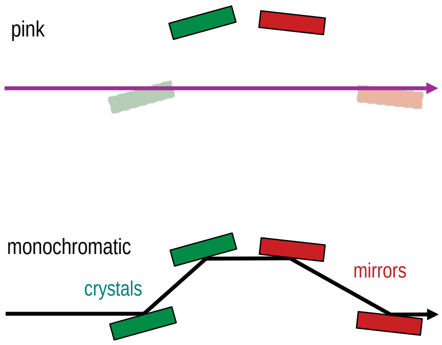

Figure 26: A four bounce scheme with a DCM and a pair of mirrors to brings the beam back to its original direction in the Aramis 1 beamline.

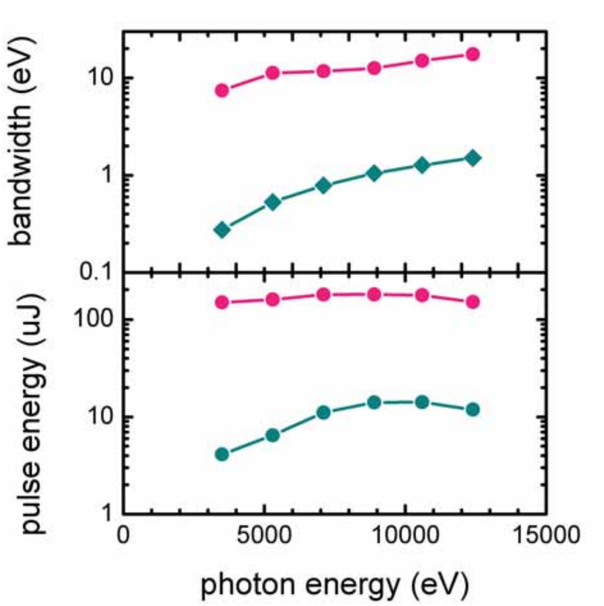

It is assumed, that operation with pink beam will be the standard mode for Aramis 1 and monochromatisation with a DCM is rarely used. Monochromatisation by the DCM may become even less necessary, when the self seeding operation of the FEL becomes available. The retractable four bounce scheme minimizes the number of optical elements in the main, pink operation mode and offers the best beam conditions.

An alternative solution would be a configuration with two double crystal monochromators where the second monochromator brings the beam back to the original direction as shown in Figure 27. But the set up of two DCM adds a high degree of complexity to the beamline and is not considered. A scheme with two two channel cut crystals would allow for an easier setup. The variable beam height after the first channel cut crystal is compensated by the second one. A serious challenge with channel cut crystal is the limited surface quality inside the channel. The surface cannot be polished as good as on regular crystals and could therefore lead to the formation of speckle pattern in the beam cross section. Artificial channel cuts address this problem by composing the single channel cut by two single crystals after surface polishing.

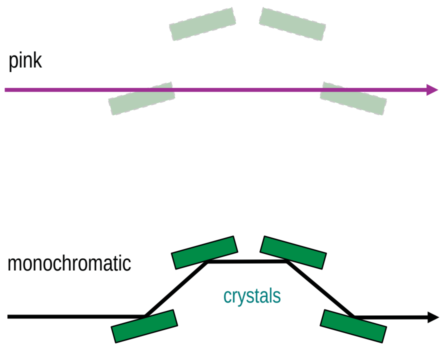

Figure 27: Four crystal option for Aramis 1 beamline.

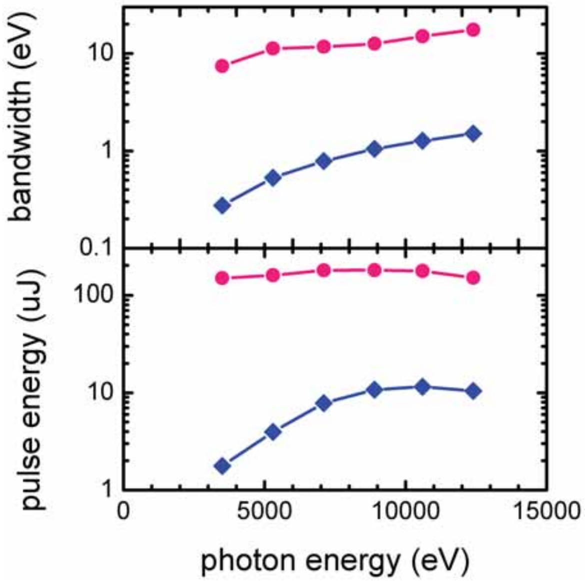

11 Monochromator

Double crystal monochromators (DCM) with fixed exit direction disperse the beam in the Aramis 1 and 2 beamlines. The crystal pairs are set in parallel configuration and deflect the beam vertically. The beam offset introduced by this geometry will be 20mm.

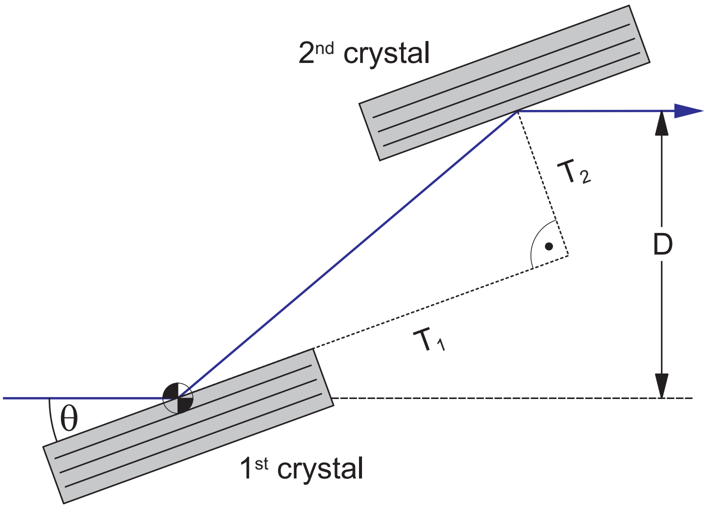

Figure 28: Side view of the crystal setup in the DCM.

The monochromators will be equipped with three crystal pairs. Silicon-(111) crystals operates from 2.0 keV to 20 keV with moderate resolution. A silicon-(311) gives better energy resolution above 4 keV, but pulse energy is reduced according to the lower bandwidth and the lower diffraction efficiency as shown in Figure 31. The lowest photon energy of the Aramis-FEL, 1770 eV, cannot be covered with silicon crystals. A pair of InSb (111) crystals has to be used to access the photon energy range down to 1770 eV without damage as shown in Figure 5. The upper photon energy limit of the InSb-crystals is given by the Indium $2p_{3/2}$-edge at approx. 3700eV .

The range of Bragg-angles are determined by the operation range of the Si-111 crystals and are shown in Figure 29, some numerical values in the range from 5.5° to 82°are given in the table.

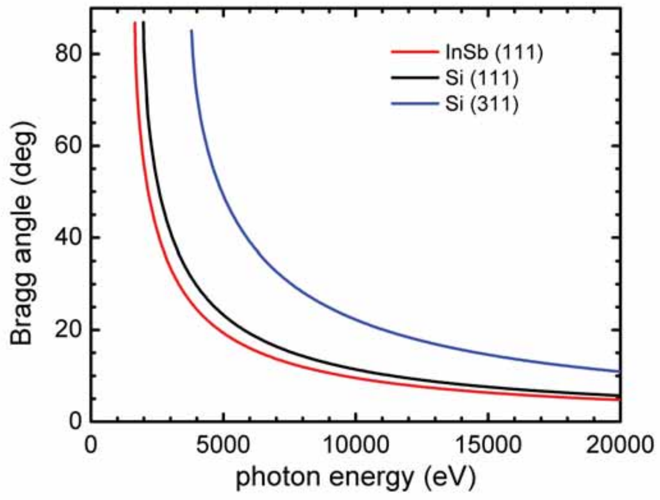

Photon energy (eV)	Si (111)	InSb (111)
1770	-	69.4°
2000	81.3°	56.0°
2100	70.3°	52.1°
1400	9.2°	-
15000	7.6°	-
20000	5.7°	-

Figure 29: Bragg angles for silicon (111), (311) and InSb (111) reflections. Lattice spacings are 0.5431020504 nm for silicon and 0.6479 nm for InSb, respectively.

The crystal pairs are mounted on a common, rotatable base plate to set the Bragg-angles for both crystals as shown in Figure 28. To maintain a fixed beam height after the DCM, the second crystal has to translate according to

$$T_1 = \frac{D}{2\sin\theta} \qquad \text{and} \qquad T_2 = \frac{D}{2\cos\theta}\ . \tag{13}$$

The length of the crystals are minimized when the the first crystal is aligned with its surface lying in the rotation axes, while the second crystal is mounted on a translation stage to keep the beam offset constant. The translation of the second crystal parallel, T_1, and perpendicular, T_2, to the surface of the first crystal is shown in Figure 30. The positions for selected Bragg angles are marked with bullets.

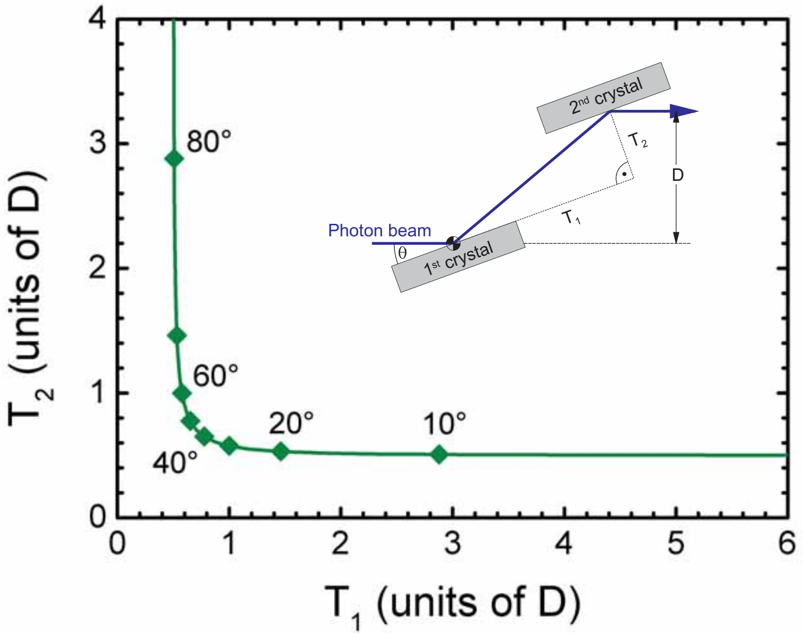

Figure 30: Trajectory of the second mirror normalized to the beam separation D. Positions are marked for Bragg angles θ in 10° steps.

The two dimensional translation of the second crystal can be replaced by a single translation if the crystal size is increased. In this mode, the intersection point of the beam on the second crystal moves along its surface while the beam offset and direction stay constant. This mode could be important for (continuous) energy scans over a limited photon energy range.

If the rotation axes is placed in-between both crystals, the beam moves along both surfaces and both crystals have to be larger. As the crystal have to have a certain size anyway, this could be a way to increase the range in which only one crystal translation is sufficient to keep the beam offset constant.

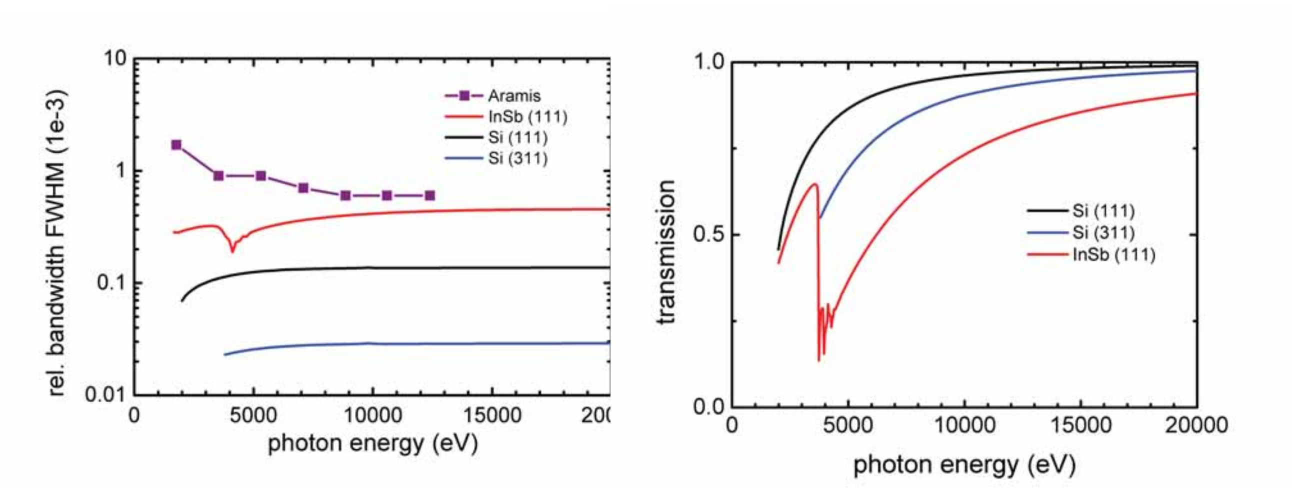

Figure 31: Resolving power and transmission for three crystal pairs.

Detuning the angular setting of the two crystals reduces not only the intensity of the first diffraction order. As the Darwin width of the third order is smaller than the corresponding width of the first diffraction order, the ratio of third order to first order decreases more rapidly than the intensity of the first diffraction order. This offers a comfortable way to reduce the higher order content of the diffracted radiation [21]. The drawback of the detuning is not only a reduced photon flux in first order but also an increased sensitivity to angular vibrations of the crystals. Any angular vibration translate directly into an intensity fluctuation, which becomes larger as the overlap of the darwin curves narrows.

11.1 Wavelength scanning

Wavelength scanning is achieved by a coupled motion of the pitch and the linear translations of the crystals. The layout of the motors determine the scan speed. Scan speeds of a few 100 eV per seconds may be realized by stepper motors. Faster motions with some 1000 eV/s may require servo motors. This fast scan speeds may put some constrains on the mechanical design.

11.2 Large Offset Monochromators

Large Offset Monochromators are foreseen for phase 2 installation and allow for a parallel usage of the transmitted and diffracted beam.

The LOM uses a thin diamond crystal in Laue-geometry as beam splitter and a second crystal as deflecting element. The second crystal could operate in either Bragg- or Laue-geometry. It deflects the beam by the same amount as the first crystal and ensures a photon energy independent direction of the diffracted beam. The scheme for a double Laue-diffraction is shown in Figure 32. Although it is not mandatory, the LOM will be installed in a horizontal deflection geometry.

A large distance between the two crystal is required to gain enough space for the experimental station. The concept of Large offset monochromators is already realized at the LCLS with diamond crystals and an offset of 0.6 m and the PETRA III, with silicon crystals and offsets of 0.5 m and 1.25 m, respectively [22, 23]. The feasibility of monochromators utilizing diamond crystals has been demonstrated at synchrotron storage rings under high cw-power load [24, 25].

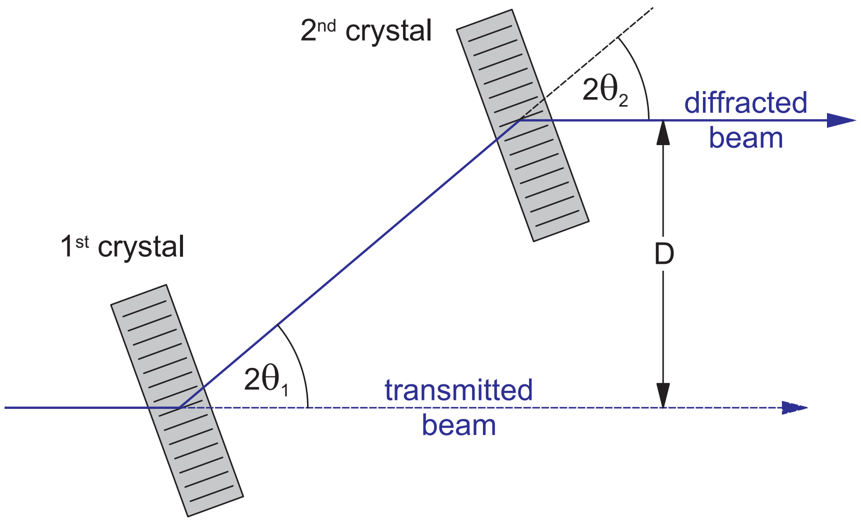

Figure 32: Top view of the Large Offset Monochromators with beam separation D in the order of 0.5 m.

A temperature difference between the two crystals, with an accompanying change in the lattice parameter, cause a detuning of the two crystals and the overlap of the two Darwin-curves reduces or even vanishes. This may be a favorable effect to reduce the bandwidth or the higher harmonic content, but, in any case lead to a loss in throughput. The detuning can be compensated by a angular readjustment of one crystal which recovers the transmission, but lead to a angular shift of the diffracted beam and to a corresponding change of beam position at the experiment.

From the Bragg-equation

$$n\lambda = 2d \sin\theta \tag{14}$$

the angular shift can be calculated according to

$$\Delta\theta = \alpha_T \tan\theta \cdot \Delta T \tag{15}$$

The sensitivity to temperature changes increases with increasing Bragg-angle and is most sensitive at low photon energies. At these energies the concept of the LOM is in any case no more functioning due to the high absorption of the transmitted beam. Figure 33 shows the Bragg angles, the Darwin width and the angular change for diamond-(111) reflection.

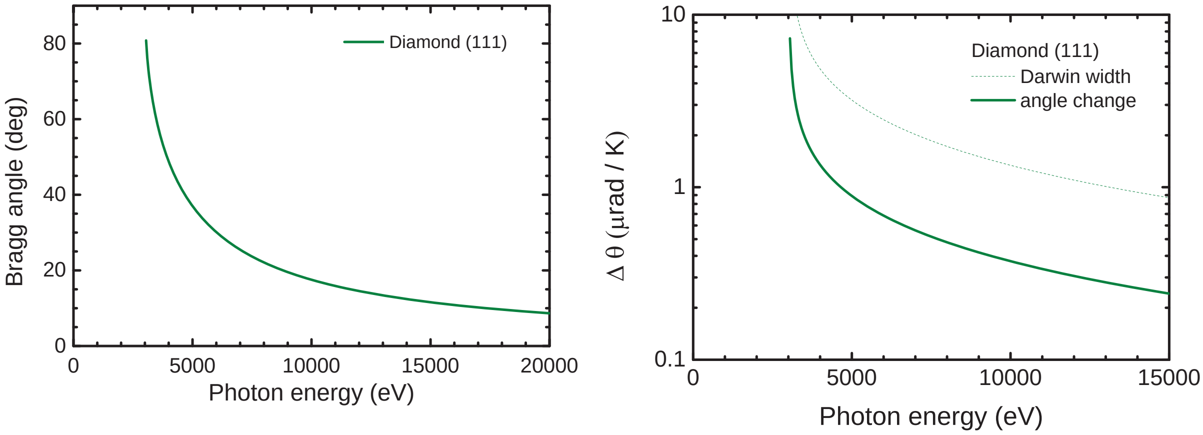

Figure 33: Bragg angle at the diamond (111) reflection (left) and variation of Bragg angle due to thermal expansion (right) according to eqn (15). For comparison, the Darwin width of the reflection is shown as thin line.

The impact of the angular detuning of the LOM on the beam position at the experiment can be reduced, by placing the experiment as close as possible to the LOM.

12 Control system

EPICS is used as control system for the beam transport system. The implementation may consist of central IOCs and distributed hardware components connected by ethernet or field busses.

As the beamlines at SwissFEL extend over a length of 100 m, a central IOC hosting motor controllers with the power supplies attached would require very long motor cables with large cross sections. To avoid this, remotely placed motor controllers with short connecting cables should be utilized whenever possible.

IOCs should be utilized where many actuators and sensors are concentrated at one location, e.g. at the double crystal monochromator chamber.

The control system should be realized in a way that it automatically recovers from power loss into a safe state without manual interaction.

The control system should allow to move an arbitrary number of motors simultaneously.

Mirror setting, especially switching the offset mirrors setting of the monochromator energy will be available for user control.

When scanning the photon energy, the crystal have to stay parallel for a significant overlap of Darwin width. The control system must be able to stabilize the parallelity of the two crystals to a twentieth of the respective Darwin width. This requirement may even tightened when high harmonic rejection requires a detuning of the two crystals. Any angular jitter results in a corresponding intensity fluctuation.

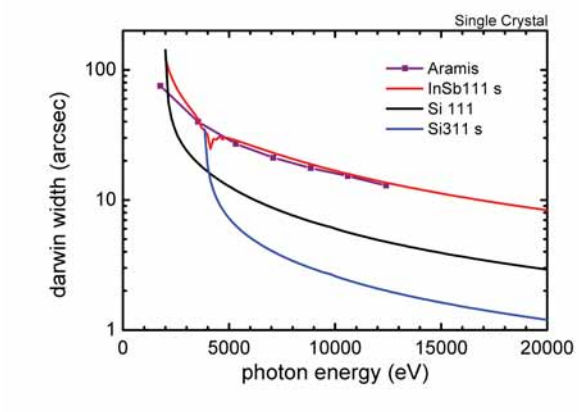

Figure 34: Darwin width of the Bragg reflection at a single crystal. For comparison, the width of the Aramis FEL-beam is depicted too.

13 Appendix

Photon energy to wavelength		$\hbar c = 1239.84$ eV nm
Lattice constant	Si	$d = 0.54310$ nm
	diamond	$d = 0.35668$ nm
	InSb	$d = 0.6479$ nm
Linear thermal expansion coeff.	Si	$\alpha_T = 2.6 \cdot 10^{-6}$
	diamond	$\alpha_T = 1.18 \cdot 10^{-6}$

Table 5: Physical constants and parameters

References

[1] Romain Ganter. SwissFEL conceptual design report. Technical Report 10-04, Paul Scherrer Institut, 5232 Villigen PSI, Switzerland, 2010.

[2] Romain Ganter. SwissFEL conceptual design report v19. Technical Report 10-04, Paul Scherrer Institut, 5232 Villigen PSI, Switzerland, 2011.

[3] P. Kirkpatrick and A.V. Baez. Formation of Optical Images by X-rays. *J. Opt. Soc. Am.*, 38:766, 1948.

[4] A. Aquila, 2013. private communication.

[5] S. P. Hau-Riege, R. A. London, R. M. Bionta, M. A. McKernan, S. L. Baker, J. Krzywinski, R. Sobierajski, R. Nietubyc, J. B. Pelka, M. Jurek, L. Juha, J. Chalupsky, J. Cihelka, V. Hajkova, A. Velyhan, J. Krasa, J. Kuba, K. Tiedtke, S. Toleikis, Th. Tschentscher, H. Wabnitz, M. Bergh, C. Caleman, U. Zastrau, and N. Stojanovic. Damage threshold of inorganic solids under free–electron–laser irradiation at 32.5 nm wavelength. *Applied Physics Letters*, 90:173128, 2007.

[6] S. P. Hau-Riege, R. A. London, A. Graf, S. L. Baker, R. Soufli, R. Sobierajski, T. Burian, J. Chalupsky, L. Juha, J. Gaudin, J. Krzywinski, S. Moeller, M. Messerschmidt, J. Bozek, and C. Bostedt. Interaction of short x-ray pulses with low-z x-ray optics materials at the LCLS free-electron laser. *optics express*, 18:23934, 2010.

[7] F. Siewert et al. Ultra-precise characterization of LCLS hard X- ray focusing mirrors by high resolution slope measuring deflectometry. *Optics Express*, 20:4525, 2012.

[8] M. Störmer et al. . Mono- and multilayer mirrors for current and next generation light sources. *SPIE*, 7077:707705, 2008.

[9] R. Soufli et al. . Development, characterization and experimental performance of x-ray optics for the LCLS free-electron laser. In *Proceedings of SPIE*, volume 7077, page 707716, 2008.

[10] R. Soufli et al. . Morphology, microstructure, stress and damage properties of thin film coatings for the LCLS x-ray mirrors. In *Proceedings of SPIE*, volume 7361, page 7361OU, 2009.

[11] D. L. Windt. IMD–Software for modeling the optical properties of multilayerfilms. *Comp. in Phys.*, 12(4):360–370, 1998.

[12] U. Flechsig, R. Abela, R. Betemps, H. Blumer, K. Frank, A. Jaggi, A. A. MacDowell, H. A. Padmore, V. Schönherr, J. Ulrich, H. Walther, S. Zelenika, and C. Zumbach. The SLS optics beamline. In Jae-Young Choi and Seungyu Rah, editors,

Synchrotron Radiation Instrumentation: 9th Int. Conf., volume 879 of *AIP Conference Proceedings*, page 890, Mellville, New York, 2007. AIP.

[13] A. Meents et al. PETRA user meeting, 2011.

[14] B. Lengeler, Ch. Schroer, J. Tummler, B. Benner, M. Richwin, A. Snigirev, I. Snigireva, and M. Drakopoulos. Imaging by parabolic refractive lenses in the hard x–ray range. *Journal of Synchrotron Radiation*, 6:1153–1167, 1999.

[15] A. Snigirev, I. Snigireva, G. Vaughan, J. Wright, M. Rossat, A. Bytchkov and C. Curfs. High energy x-ray transfocator based on al parabolic refractive lenses for focusing and collimation. *J. of Physics, Conf. Series*, 186:012073, 2009.

[16] H. Mimura, S. Handa, T. Kimura, H. Yumoto, D. Yamakawa, H. Yokoyama, S. Matsuyama, K. Inagaki, K. Yamamura, Y. Sano, K. Tamasaku, Y. Nishino, M. Yabashi, T. Ishikawa, and K. Yamauchi. Breaking the 10 nm barrier in hard x–ray focusing. *Nature Physics*, 6:122–125, 2010.

[17] W. Liu, G. E. Ice, L. Assoufid, Ch. Liu, B. Shi, P. Zachack, J. Tischler, J. Qian, R. Khachartryan, and D. Shu. Hard x–ray nano–focusing with montel mirror optics. *Nuclear Instruments and Methods in Physics Research A*, 2010.

[18] S. Reiche. GENESIS 1.3: a fully 3d time-dependent FEL simulation code. *Nuclear Instruments and Methods in Physics Research Section A: Accelerators, Spectrometers, Detectors and Associated Equipment*, 429(1-3):243 – 248, 1999.

[19] J. Bahrdt. Wavefront tracking within the stationary phase approximation. *Phys. Rev. ST Accel. Beams*, 10(6):060701, Jun 2007.

[20] F. Schäfers. The BESSY Raytrace Program RAY. In T. Krist A. Erko, M. Idir, editor, *Modern Developments in X-Ray and Neutron Optic*, volume 137 of *Springer Series in Optical Sciences*, pages 9–112. Springer, Berlin, 2008.

[21] F. Schaefers, M. Mertin and M. Gorgoi. KMC-1: A high resolution and high flux soft x-ray beamline at BESSY. *Rev. Sci. Instrum.*, 78:123102, 2007.

[22] J. Horbach, U. Hahn, and M. Degenhardt. Large monochromator systems at petra iii. *Nucl. Instrum. and Meth.*, 649:136–138, 2011.

[23] O.H. Seeck et al. The high-resolution diffraction beamline P08 at PETRA III. *J. Synchrotron Rad.*, 19:30–38, 2012.

[24] J. Als-Nielsen, A. K. Freund, G. Grubel, J. Linderholm, M. Nielsen, M. Sanchez del Rio, and J. P. F. Sellshop. Multiple station beamline at the undulator x–ray source. *Nuclear Instruments and Methods in Physics Research Section B:Beam Interactions with Materials and Atoms*, 94:306 – 318, 1994.

[25] G. Grubel, D. Abernathy, G. Vignaud, M. Sanchez del Rio, and A. Freund. A diamond double–crystal transmission monochromator for the TROIKA II station at ESRF. *Rev. Sci. Instrum.*, 67:3349, 1996.

Photon Beam Diagnostics

Pavle Juranić, Luc Patthey, Rasmus Ischebeck, Christoph Hauri, Christian David, Peter Peier, Milan Radovic, Rafael Abela

Contents

1. Photon Beam Diagnostics

1.1. Introduction

Photon diagnostics are imporant tools for both experimenters and machine operators, delivering shot-by-shot information about the quality and quantity of light being produced by SwissFEL. The table below shows the properties needed to be measured by the photon diagnostics at SwissFEL to ensure the proper functioning of the machine, as requested by the operators and users. Some of the devices that will be used to meet these criteria are also in table.

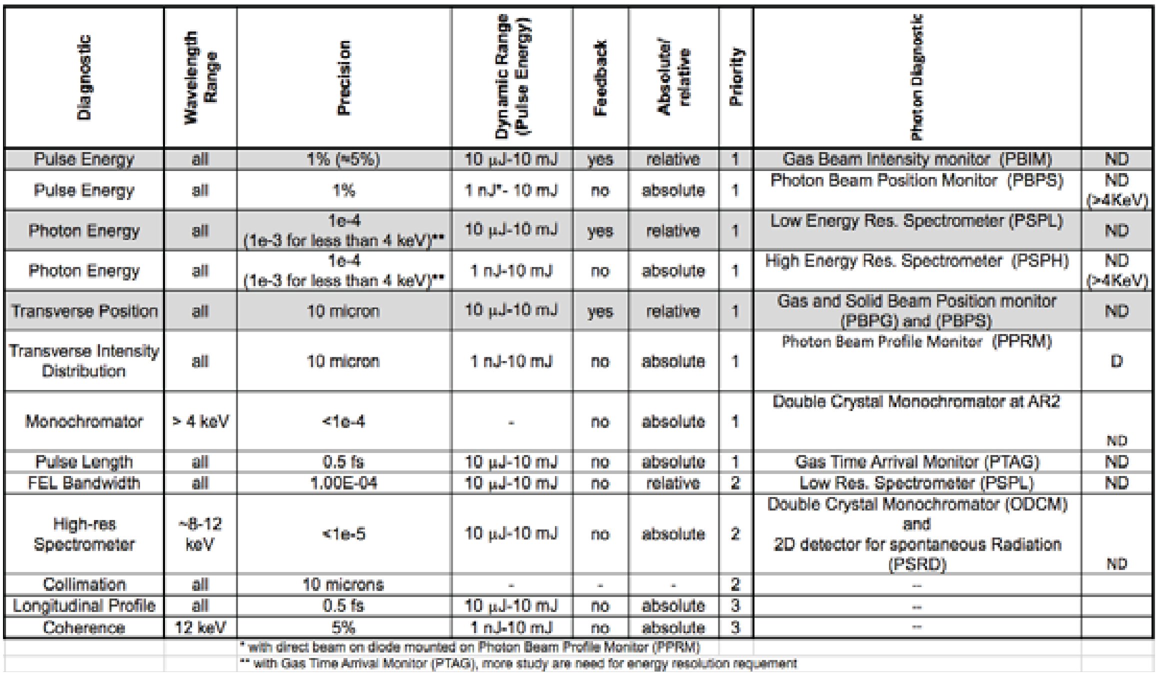

Diagnostic	Wavelength Range	Precision	Dynamic Range (Pulse Energy)	Feedback	Absolute/ relative	Priority	Photon Diagnostic	
Pulse Energy	all	1% (≈5%)	10 µJ-10 mJ	yes	relative	1	Gas Beam Intensity monitor (PBIM)	ND
Pulse Energy	all	1%	1 nJ*- 10 mJ	no	absolute	1	Photon Beam Position Monitor (PBPS)	ND (>4KeV)
Photon Energy	all	1e-4 (1e-3 for less than 4 keV)**	10 µJ-10 mJ	yes	relative	1	Low Energy Res. Spectrometer (PSPL)	ND
Photon Energy	all	1e-4 (1e-3 for less than 4 keV)**	1 nJ-10 mJ	no	absolute	1	High Energy Res. Spectrometer (PSPH)	ND (>4KeV)
Transverse Position	all	10 micron	10 µJ-10 mJ	yes	relative	1	Gas and Solid Beam Position monitor (PBPG) and (PBPS)	ND
Transverse Intensity Distribution	all	10 micron	1 nJ-10 mJ	no	absolute	1	Photon Beam Profile Monitor (PPRM)	D
Monochromator	> 4 keV	<1e-4	-	no	absolute	1	Double Crystal Monochromator at AR2	ND
Pulse Length	all	0.5 fs	10 µJ-10 mJ	no	absolute	1	Gas Time Arrival Monitor (PTAG)	ND
FEL Bandwidth	all	1.00E-04	10 µJ-10 mJ	no	relative	2	Low Res. Spectrometer (PSPL)	ND
High-res Spectrometer	~8-12 keV	<1e-5	10 µJ-10 mJ	no	absolute	2	Double Crystal Monochromator (ODCM) and 2D detector for spontaneous Radiation (PSRD)	ND
Collimation	all	10 microns	-	-	-	2	--	
Longitudinal Profile	all	0.5 fs	10 µJ-10 mJ	no	absolute	3	--	
Coherence	12 keV	5%	1 nJ-10 mJ	no	absolute	3	--	

* with direct beam on diode mounted on Photon Beam Profile Monitor (PPRM)

** with Gas Time Arrival Monitor (PTAG), more study are need for energy resolution requement

Table 1.1.1: The table of requirements for photon diagnostics for the SwissFEL. The symbols ND and D in the last column stand for 'non-destructive' and 'destructive' respectively.

Most of the photon diagnostics devices need to be non-destructive and some need to deliver the information they measure to a machine feedback system. Because of these requirements, the photon diagnostic concepts have focused on gas and low-Z materials and non-destructive methods for answers. However, some destructive measurements are envisioned as well, mainly used for beam alignment, commissioning, and pre-experimental setup.

1.2. Gas-based detectors

1.2.1. Concept

The Photon Beam Intensity Monitor (PBIM) and the Photon Beam Position Gas Monitor (PBPG) are gas-based, non-destructive absolute and relative photon beam flux and photon beam position measurement devices. The working principle of the PBIM is best summarized by the equation below:

$$\Phi = \frac{N}{\sigma z \eta n a} \qquad (1)$$

Where Φ is the number of photons, *N* is the detected number of ions, corrected by the expected average charge of the ions, σ is the cross section of the atom, *z* the detector acceptance length, η is the detection efficiency, *n* the atomic gas density, and *a* is the detector amplification factor. Most of these values, like the detector acceptance length, can be set by the design of the device or simply measured--pressure and temperature measurements give us the atomic gas density, and the amplification factors of most metals are 1. For the other values, like the cross section and the average charge we need to have wavelength-specific lookup tables, most of which exist in atomic physics literature. We can ensure a reliable measurement of the current on a metal plate from the ions photoionized by the FEL beam by controlling the gas pressure fluctuations to better than 1%. The ions would be deflected onto the plate by applying a strong electric field in the gas-light interaction region. For relative measurements, we can amplify this signal with a pre-amp outside of the chamber for the feedback system. The slower absolute measurements would be done directly by integrating the charge collected on the plate over a several tens of seconds.

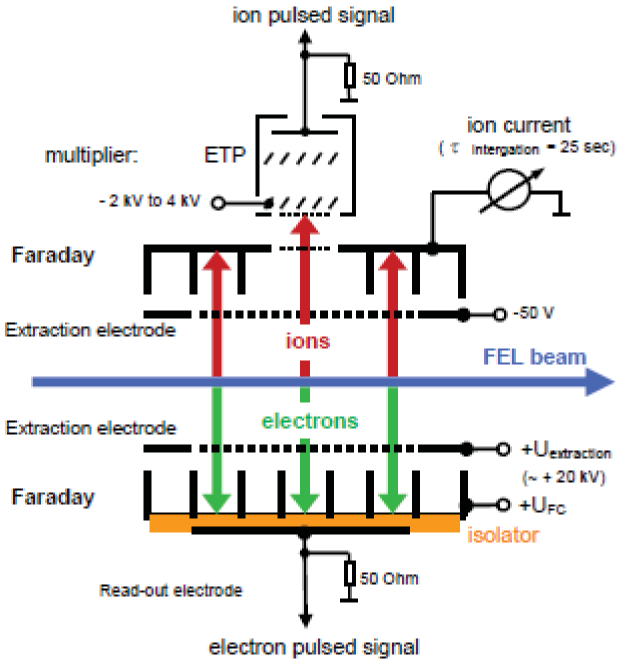

Figure 1.2.1.1: A schematic overview of the DESY XGMD from [1]. The PBIM will be similar.

The PBPG uses gas to measure the vertical and horizontal position of the photon beam. It does this via two split electrodes that the ions impact, placed in the horizontal or vertical direction. By reading out which electrode sees more signal, one can determine the horizontal or vertical position of the beam. This device only needs relative measurements, so the gas pressure does not need to be as finely controlled as for the PBIM. To calibrate the device, the horizontal and vertical measurement components of the PBIM need to be mounted on tables that can move about +/- 1mm in the horizontal or vertical direction, respectively.

Furthermore, the PBPG multipliers will also be used to deliver the faster, relative shot-to-shot intensity information. The stability of the in-vacuum multipliers developed by DESY is reportedly sufficiently good to meet the 1% accuracy criteria.

1.2.2. Vacuum Chamber and Pumps

The vacuum chambers making up the PBIM and the PBPG will most likely be a combination of finished hardware from the Photon Diagnostics group at DESY and chambers designed by the vacuum group at PSI. The design from DESY for the PBIM and PBPG will be four chambers: two for intensity measurements, one for the vertical position measurements, and one for the horizontal position measurements. The four chambers will be linked together by large bellows allowing a small range of motion for each chamber, so that the x and y positions PBPGs can be calibrated. The total size of these devices is expected to be about 2.7 m in length, and all the chambers will have a DN 200 mm diameter. The gas pressure in the chambers is expected to be between 10^{-4} and 10^{-6} mbar, with the pressure in the PBIMs being more finely controlled with a spinning rotor gauge (RS 232 from MKS Vacuum). The spinning rotor gauge will be combined with a 300 l/s Pfeiffer pump to keep the pressure to 1% stability. The setup is shown in figure 2 below.

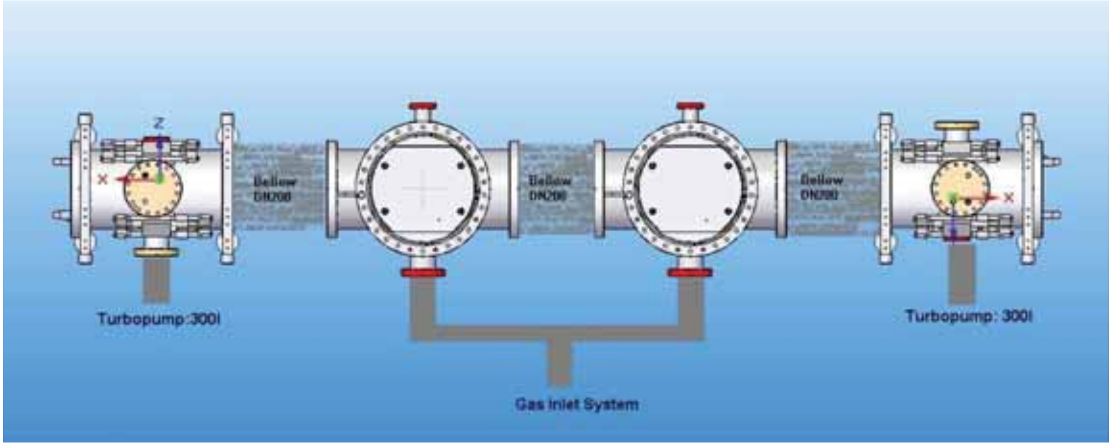

Figure 1.2.2.1: A schematic overview of the setup of the PBPG and PBIM, courtesy of Kai Tiedtke.

Differential pumping stages (DPS) will be on either side of these chambers to keep the pressure in the rest of the machine within acceptable parameters (10^{-8} mbar or less). The total space for these chambers is expected to be about 1 m per chamber, for a total length of the PBIM, PBPG, and the DPSs of about 4.7 m. The chambers will provide a pressure-sensitive interlock to the electronics systems. The type of pumps and the exact design of these chambers will e determined when the PBIM and the PBPG designs are finalized.

Furthermore, the gases used for the measurement would need to be pumped out of the tunnel safely. Considering that the gases used will be mostly Xe, Ar, Kr, and Ne, recycling them in some way may be an option.

1.2.3. Interlock System

The interlock system for the PBIM and the PBPG will depend on the pressure sensors, designed to shut down the power supplies and sensitive electronics if the gas pressure in the device becomes too high or if there is a malfunction in the pressure sensors' reading. Furthermore, the whole setup will be interlocked with the SwissFEL general emergency interlock, and will shut down the sensitive equipment in case of any problems.

1.2.4. Linear Motion and Supports

The PBPG has two components, each needing to be moved in one of the two directions perpendicular to the direction of the FEL photon beam. To that end, one of them requires a table with the linear motion in the horizontal direction of about +/- 1 mm with a precision of 10 μm, and the other requires the same in the vertical direction. Both of these constructs should be controllable via network. This is necessary to calibrate the position measurements while the FEL is in operation.

The PBIM needs to be mounted on a regular, non-movable support that will place it along the photon beam. A sturdy support is all that is required for it.

1.2.5. Detector and Monitor Hardware

The PBIM and PBPG will require 10-14 kV power supplies to create the electric field necessary for the accurate and clean detection of the ions created during the photoionization process. The high potential needed is a result of the large kinetic energies that the photoelectrons created during the ionization process would have. To be completely sure that only photoions impact the metal ion collector plate (in the PBIM) or the multiplier (in the PBPG), a large electric field is needed to “suck away” the electrons to the electron collector plate. The DESY XGMD plans to use ISEG power supplies in a MMC module for this purpose, offering a stability of 10^{-5} dV, 10 mV ripples, and a current of 2 mA.

The PBPG will have a large electron multipliers to amplify the signal from the photoionization to give an accurate position signal on the split anodes that are on the side of the multipliers opposite the interaction region (see figure 2).

Additionally, there is the possibility of including a small multiplier in the PBIM as a rough time-of-flight measurement device. This can be used to look at the signal generated by the light-gas interaction and derive the average charge of the particles impacting the ion collector plate. Though the average charge will be something that will be listed in the lookup tables, such a device is useful as a backup check, and also if we wish to operate the PBIM under new conditions. A 3-5 kV power supply, a pre-amplifier, and a patch-panel input to an oscilloscope would be necessary for this device to work properly.

Lastly, a calibrated multi-meter is necessary for the slow absolute measurements. The DESY XGMD plans to use a calibrated Keithley multimeter for this purpose. The Keithley’s performance, like its droop, would need to be checked to ensure the best results.

1.2.6. Data Acquisition Hardware and Firmware

The PBIM will acquire data in two modes: a slow, absolute measurement, and a fast relative measurement. The slow absolute measurement will be done with a calibrated current meter over the course of several tens of seconds. This measurement will directly measure and integrate the current generated by impacting ions on the ion collector plate. The total charge after 25-40 seconds of measurement will yield the total number of ions generated in this time period. The total integrated flux can be calculated from the total ion yield. This “brute force” method, while cumbersome, is reliable and simple. The 10% accuracy for this mode will mostly come from literature data. The multimeter used for this mode of measurement would need to be integrated into the SwissFEL EPICS system.

The fast, relative mode of measurement will use a pre-amplifier and a current integrator circuit to record the total amount of charge deposited on the ion collector plate per pulse. The minimum amount of photoions that need to be detected to meet the 1% relative accuracy criteria is 10,000, using the standard error of the mean. That means that, without multipliers, the pre-amplifier and integrator need to be able to reliably detect a total charge of several fC per pulse, and be able to detect 1% variances in this signal from shot to shot. However, since the shot-to-shot measurements will be taken from the multipliers in the PBIM, the total charge coming to the pre-amplifier should be between 100 pC and several nC. The integration time for this measurement can be made short (10-100 μs) at a frequency of 100 Hz. We can also have a measurement between the pulses (about 5 ms after the trigger) to get an accurate zero reading for a more precise measurement. This would increase the measurement frequency to 200 Hz. Lastly, the front end electronics would need to have a sufficiently large dynamic range to meet the demand of charge measurements that can vary up to four orders of magnitude.

To get the absolute per-pulse measurement of intensity, the long absolute measurement would be distributed according to:

$$I_0 = \sum_j I_0 x_j \tag{2}$$

Where I_0 is the absolute intensity and $I_0 x_j$ is the relative pulse intensity measurement per pulse *j*. The signal from the circuit will go to a FPGA board in a rack, connected by an appropriately fast, safe, and secure connection to the front-end electronics, and then interfaced with the SwissFEL controls and feedback systems.

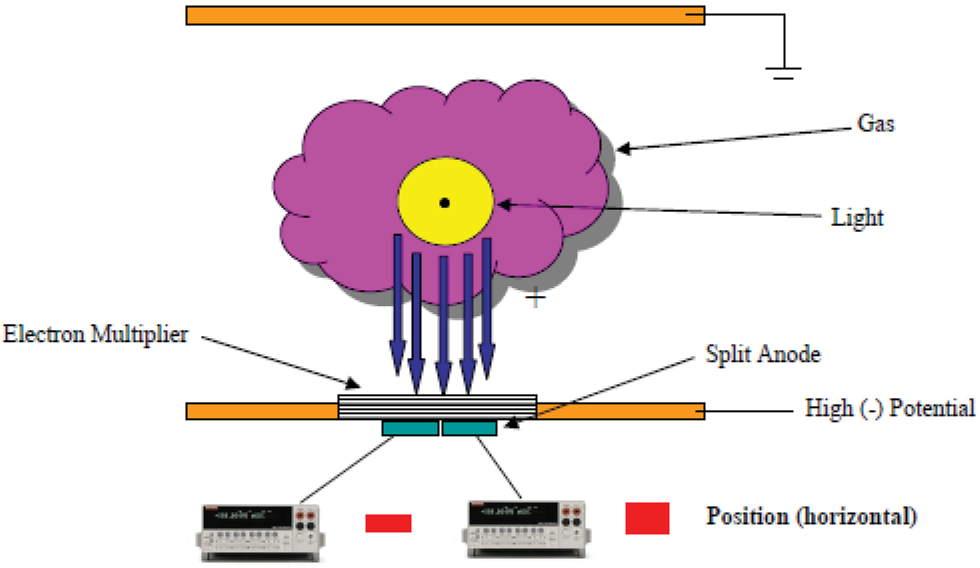

Figure 1.2.6.1: A schematic drawing of the PBPG monitor for the horizontal position of the FEL beam.

Two relative pulse-to-pulse measurements will also be needed for each direction of the PBPG, with two electrode readouts for the x and y positions of the FEL beam. The signal there would come from a combination of an in-vacuum electron multiplier and a split anode, schematically shown in figure 3. These anodes would be delivering the shot-to-shot relative intensity measurements as well as the position measurements, as mentioned earlier.

The development of these systems is expected to take several months to a half a year, if fully supported in manpower, and is expected to be a part of the general solution for the SwissFEL front end electronics system. Further work will need to be done to double-check if the delivered hardware matches the specifications needed for the successful implementation of the measurement devices in SwissFEL, as well as system engineering and installation.

1.2.7. Controls System

The control system for the PBIM and the PBPG should provide expert panels for the control of the power supplies and electronics for the two devices, as well as clearly labeled readouts for pressure, temperature, device status, signal output, etc. There should also be a 'regular' display for users. An example of an expert panel from FLASH is shown in figure 4 below.

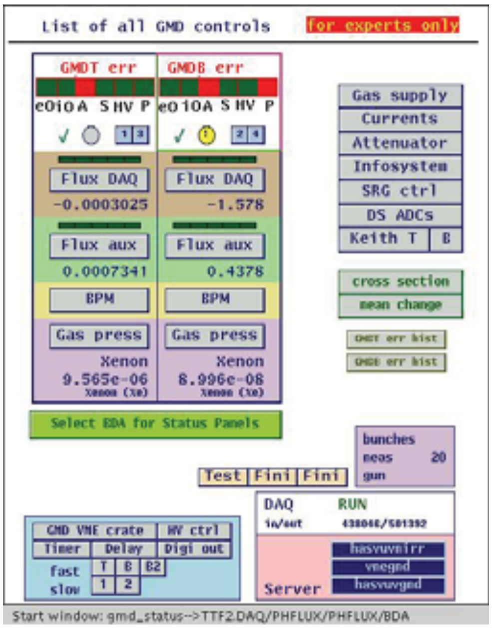

Figure 1.2.7.1: The expert panel for the GMD at the FLASH FEL.

The two devices also need to be tied to the timing and event system to trigger their measurements. The measurements themselves have to be recorded and matched with the pulse identification number of the FEL, and later on run through the formulas and lookup tables. The final data for the absolute and relative measurements should be saved in an archiver.

The faster, relative measurement data from the PBIM should also be feed to the global feedback system for the machine, so that the operators can use it to create routines to improve FEL performance. A schematic diagram for the controls setup for the PBIM can be seen in figure 5. The handling of most of these tasks will be done through an EPICS IOC system installed in a VME crate.

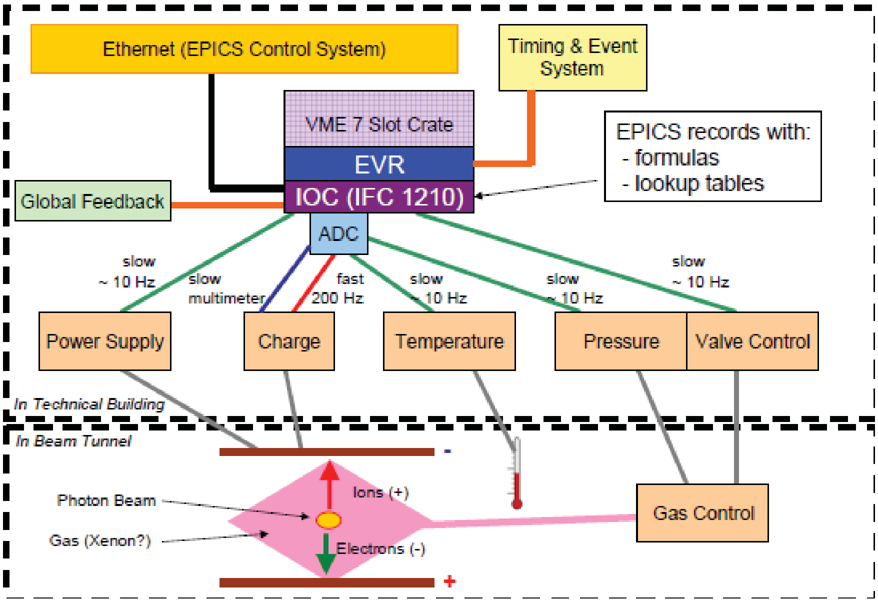

Figure 1.2.7.2: A schematic diagram for the PBIM controls system.

1.2.8. Analysis Software and Data Storage

The PBIM will need a list of pre-measured and calibrated values for the gas cross-sections and average charges of the gases that it will use to measure the photon flux. Xe will be used the most because of its larger cross section at higher photon energies. These pre-calibrated values will go into formula (1) to evaluate the absolute number of photons detected in a period of time. This formula will be evaluated by a higher-level EPICS program that will also include other information needed for the evaluation, like the ambient temperature of the gas (to derive the gas particle density), the detector acceptance length, etc.

The fast, relative measurements done by the PBIM will be immediately sent to the feedback mechanism. However, the later per-pulse distribution of absolute intensity will also be done in a higher-level EPICS program.

The PBPG position signals will be processed by the front end electronics or the IOC card and immediately sent to the feedback system. However, the position data for each shot should be saved along with the absolute and relative intensity measurements by the higher-level EPICS program.

The data storage of the ID, absolute intensity, and position of the pulse should be stored in a database for future use by operators and users. It is recommended that the data for every pulse be stored for a period of several months, after which they can be smoothed and compressed to provide an average of 100 pulses for one or more years. The data should then be smoothed even further and sent to some kind of tape storage for future use.

This storage system of pulse information should be searchable by experiment and date, so that both users and operators can retrieve the data they need for the period they wish to see. Furthermore, the values from these measurements should be able to be easily integrated with the metadata archive used for experiments. This will ensure that SwissFEL users can easily get all of the information they need for the data analysis of their experiments.

The development o the software will require occasional and personal contact with the DESY group to benefit from their expertise and experience. To this end, occasional trips of key personnel to DESY (or from DESY to PSI) will be needed to create the software needed for analysis.

1.3. Backscattering monitors and diode-based detectors

1.3.1. Concept

X-ray scattering from thin films and materials has been extensively studied in the past, both theoretically and in experiment, and is fairly well understood. An excellent theoretical treatment of the various scattering effects is found in [5]. The effect that interests this work the most, and is by far the largest factor in the backscattering detectors we wish to build, is the incoherent Compton scattering of the photons from the electrons in the thin diamond films. The general equation for this effect is given in [2] as

$$\sigma_{inc} = \int_{\theta 1}^{\theta 2} \partial\sigma_{kn} S(x,z) \tag{1}$$

Where σ_{inc} is the total incoherent cross section per atom, $S(x,z)$ is the incoherent scattering function, $\partial\sigma_{kn}$ is the differential, solid angle Klein-Nishina (free-electron Compton) cross section per electron, and θ_1 and θ_2 are the angles that define the cone the photons we are detecting are backscattering in. The Klein-Nishina cross section is defined by:

$$\partial\sigma_{kn}/\partial\Omega = \frac{r_e}{2}[1+k(1-\cos\theta)]^{-2}[1+\cos^2\theta+\frac{k^2(1+\cos\theta)^2}{1+k(1-\cos\theta)}] \tag{2}$$

Where $r_e = 2.8179380 \times 10^{-15}$ m, the classic electron radius, and k is the photon energy in units of electron rest-mass energy, eV/511003.4

The function $S(x,z)$ is defined in [2] by a series of values for a value of $x = \frac{\sin(\theta/2)}{\lambda}$, where λ is the wavelength of the photon being scattered in Angstroms. The table in [5] lists values as a function of x and the element—in this case, carbon.

Once the wavelength and the element are chosen, and the incoherent cross section per atom has been calculated, we use a modified formula for transmission to find out how many photons are back-scattered in our solid cone. The general expression for transmission T is

$$T = e^{-\rho l \sigma} \tag{3}$$

Where ρ is the atomic density of the material (diamond), *l* is the length of the film, and $\sigma = \sigma_{inc}$, the total incoherent cross section per atom. The ratio of photons that are reflected would be $R=1-T$, which would be the photons that would come within the cone the diodes' surface is in. If we use the geometry used by the setup at SACLA, as shown in figure 1, and described in [3], the diodes would see photons reflected between 2.065 and 2.501 radians.

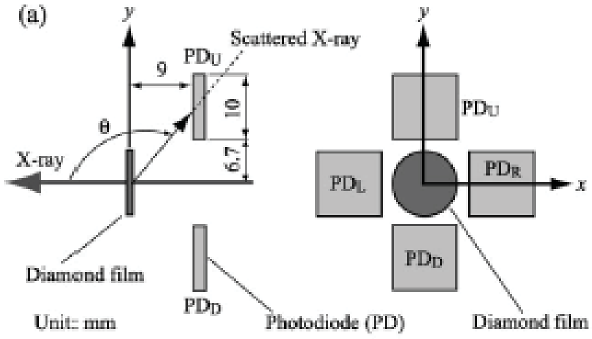

Figure 1.3.1.1: The concept for the backscattering monitor, as shown in [3].

Combining the geometry from fig. 1, eq. 3, and the fact that the atomic density of diamond is 1.73^{-29} m^{-3}, one can arrive at a list of ratios of reflected photons as a part of the whole beam, according to wavelength. This is shown in table 1 for a 15 μm thin diamond film.

Wavelength (Å)	Reflected photon ratio
1	1.29^{-4}
3	9.69^{-5}
5	5.86^{-5}

Table 1.3.1.1: Ratio of reflected photons as a function of wavelength for a 15 μm thin diamond film, using the setup described in [3].

The expected flux from the SwissFEL is several tens of billions photons per pulse, which would mean that several million photons would be back-reflected. Of these, slightly less than half would impact the diodes, which would mean that the each diode would see around 10^5 photons per pulse. This number is sufficient for our goal of 1% accuracy in relative intensity measurements, and 10 μm position accuracy measurements. The only problem with this arrangement is that the diamond thin film becomes progressively more absorptive at higher wavelengths (lower photon energies), and would eventually become damaged or absorb too many photons. This restricts the use of the device to photon energies above about 4 keV, or wavelengths lower than 3.1 Å.

The back-scattering monitor would use the signals on the top and bottom diodes (PD_U and PD_D in fig. 1) to find out the vertical position of the beam, and the right and left diodes (PD_R and PD_L) for the horizontal. The normalized total of all four diodes would give the relative intensity. The equations for the horizontal and vertical intensity change due to the position of the beam are:

$$\Delta I_x = \frac{I_R - I_L}{I_R + I_L} \tag{4}$$

$$\Delta I_y = \frac{I_U - I_D}{I_U + I_D} \tag{5}$$

The total intensity is:

$$I_0 = K(I_L + I_R + I_U + I_D) \tag{6}$$

where K is a constant of proportionality.

Small movements in the x and y direction would be necessary to calibrate the back-scattering monitor and find the constants of proportionality ΔK_x and ΔK_y that would link the motion of the beam Δx (horizontal) and Δy (vertical) to ΔI_x and ΔI_y.

For non-SASE, spontaneous radiation, the amount of photons per pulse is expected to be less than several hundred nJ. This means that a simple diode can be put into the beam to measure the per-pulse intensity directly. Experience from SACLA has shown that the direct photodiode measurement method starts becoming inaccurate when the pulse energy reaches about 460 nJ [4]. Therefore, we should restrict the direct measurements of the intensity to measuring FEL pulses that have less than several 10^8 photons. This diode could be put in the same ladder containing the screens and be inserted for non-SASE beam.

1.3.2. Thin Carbon Films

One of the issues that require special attention in the construction of the backscattering monitor is the thin carbon film used for the backscattering**.** If the film is not uniform, various non-uniform defects begin to appear in the back-reflected photon pattern, giving a false distribution of the photons on the diodes. Such a pattern could be interpreted as the beam being off center while it is actually perfectly aligned, and would generally be a nuisance for measurement.

The scientists at SACLA performed measurement on several diamond films, as well as several other materials, and showed that the most effective choice for a back-scattering reflector would be a nanocrystal diamond film with low surface roughness (< 50 nm) and small grain size (<40 nm). Such diamonds can be produced by chemical vapor deposition (CVD) and can be purchased. One firm that seems to deliver them in Europe is Diamond Materials GmbH, in Germany.

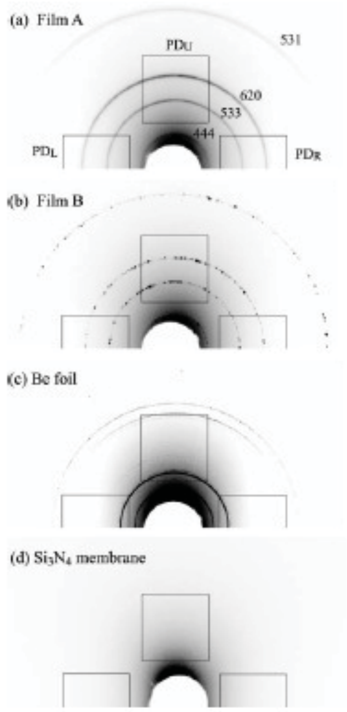

Figure 1.3.2.1: Thin film tests done at SACLA from [3]. Film A is a nanocrystal diamond with grains smaller than 34 nm, and surface roughness of the same order.

The films to be used in the backscattering monitor would need to be purchased and a sample tested to see if it confirms to the expectations. Such tests can be done at Swiss Light Source (SLS).

1.3.3. Vacuum Chambers and Systems

The diodes and the back-scattering film can function in air or in vacuum, but the devices need to be in vacuum because of the FEL beam. However, whether or not vacuum pumps are required on the chambers themselves should be determined by the Vacuum group. Every chamber should, at the very least, have a pressure gauge. There is no need for differential pumping stages or other protection equipment, as no gases are expected to be produced in the chamber.

The vacuum chamber would need to be a four-way CF40 with CF63 cross. The CF63 flanges are required to house the back-scattering monitor, the shielding for the diodes, and an in-vacuum motor. The motor would be connected to a ladder-like holder for the thin films, and their position would be controlled by driving the motor in and out. The CF40 flanges would be used to connect to the photon beam pipe.

Lastly, a simple residual gas analyzer may be an option for the chambers. This would allow for the monitoring of the presence of carbon particles in the chamber, the presence of which would indicate damage to the diamond films.

The general chamber design should be decided at PSI, but ist construction can be outsourced to an external supplier.

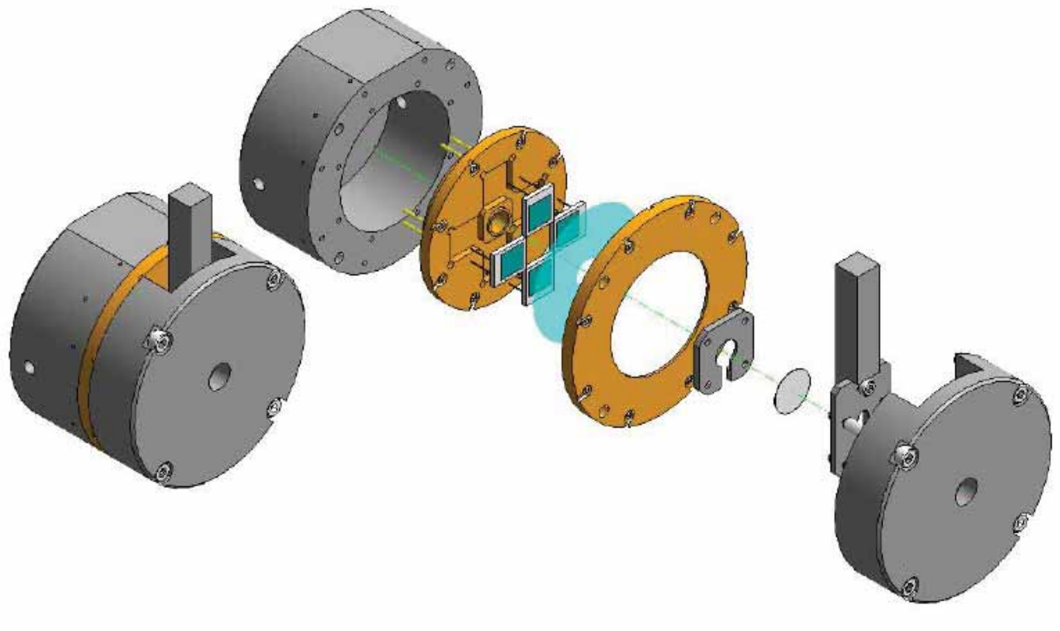

Figure 1.3.3.1: The vacuum chamber housing the back-scattering monitor at SACLA.

1.3.4. Linear Motion and Supports

The back-scattering detector chamber would most likely need to be mounted on a table with motion in the directions perpendicular to the FEL beam. It would require at least a +/- 1 mm range in both the horizontal and vertical direction with an accuracy of 10 μm. These motions would be used for calibration. The motors should be controllable via a network or remote connection.

1.3.5. Detector Monitors and Hardware

The main detectors for the PBPS are Si PIN photodiodes. The ones used at SACLA are the S3590-09 Hamamatsu Photonics Inc model. These photodiodes have a 10 mm x 10 mm sensitive surface, and can detect many photons. A similar photodiode should be used for the backscattering monitors SwissFEL will use as well. The photodiodes should be tested before their implementation in the final design.

1.3.6. Data Acquisition Firmware and Hardware

The photodiodes used to measure the back-reflected or direct photons at SwissFEL need to measure a wide range of pulse intensities, which, in turn, create a range of charge levels per pulse. To accommodate such a range, several different charge/voltage conversion stages will be necessary to deliver an analog signal of the correct strength for the correct pulse intensity. The range of charge created in the photodiodes is in the pC-μC range [4].

The signal needs to be processed with a combination of amplifiers and an analog-to-digital converter which can be placed in the front end or on an IOC card. A full description of the data acquisition hardware used at SACLA is presented in [4], and should be used as a guide to develop the electronics hardware needed for these diodes at SwissFEL. An example of the hardware used at SACLA for signal processing is shown in figures 4 and 5.

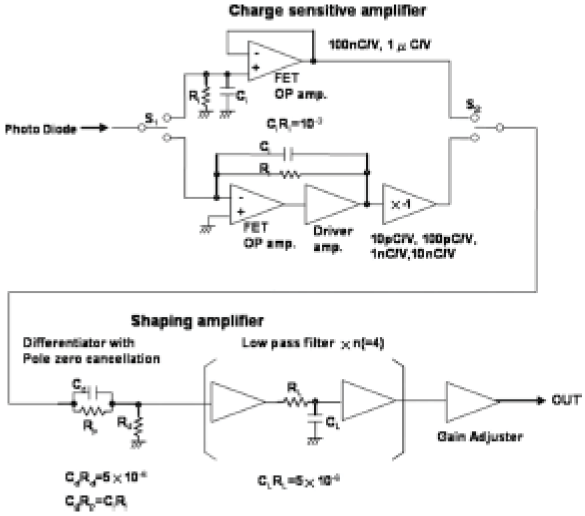

Figure 1.3.6.1: The charge sensitive amplifier circuit from [4], used at SACLA for their diodes.

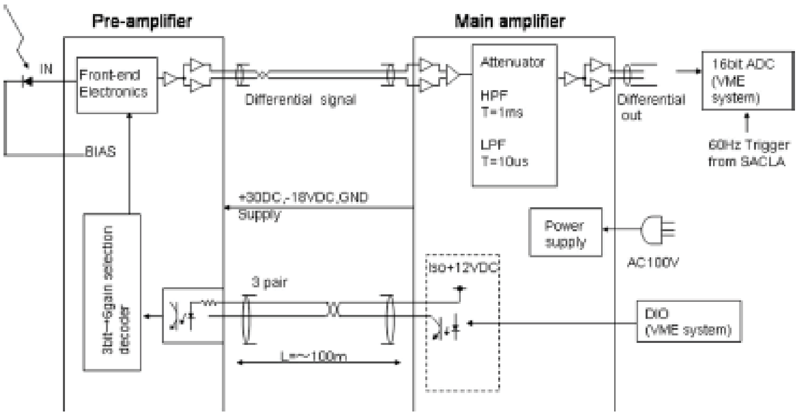

Figure 1.3.6.2: Signal processing from [4], used at SACLA for their diode signals.

The diodes' reverse bias current could further be monitored by a direct DC coupling to see if they have degraded over time. This requirement would be decided after a testing of the diodes.

We would require a system similar to the one presented in [4] for every diode. Depending on the chamber, that would mean either four or five such setups per chamber or device.

The VME rack for at least one of the PBPS monitors can be placed in the tunnel to reduce the amount of distance between the diodes and the ADC on the IOC card. The crate with the VMI would not cause significant heat load or be under danger from radiation in the area behind the beam dump.

1.3.7. Controls System

There should be an expert panel for the control of each of the devices SwissFEL will have, labeled so that the operator knows where the device is along the photon beam path. There should also be a regular panel for beamline users showing general information of interest to the experiment.

The devices need to be triggered by the timing and event system, and their measurements need to be tied to the FEL pulse number generated by the event system. Those same measurements then need to be run through the algorithms and normalization routines to deliver the beam position and relative intensity measurement from the back-scattering detector, or just the intensity measurement from the direct diode detector.

The final data for these measurements should be saved in an archiver. The handling of these signals will be done on an IOC controls card with an EPICS interface.

1.3.8. Analysis Software and Data Storage

The PBPS will measure the relative intensity of the photon beam and the absolute position of the photon beam according to the formulas and concepts laid out in 4.1. These formulas will be evaluated in a higher-level EPICS program that will also have access to other information necessary for the evaluation of the data, like the pre-calibrated proportionality constants mentioned in 4.1.

The data storage of the ID, intensity, and position of every photon pulse should be stored in a database for future use by operators and users. It is recommended that the data for every pulse be stored for a period of several months, after which they can be smoothed and compressed to provide an average of 100 pulses for one or more years. The data should then be smoothed even further and sent to some kind of tape storage for future use.

This storage system of pulse information should be searchable by experiment, detector position, and date, so that both users and operators can retrieve the data they need for the period they wish to see at the location the data was taken. Furthermore, the values from these measurements should be able to be easily integrated in the metadata archive used for experiments. This will ensure that SwissFEL users can easily get all of the information they need for the data analysis of their experiments.

1.4. Photon beam profile monitors

1.4.1. Concept

Scintillating screens coupled with optics and CCD cameras have been used for years to characterize the beam profiles of light over a large range of spectra (from UV to hard X-ray) and is a mature, dependable methodology [5]. Despite its age, however, new advances are still being made and improvements in the methods and measurements come forth yearly, mainly in the design of scintillator materials, but also in the cameras that become accessible.

The basic principle behind scintillation is the emission of visible or easily detectable wavelengths of light as a by-product from de-excitation of electrons that were kicked into a higher orbital state by an ionizing or excitation event (like photon absorption or electron beam interaction). The available transitions vary from material to material, and a list of the available wavelengths and materials is presented in figure 2, along with some of the material physical properties.

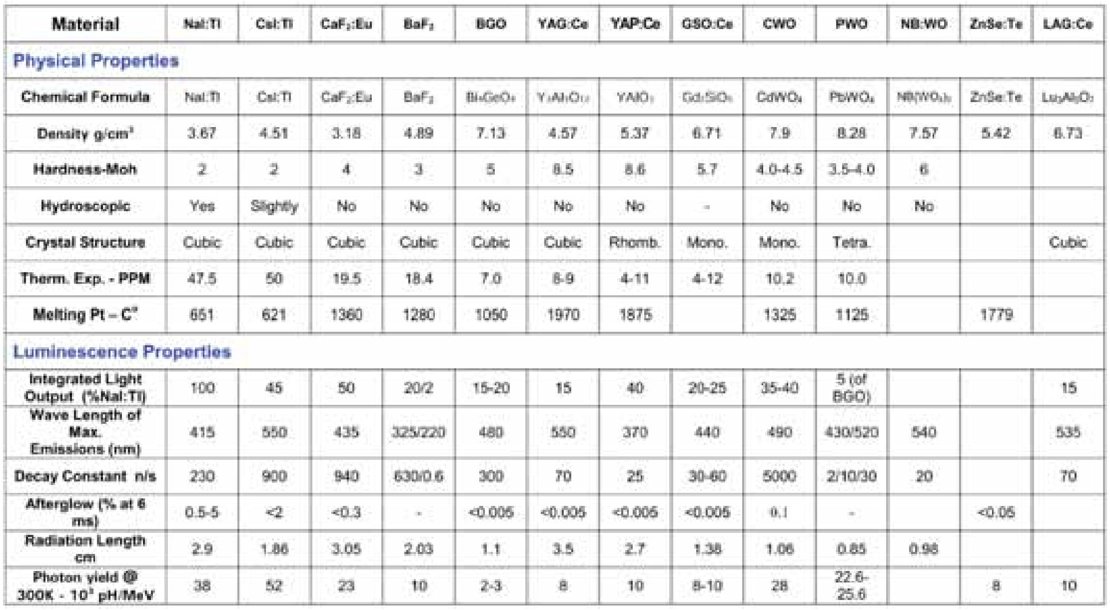

Material	NaI:Tl	CsI:Tl	CaF_2:Eu	BaF_2	BGO	YAG:Ce	YAP:Ce	GSO:Ce	CWO	PWO	NB:WO	ZnSe:Te	LAG:Ce
Physical Properties													
Chemical Formula	NaI:Tl	CsI:Tl	CaF_2:Eu	BaF_2	Bi_4GeO_4	$Y_3Al_5O_{12}$	$YAlO_3$	Gd_2SiO_5	$CdWO_4$	$PbWO_4$	$NB(WO_4)_2$	ZnSe:Te	$Lu_3Al_5O_{12}$
Density g/cm³	3.67	4.51	3.18	4.89	7.13	4.57	5.37	6.71	7.9	8.28	7.57	5.42	6.73
Hardness-Moh	2	2	4	3	5	8.5	8.6	5.7	4.0-4.5	3.5-4.0	6		
Hydroscopic	Yes	Slightly	No	No	No	No	No	-	No	No	No		
Crystal Structure	Cubic	Cubic	Cubic	Cubic	Cubic	Cubic	Rhomb.	Mono.	Mono.	Tetra.			Cubic
Therm. Exp. - PPM	47.5	50	19.5	18.4	7.0	8-9	4-11	4-12	10.2	10.0			
Melting Pt – C°	651	621	1360	1280	1050	1970	1875		1325	1125		1779	
Luminescence Properties													
Integrated Light Output (%NaI:Tl)	100	45	50	20/2	15-20	15	40	20-25	35-40	5 (of BGO)			15
Wave Length of Max. Emissions (nm)	415	550	435	325/220	480	550	370	440	490	430/520	540		535
Decay Constant n/s	230	900	940	630/0.6	300	70	25	30-60	5000	2/10/30	20		70
Afterglow (% at 6 ms)	0.5-5	<2	<0.3	-	<0.005	<0.005	<0.005	<0.005	0.1	-		<0.05	
Radiation Length cm	2.9	1.86	3.05	2.03	1.1	3.5	2.7	1.38	1.06	0.85	0.98		
Photon yield @ 300K - 10³ pH/MeV	38	52	23	10	2-3	8	10	8-10	28	22.6-25.6		8	10

Table 1.4.1.1: Physical and luminescence properties of some scintillating crystals, courtesy of Martketech International, Inc.

In addition to the inorganic scintillators shown in figure 2, doped diamond crystals have been used as scintillators as well. SACLA, for example, uses both 300 mm thick YAG:Ce scintillator screen and a 30 mm thick boron-doped diamond screen [6]. The advantage of using doped carbon scintillators, despite their lower yield than the YAG:Ce screens, is that they are nearly transparent to hard x-ray radiation, allowing the use of the screen without significantly affecting the FEL beam's intensity.

In addition to the standard scintillator-and-mirror setup, the spontaneous radiation detector would have a multi channel plate (MCP) plate in front of the scintillating screen to yield sufficient signal for detection by the camera. A MCP is a thin disk composed of many small (6-15 μm diameter) tubes coated with a material that emits a large number of electrons when impacted by ionizing radiation or particles. They typically emit between 10,000-100,000 electrons per ionization event. These electrons would then be accelerated onto the scintillating screen, where they would cause emission of visible light. A simple sketch of the proposed setup is shown in figure 3. A similar setup, without the MCPs, would be used for the direct observation of the beam. The MCP would have a high, negative

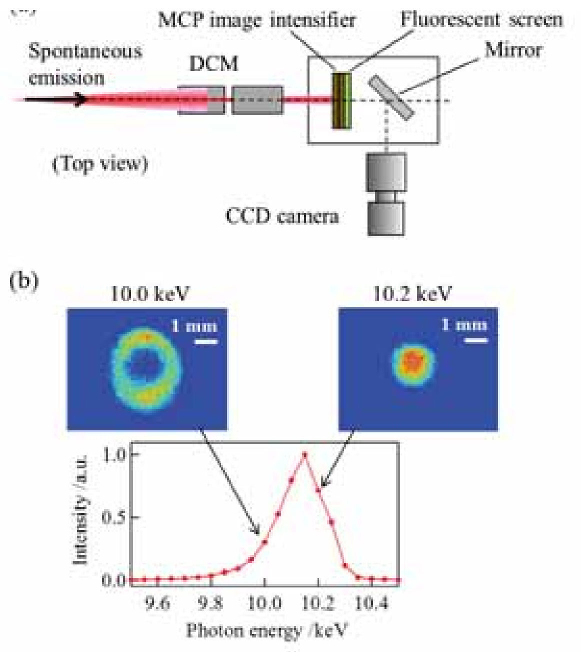

Figure 1.4.1.1: the MCP, screen, mirror, and camera setup, as shown in [6].

1.4.2. Scintillating Screens

The parameters for choosing the best material for FEL application are radiation hardness, light yield (or x-ray to light conversion), and spatial resolution. Thinner crystals tend to give a better spatial resolution, and experience at PSI and elsewhere has shown that YAG:Ce screens of thicknesses between 30 and 100 mm can reach the 10 mm rms resolution while still yielding sufficient signal for detection. A 30 mm boron doped diamond film should be able to deliver these values as well for a full SASE beam [6]. Both YAG:Ce and Diamond are radiation hard and have been used in FELs around the world without showing any significant degree of degradation as long as they are not in focus of the FEL beam. When placed at the focus of FEL beams, they usually displayed significant alterations to their surface roughness or cracking [7]. Therefore, YAG:Ce and doped diamond are the best choices for scintillating screens for SwissFEL. The screen used for the MCP setup could be a phosphor screen, optimized for scintillation from electron impact.

A possible supplier for the doped carbon scintillating screens is Diamond Materials GmbH from Freiburg, Germany, which has a long-standing business relationship with PSI and has delivered similar products to PSI in the past. The YAG:Ce screens can be purchased from a multitude of commercial sources and are commonly available in the required thicknesses and sizes.

To cover the full range of intensities and wavelengths we would see at SwissFEL, three scintillating screens should be installed: a 30 μm YAG:Ce, a 100 μm YAG:Ce, and a 30 μm boron-doped carbon screen. They should be etched with marks with several micrometer spacing for spatial orientation of the image displayed by the camera.

1.4.3. MCPs

One of the main issues when using an MCP is that its channels limit the resolution of the complete device, since the electrons have a small divergence as they exit the MCPs channels. However, with the right choice of MCP, and the use of just one single MCP (as opposed to a stack of them), this problem will be minimized to a resolution of about 10 μm rms as well. Hamamatsu photonics offers MCPs with a fairly small pitch of 6 μm, and even offers a tailored holder for them one can mount on a motorized stage. However, other firms offer similar products, and their procurement should not be difficult. The holder for the MCP will be connected by a in-vacuum feedthroughs to several high-voltage power supplies, with potentials ranging from -4000 to -1000 V. These power supplies can be bought commercially.

1.4.4. Vacuum Chamber and In-vacuum Components

Due to the small nature of the screens, most of the work and the mounting for this device can be done in a small chamber like a CF 63 tube with a CF 40 cross for the photon beam. The screens should be mounted on a linear motor that can be driven in and out of the beam that is either encoded or otherwise marked to match a screen position with the motor movement. The chamber should have a CF 63 window flange on one side to allow access to the out-of-vacuum optics and the camera.

To prevent damage to the mirror from impact from the FEL beam, an off-axis alignment for the screen and mirror would be preferable. Such a design has been implemented already at PSI for the electron beam profile monitors, and a simple sketch of it is shown in figure 4. The PSRD would not need such a setup since the light that would be measured by it will be too low intensity to cause any damage to the mirror surface.

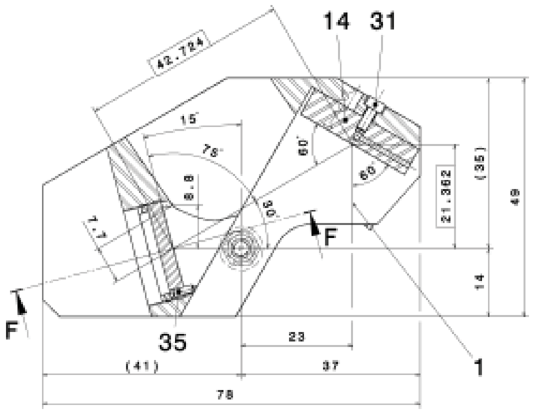

Figure 1.4.4.1: A technical drawing of the screen/mirror geometry used for the electron beam profile monitor at the PSI injector test facility. The x-ray beam comes in from the right. 35 is the scintillating screen, 14 the mirror, and 31 the mirror holder.

The full chamber should resemble something like the photo in figure 5, a profile monitor from the SACLA free electron laser.

Figure 1.4.4.2: SACLA photon beam profile monitor chamber.

Due to the small size of the chamber, no vacuum pumps are foreseen for them. They will be placed in the vicinity of larger, more critical optical components that should be able to handle the pumping for such a small chamber as well.

1.4.5. Cameras and Optics

The current setups used at PSI use a variety of gigabit Ethernet cameras to display the profiles of electron and photon beams. However, the only cameras that can work at 100 Hz and is already integrated into the PSI EPICS system is the PCO Edge and the Andor S-Cemos chip camera. Of these two, PCO Edge is the more convenient camera for use and integration, and is already used for other purposes at PSI. Therefore, we would likely take the same type of camera for the PSRD and one of the PBPR detectors. This camera has 6.5 μm x 6.5 μm pixels on a chip that is 16.6 mm x 14 mm, which should be sufficient for a 10 μm FWHM resolution, provided that appropriate optics are installed for focusing. The cameras need at least 12 bits per pixel to reach the sensitivity needed and still have enough dynamic range.

The slower cameras used for the majority of the PBPR monitors only have to have a relatively slow repetition rate of around 20 Hz. PSI currently uses Basler scout-series monochrome cameras that would also fit our purpose, though other firms (like Andor, PCO, ImperX) offer similar cameras at similar prices. A camera similar to the Basler sca1300-32gm would suit our purposes.

The optics and lenses would need to be chosen to fit the correct distances in the chamber and the camera properties. Figure 6 below shows a rough sketch of an optical setup and a choice of lenses that would be needed to make the design fit. The lenses are common and easily purchased from a variety of firms.

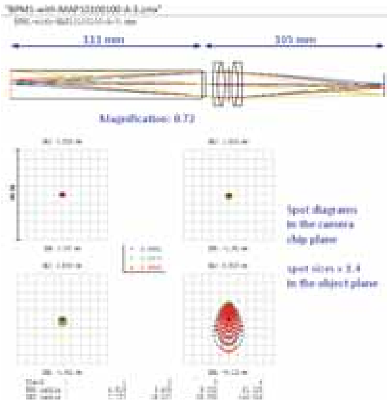

Figure 1.4.5.1: A rough optical setup sketch for the PBPR, courtesy of Vincent Thominet.

1.4.6. Controls System, Interlocks, and Interface

Most available cameras can be controlled remotely by a desktop windows PC, and the controls system should be able to interface with such a setup. The current setup used at the PSI injector test facility has a EPICS interfacing sees the slower Basler cameras hooked up by Ethernet cables to a network that is connected to a PC controlling them, while the PCO Edge camera uses a separate, unique connection to a PC via a special cable. It is expected that the PCO Edge camera will be updated to a rocket IO interface with a fiber optics cable for easier control and cabling in the near future.

The cameras are controlled from window PC servers which then deliver data to an EPICS channel. Though this data, at present, only shows the direct images, SwissFEL will require additional data along with the images in the future. In particular, the images should be indexed or synchronized to the electron/photon pulse that produced them, and some basic analysis should be available with the images as well. This type of analysis is currently under development for the electron profile monitors.

Additionally, we should have the ability to remotely turn the camera on and off, and be able to control the motors of the devices. The screens should be soft-interlocked with the machine so that the operators know that a screen is in the beam while they are producing light to avoid confusion from other diagnostics tools downstream of the screens.

Lastly, the data from the monitors should be archived for future use.

1.4.7. Analysis Software and Data Storage

The simple analysis software (center position and Gaussian profile) should be available on a per-image basis. Additionally, the images produced by the cameras should be easily transferable into a Matlab or other analysis program for further inspection if necessary.

The images taken by the camera should be saved to a server for a short period of time (a week or so) during which those interested in the images can download them. After this time, the images should either be reduced or only the automatic data (like the beam position and Gaussian profile) should be saved for longer-term storage.

Since the screens are mostly destructive, their use is not foreseen on a constant basis. Typically, they would be used at the beginning of a beamtime to check alignment and beam profile, and sometimes introduced into the beam during an experiment to ensure everything is all right. This means that most of the images collected by the cameras will be collected over the period of about an hour during the normal operation of the FEL. However, since the screens, and the spontaneous radiation detector in particular, are meant to b used for commissioning, we can expect a much larger number of images and data to be taken during the commissioning process of SwissFEL.

1.4.8. Linear Motion and Supports

Outside of the single motor needed to lower the monitoring setup into the beam, no other motors are foreseen for the PSRD or the PBPR. The chamber accommodating them will need to be mounted on supports, however, and the camera and optics setups need to be placed nearby as well. The camera should also be enclosed to prevent ambient light from disturbing our signal.

1.5. Single shot spectrometer

1.5.1. Concept

The basic concept behind the PSI-proposed single shot spectrometer is to combine a diffraction grating with a bent crystal to create a highly-resolved, non-destructive way of measuring the spectrum of the FEL pulses. While the basic theories behind both of these optical elements have been known for years, this document presents a short summary of the physical concepts for this device.

The dispersive diamond grating with a pitch much smaller than the size of the beam, when placed into the FEL beam, causes non-zero harmonics of the light to split off from the main beam. The device proposed here would use such a grating, with a pitch on the order of 100 nm for a 100-200 µm rms FEL beam, to split off the first order of the light and shine it onto a bent crystal further downstream. The angle at which the higher-order light leaves the grating is described by $\sin q_m = ml/d$, where d is the pitch, m is the order of the harmonic, and l is the wavelength of the light. With the first order harmonic and a pitch was 100 nm, the angle would be between about 1 and 7 mrad for the wavelength range between 1 and 4 Å. These small angles mean that the design of the whole device needs to have a large distance between the diffraction grating and the bent crystal that is to be used for the measurement of the spectra, mainly to separate the first order beam from the main beam over the whole range of photon energies that are to be studied. The diamond grating was chosen as the element of choice because of the high transmission and hardness of the material, allowing the device high resistance to the FEL beam while simultaneously allowing the overwhelming majority (over 95% at 6 keV) of the x-ray pulse to pass through it undisturbed for a 4 µm thick grating.

The first (or higher) order light from the diamond grating would impact the bent Si crystal placed several meters downstream of the diamond grating. When an x-ray beam with a very small divergence and a small (and limited) bandwidth impacts the convex side of a bent crystal in such a way so that the dispersion of the spectrum is parallel to the bend of the crystal, different portions of the spectrum have different incident angles on the crystal. Each part of the beam would satisfy a slightly different Bragg condition for its wavelength, $l = 2a \sin q_B$, where a is the lattice spacing and q_B is the Bragg angle. The radius of curvature r of the crystal determines the angle of the reflected beam. The dispersion of the spectrometer on the detector plane Dx for an energy interval DE is given by

$$\Delta x = 2\tan\theta_B\left(\frac{r\sin\theta_B}{2} + L\right)\frac{\Delta E}{E} \tag{7}$$

where *L* is the distance from the crystal membrane to the detector plane. The maximum *DE* for a given bent crystal depends on the size of the incoming x-ray beam *s* and the radius of curvature *r*

$$\Delta E_{\max} = E\frac{s\cot\theta_B}{r\sin\theta_B} \tag{8}$$

Figure 1.5.1.1 shows this relationship below.

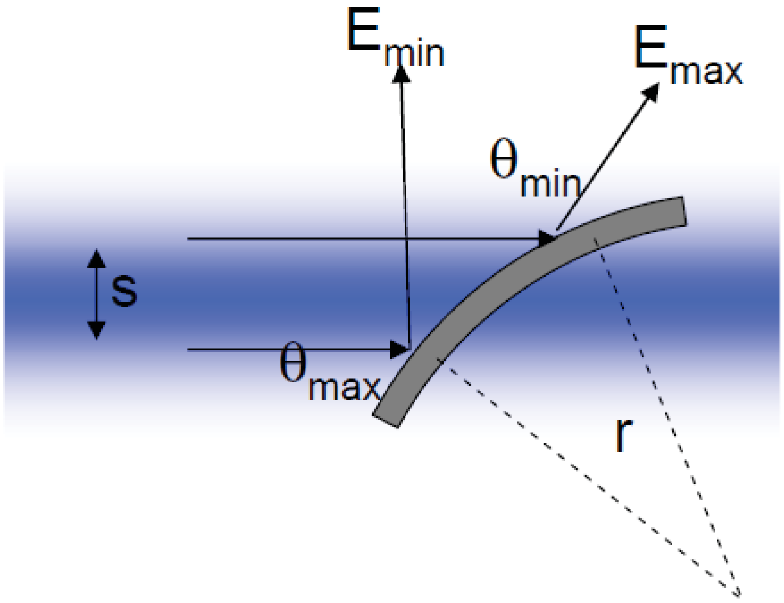

Figure 1.5.1.1: The schematic drawing of the conditions for Bragg reflection, courtesy of C. David.

Equations (7) and (8) place limits on the effective range of the photon energy of the spectrometer, and the geometry of the detector that would be used to observe the light coming from the bent crystal. The types of bent crystals that are most easily used for this purpose are Si <111> and Si <333> oriented crystals, which give different Bragg angles at different wavelengths. They also meet the requirement for 10^{-4} and better energy resolution if bent properly.

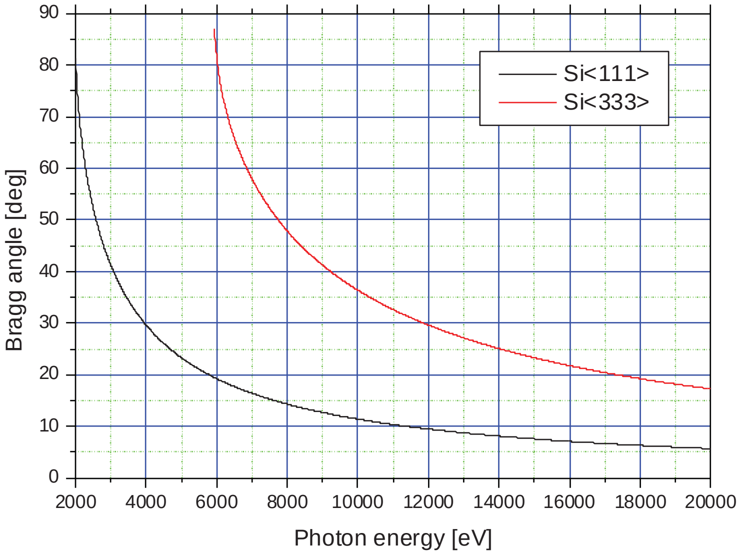

Figure 1.5.1.2: The Bragg angles vs. photon energy for the Si <111> and Si <333> bent crystals, courtesy of C. David.

As figure 1.5.1.2 above shows, the Bragg angle becomes large at lower photon energies, making it impossible to fit a detector into the setup—it would need to be placed in a back-reflection geometry, in a vacuum chamber, along the same path that the refracted beam itself is taking, without interfering with the 0^{th} order FEL pulse. The size of the pixel or pitch of the detector *Dx* directly affects the *L*, the distance between the detector and the plane of the crystal membrane. For the Si bent crystals in figure 2, a detector with a 50 µm pitch would need to be placed a meter or more away from the crystal, and have the ability to move through a range of angles to observe the Bragg reflection. A smaller detector pitch or pixel size would make this distance between the detector and the crystal membrane correspondingly shorter.

The last hurdle this detector has is the radius of the bent crystal itself. To be able to see larger energy bandwidths, the radius of curvature needs to be smaller. For a fixed size of an incoming x-ray beam, this is the only parameter the designers can control. In case of SwissFEL, with its 100-200 µm rms diameter pulse, the bending radius of the crystal would need to be on the order of 10 cm to meet the energy resolution requirements. If a way can be found to make the incoming beam more dispersed, then the bending radius could be larger and easier to implement. The actual method to be used for the bending of the crystal needs to be tested, and several options are available: a micromotor to bend the crystal, attaching the crystal to a pre-defined bent surface, or using lithography to create the bent crystal of appropriate radius. The total sketch of the concept is shown in figure 1.5.1.3.

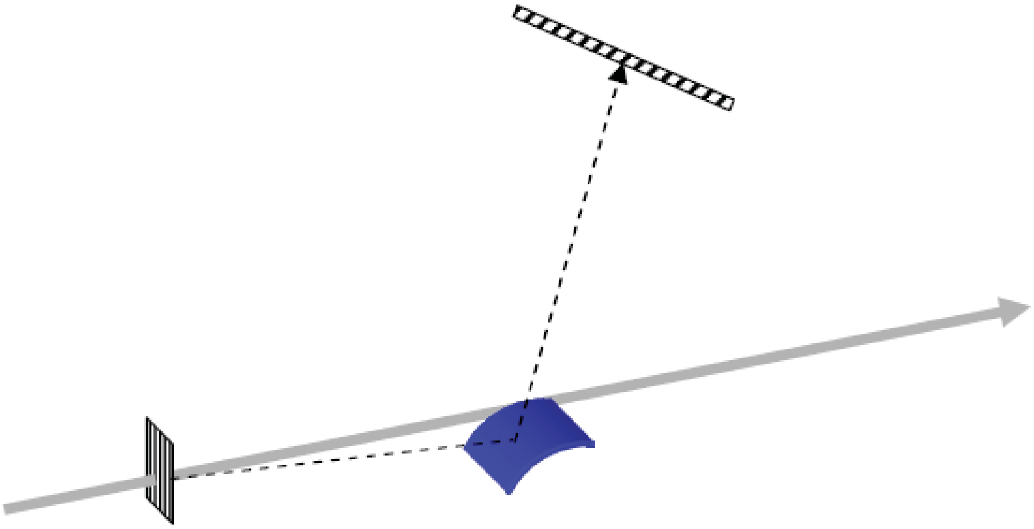

Figure 1.5.1.3: Concept drawing of the single shot spectrometer, courtesy of C. David.

1.5.2. Choice of Detector

The two methods of observing the x-rays reflected from the bent Si crystal are via a scintillator-and-camera setup, or with a pixilated x-ray detector. Both cases have their advantages and disadvantages, and further testing and experimentation needs to be done before a choice can be made for SwissFEL.

The Gotthard detector, developed at PSI [4], is a pixilated x-ray detector with high sensitivity that is meant to be used in scattering experiment at synchrotrons and

FELs. It has adaptive gain, high processing speed, and can be easily integrated into existing PSI infrastructure due to existing synergies at PSI. It can easily meet the 100 Hz requirement, and will be used at the European XFEL to meet that machine's 2 MHz repetition rate requirement. The downside of the detector is that it has no sensitivity to softer x-rays, and has a detector pitch of 50 μm, requiring it to be placed a meter or more away from the bent crystal it is meant to observe. Because of the great distance between the detector and the screen, the intervening space would need to be filled with He to reduce the absorption of the x-rays as they pass through the air, and a beryllium window would need to be installed in the vacuum chamber to allow the x-rays to pass from the crystal to the detector unperturbed. Finally, the detector would need to be moved over a wide range of angels, which could be a problem if there is not enough space for such a device in the SwissFEL tunnel. Future developments with the Gotthard could bring its detector pitch down to 25 μm, which could make it easier to install.

The second option for the detector is a scintillator screen with a strip-line (1D) camera behind it. The advantage to this approach is that the scintillator screen pixels can be very small, down to only several micrometers in size, and could be placed about 10 cm from the Si crystal, perhaps even in vacuum. The 1D camera, which can also have pixels of only a few micrometers, would be placed outside of the vacuum and look at the visible light generated by the scintillator through a standard window flange and some optical elements. The setup could be placed nearer to the bent crystal membrane, and there would be no need for a He-filled container to mitigate the absorption of hard x-rays in air. Being able to observe the Bragg-reflected signal in 2D may give additional useful information, but would not need to be in the feedback system. However, the efficiency of a scintillator screen is smaller than the efficiency of the Gotthard detector, so there is a possibility that the signal the camera sees from the first order diffraction may not be sufficient for the resolution required. Though past experiments at LCLS with a focused diffraction grating [3] have yielded sufficient light, more experiments are needed to find if this option is the best one.

In both cases, for the Gotthard or for the scintillator-and-camera setup, software and hardware needs to be developed at PSI to allow the use of these devices for feedback and monitoring. The feedback, due to the requirements from the machine, would most likely need to be more hardware-based.

1.5.3. Detector Hardware and Firmware

The 100 Hz feedback from the single-shot-spectrometer detector needs to deliver the average photon energy and the bandwidth on a shot-to-shot basis to the machine. This feedback needs to be delivered to the machine within a 2-4 ms timeframe to enable the tuning of the machine on a shot-to-shot basis in a feed-forward setup. Because software solutions for feedbacks all have an enormous jitter in their reporting, with no possibility of ensuring that the information from the detector is sent to the feedback by a certain time (like 4 ms), the most obvious solution for the feedback is FPGA programming on a IOC card. Though such a setup does not exist at PSI at present, it is achievable—both the Gotthard detector and 1D cameras have simple Gigabit Ethernet connections which interface well with most IOC cards, and are compatible with the IOC card chosen to be one of the pillars of SwissFEL, the IOxOS. In case we choose a more complex camera for the measurement, like the one developed for the Gigafrost project at PSI, the infrastructure for it could be copied from an existing project, although the camera used for the spectrum measurement would exceed the needs of the device.

1.5.4. Vacuum Chamber and In-Vacuum Components

The expected collaboration between PSI and the European XFEL is expected to deliver a design for chambers that would hold the diffraction grating and the bent crystal screens. The two chambers would then be installed as modules along the FEL beam pipe, with the detector hardware and other linear supports built around them. The expectation for vacuum is that the module containing the diffraction grating(s) will have a motorized stage to move the grating(s) in and out of the beam. The stage would require an encoder to ensure that the grating(s) are correctly positioned in the beam.

The module containing the bent crystals would have either a series of crystals with different radii on a stage that can be moved in and out of the diffracted beam, and/or an in-vacuum setup that may include a motor to make the crystal bend to the radius required for the measurements. In addition to the motors, the chamber would have a window flange (Beryllium for the Gotthard, normal for the camera) through which the x-rays or visible light from the scintillator would pass through. Both of these devices would need to be observed with vacuum interlocks. As the designs for the devices get closer to being finalized, the exact specifications for the vacuum interface will be determined.

1.5.5. Controls System, Interlocks, and Interfaces

The controls interface for the PSPH needs to deliver active feedback to the machine. This means that an FPGA program on an IOC card needs to be created to deliver the mean photon energy and bandwidth of the observed x-ray spectrum from the spectrometer on a shot-to-shot basis.

Furthermore, the data from the spectrometer should be available to users and other interested parties, along with a software package that can be used for further analysis of the spectra off-line. This feature does not need to be fast nor in feedback, but should provide some basic tools for those interested in examining the x-ray spectra more closely.

The PSPH should be interlocked so that it can not be used under conditions that would damage it, like at low photon energies, and some components would need to have end-switches installed so that they are not driven into the 0th order beam by mistake. The device should be connected to the general SwissFEL vacuum and electric interlock system, and be shut down in case of any power or vacuum failure, with the safety valves closing to protect the equipment in the vacuum chambers. There should be similar oversight of the detector component of the PSPH, with it shutting down in case of power surges or other adverse conditions. The detector should be able to be turned on and off and calibrated remotely.

The spectra and raw data taken by the PSPH need to be stored and archived for future use.

1.5.6. Analysis Software and Data Storage

Besides the feedback analysis, the analysis software package for the PSPH should offer a basic set of tools for analyzing spectra, as described earlier. Both the feedback data and the spectra themselves should be saved for a period of about one year, and afterward should be compressed or otherwise averaged and put into longer-term storage. Because of the nature of the device, the data acquisition rate is not extremely high for this device since it uses1D detectors. The data storage should be simpler than for cameras or other devices.

The data should be retrievable with some kind of a tool that would allow someone to search for a specific spectrum by time stamp, data, experimental number, or other reference. Such a software package should be available to both users and operators.

1.5.7. Linear Motion and Supports

Besides the motors described earlier to move the grating and the bent crystals, there may be a need for further linear motion. The module that has the bent crystals may be required to shift by up to a millimeter to accommodate new angles or optimize the geometry of the setup. To that end, a table that can accommodate about a millimeter of movement in the directions transverse to the propagation of the photon beam may be required. As the design of the detector becomes more developed, the requirements for linear motion and support will become better defined.

1.6. Photon Pulse Length and Aarrival Monitor (PALM)

1.6.1. Concept

The accurate non-destructive measurements of the arrival time and the few-femtosecond pulse length at free electron laser (FEL) sources are vital to understand the atomic, molecular, and chemical dynamics often being probed at these facilities. Furthermore, such measurements are important for the operation of an FEL, as they can provide a feedback to the functioning of the machine, and allow the operators to better control the quality of light they deliver to the users. To this end, several methods have been proposed over the years to measure both the pulse length of the FEL beam and its arrival time relative to a pump laser at an experimental station, like THz streaking [13], transmission/reflectivity spatial and spectral encoding [15]. The methods that have been proposed and used thus far have different limitations--for example, the transmission or reflectivity-based spectral encoding methods only yield information about the arrival time while THz streaking has its resolution limited by the shot-to-shot time-jitter of the FEL pulse.

The only method that has been proven to be able to achieve time resolution measurements below the 10 fs and down to sub-fs FWHM regime is the THz streak camera taken to its limit and operated as a petahertz streak camera [10,11,12] in a well-controlled tabletop laser laboratory. However, such accuracy is not easily achievable at an FEL because they cannot, as of yet, reach the level of time stability achievable in a tabletop laser laboratory.

To address these issues, the advanced diagnostic concepts and photonics groups at the Paul Scherrer Institute have developed a concept for a better pulse length and pulse arrival measurement method for the future SwissFEL project that could give few-fs resolution measurements while being very insensitive to the timing jitter of the FEL. The method utilizes a pair of THz streak cameras set up downstream of each other and two infrared radiation sources with a locked 90° phase-offset between them to measure pulse length. The combination of this setup with a spectral encoding setup behind it could also be used to achieve few-fs arrival time resolution.

1.6.2. THz Streak Camera

Conventional streak cameras use photocathodes to generate electron bunches that mimic the structure of a light pulse, are accelerated by a rising electric field, and then transversally deflected onto a screen according to their kinetic energy. However, the time resolution of such a setup is limited to several hundred femtoseconds [8,9]. A THz streak camera corrects the main source of error, the initial dispersion of kinetic energies from the photodiode, by using a gas photoionized by the x-ray beam as an electron emitter that is completely contained within the deflecting electric field—an infrared or near-infrared streaking field [10,11,12]. An excellent explanation of the THz streak camera concept is presented in [12], but this document presents a short summary below.

The simplest description of the THz streaking phenomenon uses the semi-classical approach. In this approach, we assume that streaking electromagnetic wave $E_{Thz}(t)=E_0 cos(\omega_{Thz}t+\phi)$ interacts with a photoionized electron with a kinetic energy of $K_i=\hbar\nu-W$ where W is the atom's electron binding energy. In this case, the final kinetic energy of an electron drifting parallel to the electric field would be

$$K_f = K_i + 2U_p \sin^2(\phi_0) \pm \sqrt{K_i U_p}\,\sin(\phi_0) \qquad (9)$$

where ϕ_0 is the phase at the instant of ionization and

$$U_p = \frac{e^2 E_0^2(t)}{4 m_e \omega_{Thz}^2} \qquad (10)$$

with e and m_e being the charge and mass of the electron, respectively. The middle term of (9) can be ignored in when $U_p << K_i$, as is often the case with x-ray photoionization. Therefore, the final kinetic energy of the photoelectron is dependent only on the ponderomotove potential at the time of ionization and the photon energy of the x-ray pulse. Since the potential varies with time and the photon energy of the x-ray pulse stays constant, the final kinetic energy of the electron varies with the phase of the potential at the time of ionization--that is, its final kinetic energy shifts depending on when during the electric field cycle it is photoemitted.

This shift in the final kinetic energy of the photoelectron can be used to calculate when during the terahertz or infrared pulse the photoionization took place. For a larger number of electrons generated by x-ray pulses at FELs, the difference in the final kinetic energy between the electrons ionized at the beginning and the end of the x-ray pulse can be used to calculate the length of the x-ray pulse as well.

Unfortunately, a FEL cannot match a laboratory setup with a self-synchronized high harmonic generation (HHG) x-ray source in arrival time stability, and the FEL pulse can arrive outside of the 'target' terahertz cycle, or on a part of the terahertz cycle where the difference between the final kinetic energies of the photoelectrons is not easy to evaluate--areas of the cycle that are not linear, like near the maxima and minima of the THz vector potential. Similarly, if the x-ray pulse is longer than the part of the THz cycle that contains a linear vector potential slope, a part of the x-ray pulse will be in the non-linear region and make the evaluation of the pulse length difficult--every pulse longer than the length of the linear region of the potential will yield the same final electron kinetic energy dispersion. The x-ray pulse must be shorter than the part of the THz cycle that has a linear vector potential slope.

To deal with these issues, most THz streak camera setups up to now have concentrated on creating THz fields with frequencies that were long enough to accommodate the x-ray pulse length [12,13]. Similarly, one could attempt to use single-cycle THz pulses to reduce the uncertainty of the position of the x-ray pulse relative to the THz pulse. Such pulses have been developed for experimental purposes already [14].

The main problem with single-cycle THz fields, however, is that they have to match or exceed the expected (or measured) jitter of the FEL they are supposed to characterize, which can be on the order of hundreds of femtoseconds. This typically means that the THz field has to have frequencies that are difficult to reach--between 2 and 15 THz. Similarly, since it is best to have the maximum slope of the field in the linear region, a shorter frequency that may be easierto achieve would require a higher maximum field strength, introducing more difficulties for the THz generation. Infrared frequencies of 20 THz and above are reachable with high maximum power, but their single-cycle pulse is usually too short to fit the jitter of the FEL.

To solve this problem, PSI has developed a method of combining two THz streak cameras with THz fields offset by 90 degrees from each other. In such a setup, the photoelectrons being ionized will always see a linear part of the field in one of the two streak cameras, giving an accurate measurement of the pulse length regardless of the jitter of the FEL, leaving only the FEL pulse length as the limit on the THz cycle-length. Similarly, because the THz cycle no longer has to match the FEL jitter, the streak camera setup can use a continuously cycling infrared or THz field instead of a single-cycle pulse. For example, a 20 fs-long FEL pulse would require a 20 THz continuously cycling field. This method, when combined with a rougher method for x-ray pulse arrival time measurement (like spectral encoding), can be used to also calculate the arrival time of the x-ray pulse relative to a laser pulse with femtosecond accuracy.

1.6.3. Spectral Encoding

An excellent summary of the use of spectral encoding to measure arrival time of an x-ray/potical delay with transmitted light is presented in [15], and this document presents a short summary here. Spectral encoding chirps an optical pulse so that different wavelengths of the optical pulse arrive at an interaction point at different times. The interaction point, a thin semiconducting foil, transmits the light with different efficiencies depending on whether the foil was illuminated with x-rays from the FEL or not. When the foil is illuminated by the x-rays, its transmission of visible light increases [16,17], giving rise to a step function in the spectrum of the optical pulse when read out by a spectrometer. This method has been used to measure to resolve the arrival time of the LCLS x-ray pulse to 10 fs RMS, and can possibly reach even better values with further development and research. An example of such a setup is shown below.

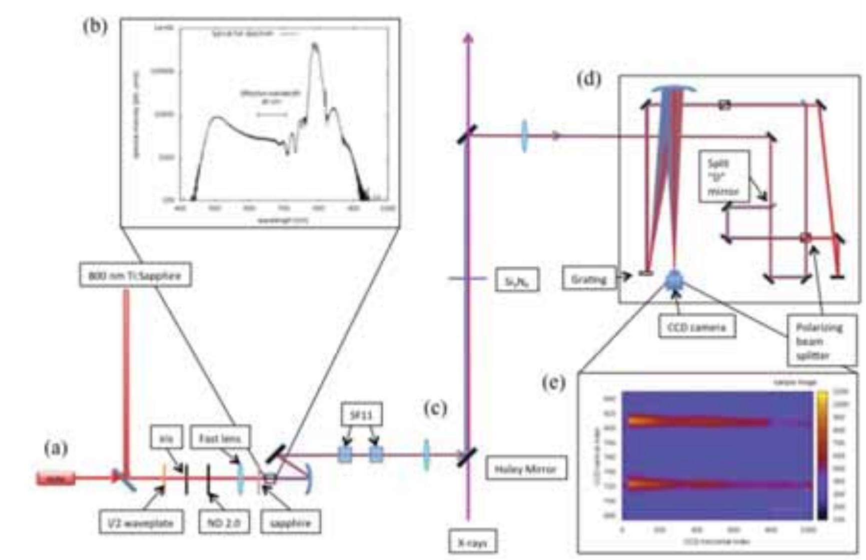

Figure 1.6.3.1: The spectral encoding setup used at LCLS (courtesy of R. Coffee from LCLS).

When such a method is combined with the multiple THz-streak-camera setup described above, it could be used to cycle-encode the infrared pulse. That is, if the optical and infrared pulses are synchronized, optical encoding can be used to figure out which cycle of the many-cycle infrared field was the one that 'saw' the FEL beam. Once identified, the information within the cycle could then be used to figure out a more accurate x-ray arrival time, and the pulse length of the FEL. The proposed schematic setup is shown below in figure 1.6.3.2. The delay stage would introduce the 90 degree offset between the two THz/IR streak setups.

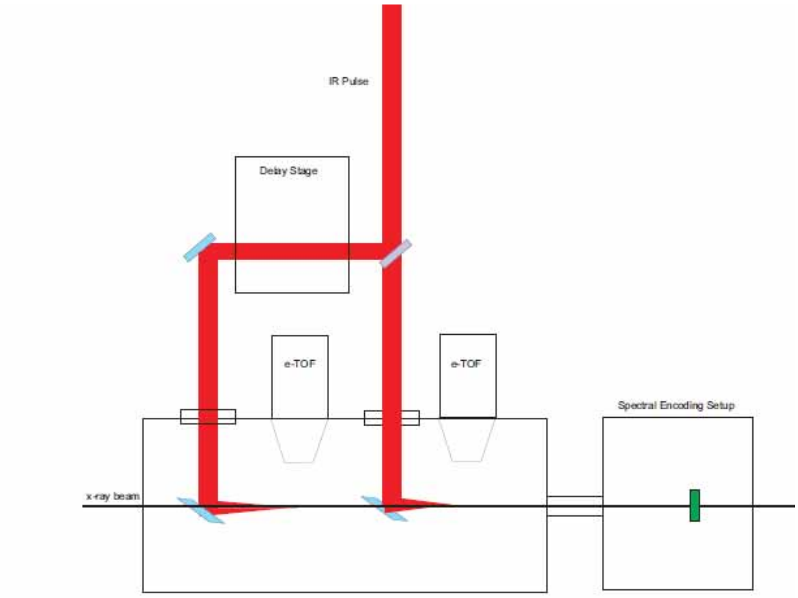

Figure 1.6.3.2: The schematic of the proposed PALM setup.

1.6.4. Electron Time-of-Flight Spectrometers

The electron time-of-flight (eTOF) spectrometer is a standard tool in atomic, molecular, and surface physics, used to probe the electronic structure of materials. In its simplest form, it is a drift tube that measures the time between the photoionization of a sample by a photon and the arrival time of an electron flying through a drift tube. The time of flight in the drift tube can be used to calculate the photoelectron's kinetic energy, which can be used to gain valuable information about the structure of the material being studied.

In the case of x-ray photoionization, the kinetic energies of photoelectrons typically become higher as the photon energy of the incoming x-ray beam increases. Because the resolution of a time-of-flight spectrometer is a tied to flight time, while the kinetic energy of an electron goes as the square inverse of flight time, to get a good energy resolution for high energy photoelectrons, one needs to use an electrostatic retardation and lensing system in the eTOF to have the best resolution and largest count rate possible. This experiment used a modified Kaesdorf ETF20 eTOF made to be able to measure photoelectrons with kinetic energies up to 10,000 eV with a time-of-flight resolution factor of up to 1000, which cover the range of most hard x-ray FELs, like SwissFEL, LCLS, SACLA, and the European XFEL.

Since most of the electrons ionized at hard x-ray photon energies tend to have very high kinetic energies, the primary assumption one can make about the angular electron distribution is that it will mostly follow the polarization vector of the x-ray pulse [18]. This means that the most efficient placement for the eTOFs would be in the polarization plane of the FEL beam, to increase the number of electrons that would fly towards the eTOF for the largest range of photon energies.

A further effect that has to be taken into consideration is the inverse square relation between the electron kinetic energy and the time of flight. To get the best kinetic energy resolution, the electrons should be as slow as possible, while the dynamic range of the eTOF should large enough to see the full range of electron kinetic energies that could be reached because of the THz streaking field. This means that strong retardation on the eTOFs is an absolute necessity for any photon energies higher than the Xe 2s binding energy of 5453 eV, the highest reasonably achievable electron binding energy of a noble gas below 14,000 eV.

1.6.5. Pulsed Gas Jet

As the photon energy increases, the photoionization cross sections of the noble gases used for the THz streak camera decrease [19]. For example, the difference between the cross section of xenon between 90 eV photon energy and 14,000 eV photon energy is about four orders of magnitude.

This reduction in the cross section at higher photon energies has to be compensated if the method is to have a sufficient number of electrons to see the THz streaking effect. An Amsterdam cantilever piezo valve system [20] can provide about $3.3\text{x}10^{13}$ cm^{-3} particle densities 160 mm away from the nozzle, which should increase the amount of gas in the interaction of the eTOFs by four or five orders of magnitude from what one would see if one simply flooded the experimental chamber to the same pressure without the nozzle. In other words, the use of the pulsed gas valve or some similar device is necessary to increase the number of gas atoms and photoionization events in the interaction region at higher photon energies. In our case, we mounted the cantilever piezo valve system on an XYZ stage placed 25 mm above the x-ray photon beam, and could optimize its position relative to the eTOFs with the signal intensities from the eTOFs.

1.6.6. Controls Systems, Interlocks, and Interfaces

The controls system for the PALM requires extensive expert panels. The THz streak camera needs the control of the pulsed gas valve position, frequency, and delay relative to the THz pulse, the ability to automatically change the type of gas being pulsed into the chamber, control over the potentials applied to the various parts of the eTOFs, controls for the position of the THz beam focus, information about the spectrum of the photon beam (taken from the single-shot spectrometer), information about the theoretical electron or photon pulse length, and a feedback system to send the information further to the machine. Furthermore, the controls system would need to display and record a shot-to-shot measurement of the THz field strength (taken from a virtual focus), and perform a fairly complicated analysis to find the position and width of the peak being streaked. That analysis would then be used by another analysis program to calculate the length and arrival time of the X-ray pulse.

The spectral encoding setup requires the control and oversight of the chirp of the optical laser, the display of the signal of the spectrometer, the analysis of the signal from the spectrometer to find the approximate arrival time of the X-ray beam, controls over any motors in the chamber (like the thin foil stage). The information from the spectral encoding setup would be combined with the information from the THz streak camera to create a more accurate measurement.

The controls would also need to have oversight over the chambers' vacuum, and control and implement any safety interlocks necessary to protect the equipment in the chamber (like the MCPs of the eTOFS), and any valves the chamber has. Additionally, the data gathered by the devices would need to be analyzed and stored.

1.6.7. Analysis Software and Data Storage

The spectra taken by the PALM need to be processed in accordance to the parameters described in the concept section. The position and width of the spectra need to be saved, and checked agains the spectra taken by the single-shot-spectrometer, which will be used as a reference. This data would then be combined with the data on the strength of the THz field and the data evaluated from the spectral encoding setup to extrapolate the arrival time and the pulse length of the x-ray.

The raw data (THz field strength, spectral encoding data, and eTOF spectra) all need to be saved for some short period of time for possible further analysis, and then should be somehow compressed afterward. Additionally, the combined data about the pulse length and arrival time should be stored for the duration of the experiment plus a few weeks, after which they can be compressed and reduced.

Since this is a device that is not going to be used for direct feedback on the machine, the complete evaluation of the data need not be one on a shot-to-shot basis, but can be done in intervals of a second or several seconds. That is, a set of spectra, spectal encoding data, and THz field data can be taken, and then the final numbers simultaneously evaluated, rather than evaluating them one at a time every 10 ms. This data will be used by the operators and users to improve machine and experiment performance.

1.7. References

1. K. Tiedtke et al., *Gas Detectors for X-Ray Lasers*, Journal of Applied Physics **103**, 094511 (2008).
2. J. H. Hubbel et al., *Atomic form factors, incoherent scattering functions, and photon scattering cross sections*, J. Phys. Chem. Ref. Data **3**, 471 (1975).
3. K. Tono et al., *Single-shot beam position monitor for x-ray free electron laser*, Rev. Sci. Instrum. **82**, 023108 (2011).
4. T. Kudo et al., *A photodiode amplifier system for pulse-by-pulse intensity measurement of an x-ray free electron laser*, Rev. Sci. Instrum. **83**, 043108 (2012).
5. M. Nikl, *Scintillation detectors for x-rays*, Meas. Sci. Technol. **17**, R37 (2006).
6. M. Yabashi, private communication.
7. Ozkan, C, private communication.
8. M. M. Shakya and Z. Chang, *Achieving 280 fs resolution with streak camera by reducing deflection dispersion*, Appl. Phys. Lett. **87,** (2005) 041103.
9. J. Fang et al., *An x-ray streak camera with high spatio-temporal resolution*, {Appl. Phys. Lett. **91,** (2007) 13412.
10. M. Hentschel et al., *Attosecond Metrology*, Nature **414**, (2001) 509.
11. M. Drescher et al., *X-ray pulses approaching the attosecond frontier*, Science **291**, (2001) 1923.
12. M. Uiberecker et al., *Attosecond Metrology with Controlled Light Waveforms,* Laser Physics **15,** (2005) 195.
13. U. Frühling et al, *Single-Shot Terahertz-Field-Driven X-ray Streak Camera* Nature Photon **3**, (2009) 353.
14. J. Hebling et al., *Generation of high-power terahertz pulses by tilted-pulse-front excitation and their application possibilities*, J. Opt. Soc. Am. B **25**, (2008) B6.
15. M. Bionta et al., *Spectral encoding of x-ray/optical relative delay*, Optics Express **19** (2011) 21855.
16. C. Gahl et. al., *A femtosecond X-ray/optical cross-correlator*, Nature Photon **2** (2008) 165.
17. M. Trigo et. al., *Imaging nonequilibrium atomic vibrations with x-ray diffuse scattering*, Phys. Rev. B **82** (2010) 235205.
18. D. S. Kennedy and S. T. Manson, *Photoionization of noble gases: cross sections and angular distributions*, Phys. Rev. A **5** (1972) 227.
19. B. L. Henke et. al., *X-ray interactions: photoabsorbtion, scattering, transmission, and reflection at E=50-30,000 eV, Z=1-92*, At. Data Nucl. Data

Tables **54** (1993) 181.

20. D. Irimia et. al., *A short pulse (7 μs FWHM) and high repetition rate (dc-5kHz) cantilever piezovalve for pulsed atomic and molecular beams*, Rev. Sci. Inst. **80** (2009) 113303.

Operation Mode and Safety Consideration

Luc Patthey, Roland Luecher, Rafael Abela

Contents

1. Introduction

User operation at the ARAMIS photon beamline of SwissFEL will start in 2017 [1]. ARAMIS will deliver photon from 2-12.4 KeV to three experimental hutches using three different optical beamlines called AR1, AR2 and AR3. The tree experimental hutches (EH1, EH2, and EH3) are located in series after the optical hutch (OP). A general layout of the ARAMIS photon beamline, including optical and experimental hutches, is given in the figure 1. In the first phase (< 2017) ARAMIS beamline will be a “single user” beamline, as only one experimental setup receiving FEL radiation at any time. The order in which the FEL radiation is distributed between the different experimental hutches is not predefined and will depend on the experimental program. When the FEL radiation is delivered to one experimental hutch, the access to other experiment hutches has to be possible for preparation of the next experiment/beamtime. In a second phase (> 2017) some kind of beam splitter (for example a large offset monochromator) could be used to distribute the FEL radiation to two different hutches simultaneously. Under these conditions, the access to the third hutch should still be guaranteed for preparation work.

2. Operation mode

To allow this operation scheme at the ARAMIS beamline, a set of Photon Beam Stopper (BST) and Collimator (CO) is proposed on the three beamlines. The Local Access Control system (LAC) of the individual hutches is ensuring that (a) no access is allowed during beam operation and (b) no beam operation is permitted when access is allowed. The optical hutch located before the first experimental hutch follows the same logic and is included in this operation mode. The experimental areas have been defined as zone of type 0 or I [1] following the criteria from [2]. When the LAC is in the “Open” state, a radiation dose rate below the guideline values 10 μSv/h [1, 2] has to be ensured to allow free access to the opened hutch. The various operation modes are illustrated in figures 1 to 3. In figure 1, the BST located into the tunnel is closed and prevent any radiation (Bremsstrahlung, spontaneous radiation and FEL radiation) to exit the tunnel. The LAC can be in the “Open” status (no beam operation allowed in any hutch) for the optical and experimental hutches. This configuration will be used to access to the optical hutch while having the SwissFEL accelerator in operation with full electron beam.

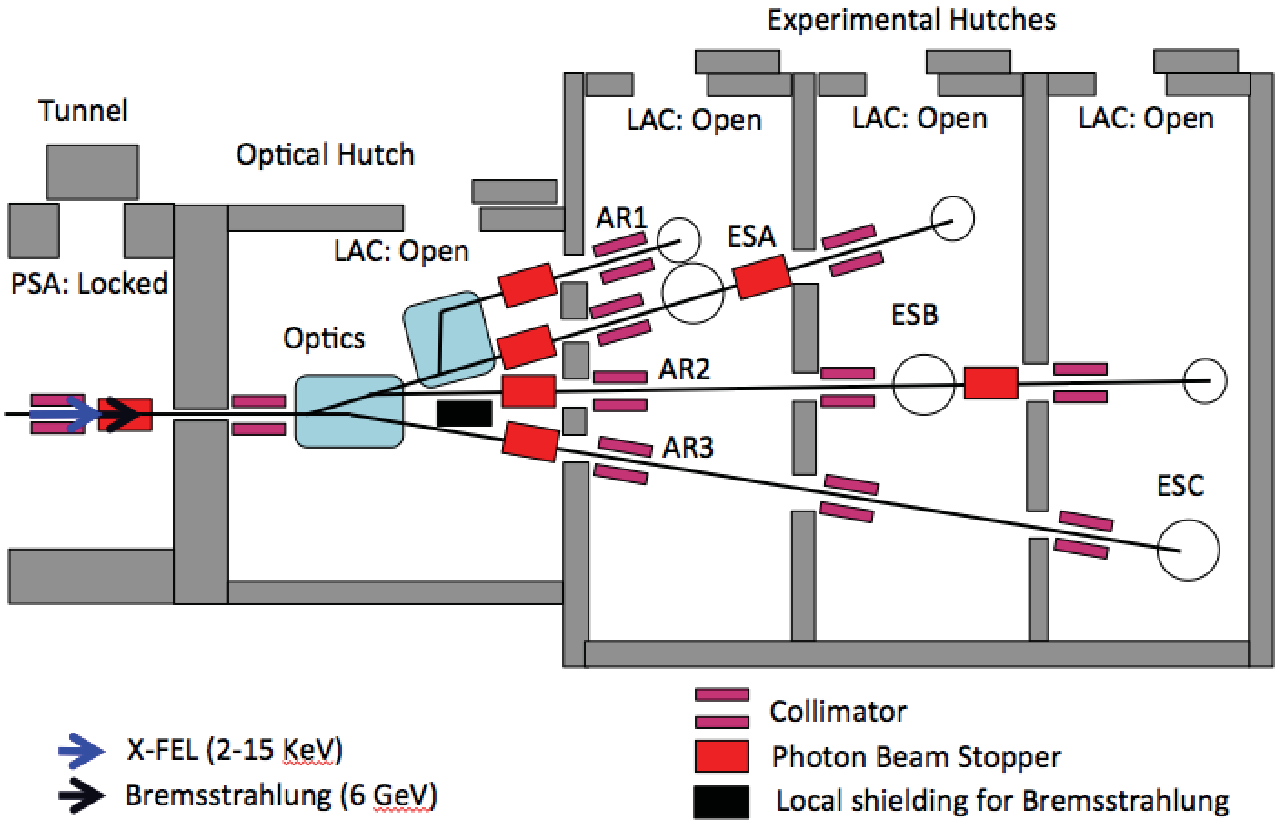

Figure 1: Operation mode: “Access to Optical Hutch”. The LAC is open for the optical and experimental

hutches. The beam splitter (for example a large offset monochromator) in indicated only on AR1 to not over load the figure, but the beam splitter can also be installed on AR3 beamline.

The figure 2 corresponds to the “Beam On in Optical Hutch”. The photon BST from the tunnel is open therefore the FEL radiation can reach the optical hutch. The LAC is locked for the optical hutch. The access to the three experimental hutches is possible and the BST for each beamline are closed. This operation mode allows the beam to go trough the optic components in the optical hutch (offset mirrors or monochromators) but not to the experimental hutches.

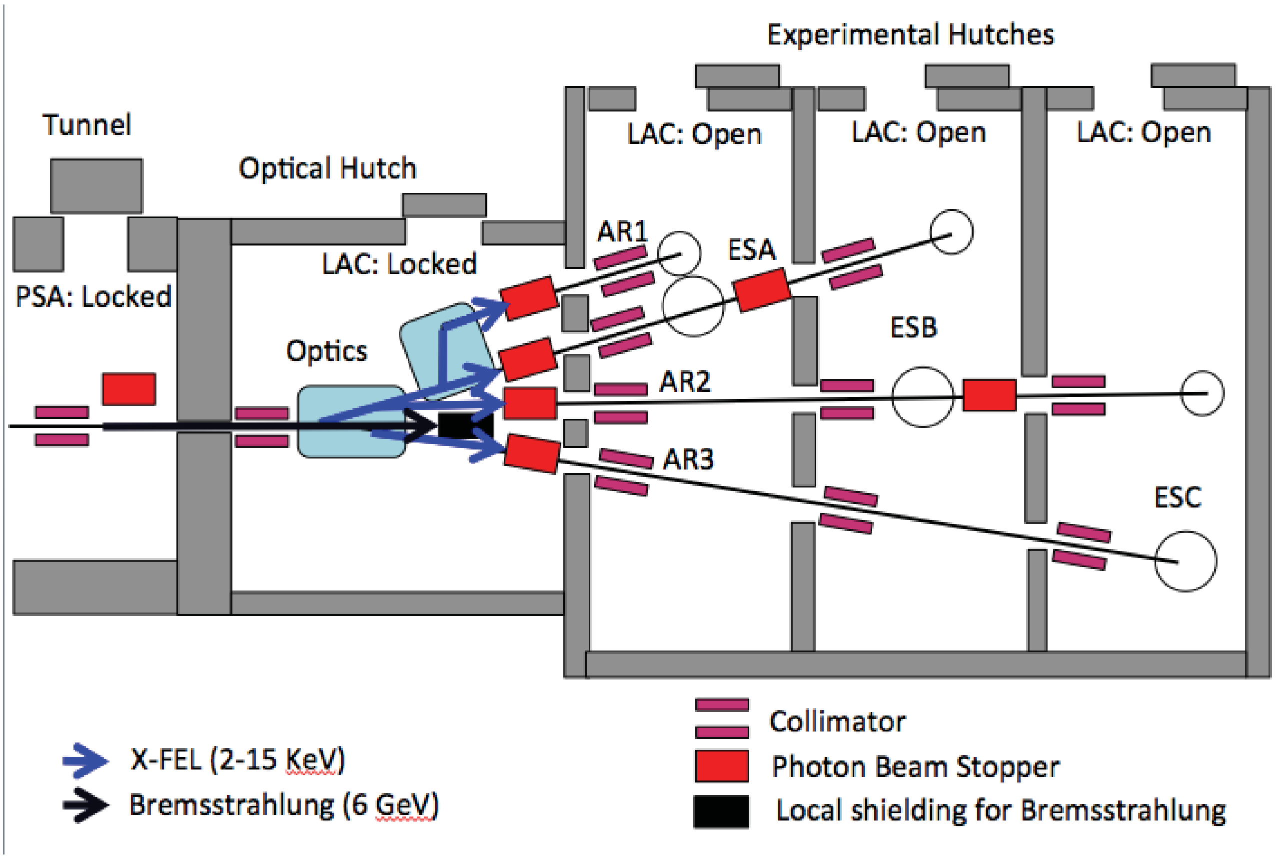

Figure 2: operation mode: “Beam on Optical Hutch”.

During normal operation, one of the experimental hutch receives the FEL radiation while the other hutches are still open for access. The figure 3 illustrates this mode: the beam is lead as an example to the second experimental hutch (EH2) through the beamline AR2. The BST in the tunnel and the BST of AR2 in the optical hutch are open. The LAC for the optical hutch and the second experimental hutch are locked. The access to the first and third hutches is still possible. Similar operation mode applies to the other hutches.

The status of the BST and LAC as a function of the operation mode of the beamlines are summarized in Table 1. As described in the introduction, the table includes the 1st (< 2017) and 2nd (> 2017) phases of the operation mode of ARAMIS.

3. Collimator

In the operation mode described in Figure 3, a collimator on AR2 located in the first hutch prevents the FEL radiation hitting the vacuum tubing of AR2. The free access criteria are fulfilled according to the radiation regulation [2]. The detail of this concept is given in figure 4.

The collimator limits the angular distribution of the Bremsstrahlung and the spontaneous synchrotron radiation along the beam path without intercepting the FEL radiation. The so-called “stay clean” (or opening of the collimator) depends on the location and function of the collimator (see table 2 for details). The collimators in the tunnel and in the optical hutch should have a 30σ stay clean for the FEL radiation to allow for the measurement of spontaneous radiation, needed during the commissioning of SwissFEL. On the other hand, the collimators in experimental hutches are limited to 10σ stay clean. The vacuum tubing in the experimental hutch should be bigger that 30σ stay clean.

The collimator has a B_4C-Air-Tungsten structure. The B_4C is used to stop the soft x-ray radiation and the Tungsten the hard x-ray radiation. The B_4C is an extremely hard boron–carbon ceramic material with a melting point of 2763 °C and high ablation threshold for soft x-ray. Boron and carbon have both a low atomic Z value and low soft x-ray attenuation. The energy distribution of the absorbed soft x-ray is more isotropic in the material, which gives a higher ablation threshold for low Z material. Therefore, the B_4C is well suited to stop the soft X-ray FEL and protects Tungsten from ablation from the soft x-ray. The air gap between the B_4C and Tungsten provides an intrinsic interlock in case of an improbable ablation of the B_4C. In such case the soft x-ray FEL radiation will develop a micro leak in the vacuum chamber and generate a vacuum interlock of the machine. The electron beam will be dumped before further damage occurs. This simple scheme prevents any radiation damage of the Tungsten structure and represents an optimal shielding without movable piece and complex mechanism. The same design has also proposed for LCLS II [3], where two BST are requested for each beamline to ensure the defined safety performance level.

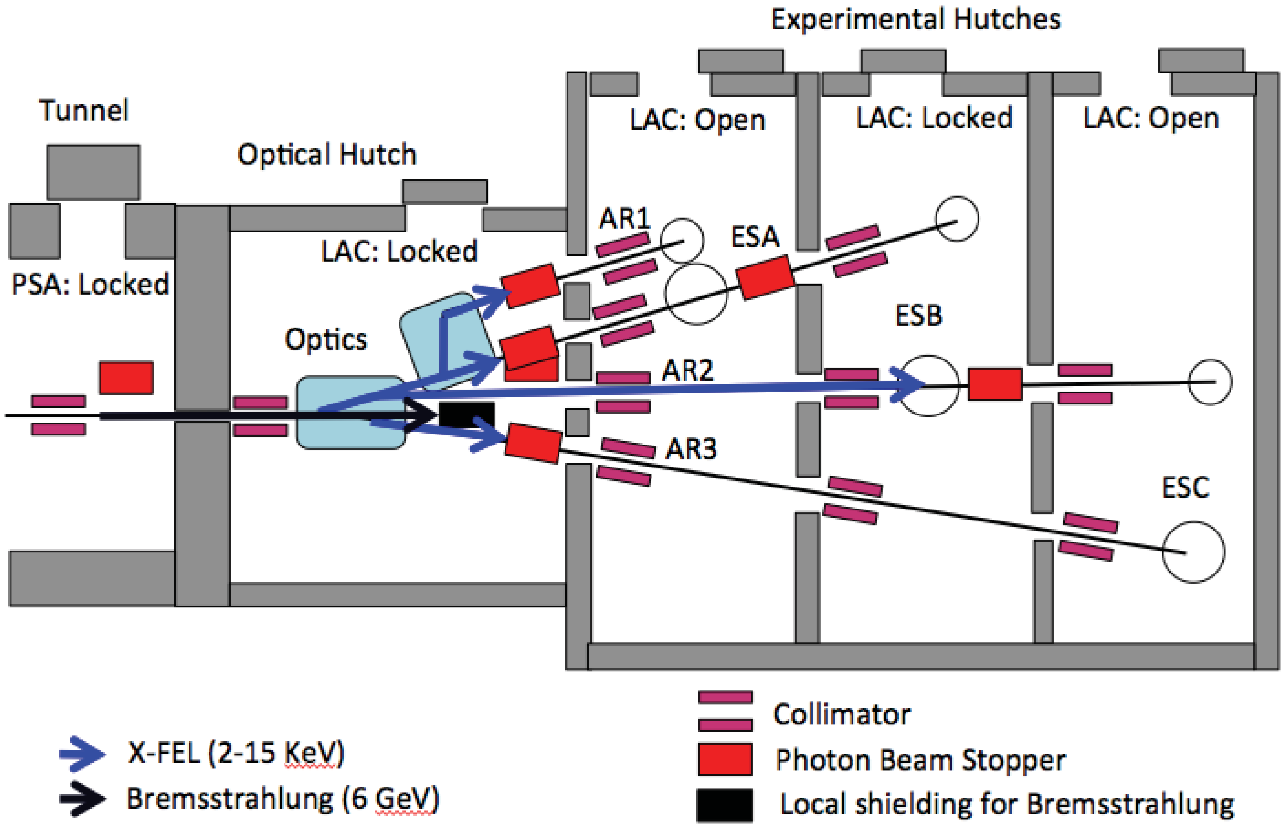

Figure 3: Mode of operation “Beam on Experimental Hutch 2“

Table 1: Summary of the BST and LAC state fort he various operation modes on ARAMIS.

Beam Stopper (BST) vs Local Access Control (LAC)											
	Service	**Normal operation with electron beam**									
				AR1			**AR2**			**AR3**	
	Service without electron beam	Access to optical hutch	Beam on Optical Hutch	Beam on Exp. Hucht1 for ES11 (>2017)	Beam on Exp. Hucht1 for ES12	Beam on Exp. Hutch2 with AR1 (>2017)	Beam on Exp. Hucht2 for ES21 (>2017)	Beam on Exp. Hucht2 for ES22	Beam on Exp. Hutch3 with AR2 (>2017)	Beam on Exp. Hucht2 for ES31 (>2017)	Beam on Exp. Hucht2 for ES32
PSA/LAC											
Tunnel	Open	Locked	Locked	Locked	Locked	Locked	Locked	Locked	Locked	Locked	Locked
Opt. Hutch	Open	Open	Locked	Locked	Locked	Locked	Locked	Locked	Locked	Locked	Locked
Exp. Hutch1	Open	Open	Open	Locked	Locked	Open	Open	Open	Open	Open	Open
Exp. Hutch2	Open	Open	Open	Open	Open	Locked	Locked	Locked	Open	Open	Open
Exp. Hutch3	Open	Open	Open	Open	Open	Open	Open	Open	Locked	Locked	Locked

Beam Stopper											
FE-BST	Open	Closed	Open	Open	Open	Open	Open	Open	Open	Open	Open
AR11-BST	Open	Open	Closed	Open	Closed	Closed	Closed	Closed	Closed	Closed	Closed
AR12-BST	Open	Open	Closed	Closed	Open	Open	Closed	Closed	Closed	Closed	Closed
AR13-BST	Open	Closed	Closed	Closed	Closed	Open	Closed	Closed	Closed	Closed	Closed
AR20-BST	Open	Open	Closed	Closed	Closed	Closed	Open	Open	Open	Closed	Closed
AR21-BST	Open	Open	Closed	Closed	Closed	Closed	Closed	Closed	Open	Closed	Closed
AR30-BST	Open	Open	Closed	Closed	Closed	Closed	Closed	Closed	Closed	Open	Open

1st phase (< 2017)	
2nd phase (>2017)	

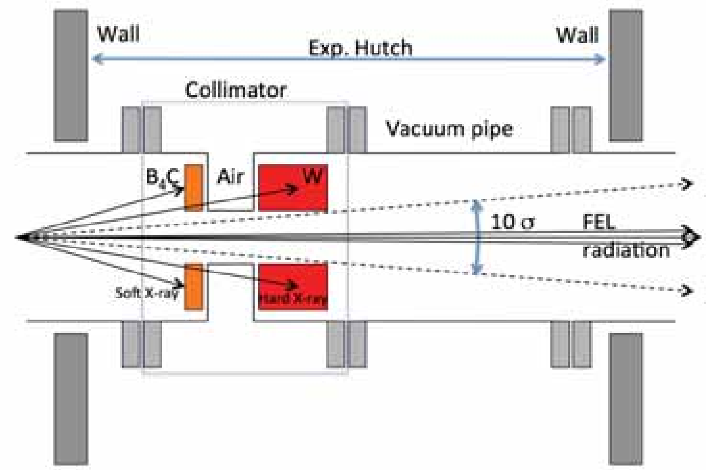

Figure 4: Schematic scheme of the B_4C-Air-Tungsten structure of the collimator including the vacuum pipe of the beamline inside the experimental hutches.

Table 2: Parameters for the "stay clean" for each type of collimators.

Collimator	Location	ΔZ position from ID	Stay Clean	Stay clean for Spontant Radition	Stay clean for FEL	See Breamstralung
FE-COLL	Tunnel	35.4 m	$30\ \sigma_{FEL}$	Yes	Yes	Yes
AR10-COLL	Optical Hutch	62 m	$30\ \sigma_{FEL}$	Yes	Yes	Yes
AR11-COLL	Experimental Hutch1	113.7 m	$10\ \sigma_{FEL}$	No	Yes	No
AR12-COLL1	Experimental Hutch1	113.7 m	$10\ \sigma_{FEL}$	No	Yes	No
AR12-COLL2	Experimental Hutch2	133 m	$10\ \sigma_{FEL}$	No	Yes	No
AR20-COLL1	Experimental Hutch1	115 m	$10\ \sigma_{FEL}$	No	Yes	No
AR20-COLL2	Experimental Hutch2	127 m	$10\ \sigma_{FEL}$	No	Yes	No
AR22-COLL	Experimental Hutch3	151 m	$10\ \sigma_{FEL}$	No	Yes	No
AR30-COLL1	Experimental Hutch1	119 m	$10\ \sigma_{FEL}$	No	Yes	No
AR30-COLL2	Experimental Hutch2	132.1 m	$10\ \sigma_{FEL}$	No	Yes	No
AR30-COLL3	Experimental Hutch3	146.9 m	$10\ \sigma_{FEL}$	No	Yes	No

4. Photon Beam Stopper (BST)

The Photon Beam Stopper (BST) is used to block the Bremsstrahlung, the synchrotron spontaneous and the FEL radiations. The BST has two activators as shown in the figure 5. The first activator protects the equipment from soft x-ray FEL radiation. This activator is implemented into the Equipment Protection System (EPS) of the beamline. This activator is done in B_4C and can quickly (few 10 msec) be moved into the beam. The second activator is used to block the soft and hard x-ray radiations as well the Bremsstrahlung. This activator has the same B_4C-Air-Tungsen structure as the collimator. The BST is linked with the LAC. The Photon Beam Stopper should stop the photon beam over a solid angle typical 3-5 time larger than the acceptance angle of the collimator located up-stream.

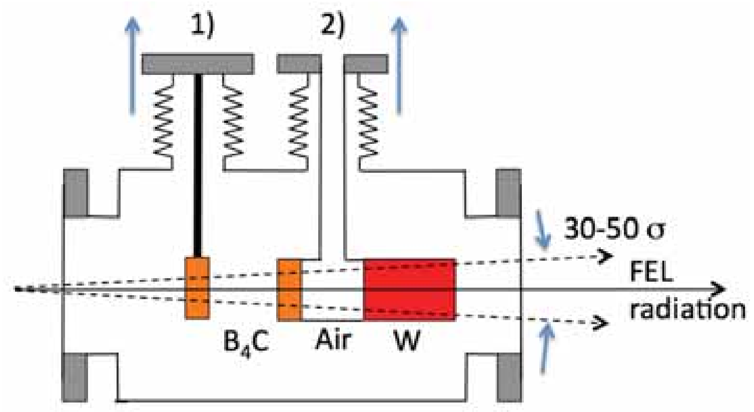

Figure 5: Schematic view of the beamstopper (from the experimental hutch) including the 2 activators.

5. Radiation

The type and amount of radiation differ depending on the location. In the tunnel, the Bremsstrahlung from residual gas, the spontaneous radiation and the FEL radiation are all co-propagating along the beamline direction. It should be noted that the angular distributions of those radiation differ [1]. In the tunnel, the CO and the BST ensure in closed position a dose rate below the guideline limits and allow a free access to the optical hutch. In the optical hutch, the two off-mirrors at each beamlines offset the spontaneous and FEL radiations from the original beamline axis. Calculations [4] have show that the Bremsstrahlung scattered by the first off-mirror can be neglected. As a consequence, the Bremsstrahlung can be separated from the FEL radiation after the first off-mirror. The Photon Beam Stopper and Collimator between the optical hutch and experimental hutch do not see the Bremsstrahlung and can be designed for spontaneous and FEL radiation only. The same apply for the BST and CO between the different experimental hutches.